Gravitational Waves as Cosmological Probes for New Physics between the Electroweak and the Grand-Unification Scale

Gravitationswellen als kosmologische Phänomene neuer Physik im Bereich zwischen der elektroschwachen und der Skala der Großen Vereinheitlichung

DIPLOMARBEIT
zur Erlangung des Akademischen Grades
DIPLOM-PHYSIKERIN

Laura Sagunski

November 2012

Universität Hamburg
Department Physik

und

DESY
Theory Group

Gutachter der Diplomarbeit

Erstgutachter:	Dr. Thomas Konstandin DESY Theory Group
Zweitgutachter:	Prof. Dr. Günter Sigl II. Institut für Theoretische Physik Universität Hamburg

To my parents

and

to my boyfriend Timo

for their incredible support and their infinite love

Abstract

Relic gravitational waves, generated by strongly first-order phase transitions in the early Universe, can serve as cosmological probes for new physics beyond the Standard Model. We investigate phase transitions at temperatures between the electroweak and the GUT scale in two extensions of the Standard Model for their possibility to provide detectable gravitational radiation. First, we study the $\mathbb{Z}_2$ symmetry breaking phase transition in the Standard model extended by a real gauge singlet. The analysis yields that the gravitational wave amplitude of the first-order phase transition with a thermally induced barrier is several orders too small for being detectable. The second model we discuss is a left-right symmetric model based on the gauge group $SU(2)_L \otimes SU(2)_R \otimes U(1)_{B-L}$ generating a first-order phase transition already due to the emergence of a barrier in the tree-level potential. We derive an upper bound on the peak amplitude of the gravitational wave spectrum of the order $h_o^2\tilde{\Omega}_{GW} \simeq 3\cdot 10^{-11}$. Hence, for very strong phase transitions a detection with the spaceborne interferometer LISA will be possible, whereas the sensitivity of the (cross-correlated) BBO detector will even allow to observe the gravitational wave spectrum within the whole parameter range of the model. By using the correlation between the characteristic parameters α and β of the gravitational wave spectrum, we finally compute the lower bounds on $\alpha(T_*)$ in dependence of the tunneling temperature T_* which are necessary for a detection of the model spectrum by the specific detectors.

Zusammenfassung

Relikt-Gravitationswellen, die während Phasenübergängen erster Ordnung im frühen Universum erzeugt wurden, sind kosmologische Phänomene, die dazu dienen können Konzepte neuer Physik jenseits des Standardmodells zu überprüfen. Wir untersuchen die Phasenübergänge zweier Erweiterungen des Standardmodells bei Temperaturen im Bereich zwischen der elektroschwachen Skala und der Skala der Großen Vereinheitlichung im Hinblick auf ihre Möglichkeit detektierbare Gravitationswellen zu generieren. Zuerst analysieren wir einen $\mathbb{Z}_2$-Symmetrie brechenden Phasenübergang in einem Modell, das das Standardmodell um ein reelles Eichsinglett erweitert. Unsere Rechnungt zeigt, dass die Amplituden der Gravitationswellen, die durch einen thermisch induzierten Phasenübergang erster Ordnung generiert wurden, für eine Detektion mehrere Größenordnungen zu klein sind. Als zweites untersuchen wir ein links-rechts-symmetrisches Modell basierend auf der Eichgruppe $SU(2)_L \otimes SU(2)_R \otimes U(1)_{B-L}$, das einen Phasenübergang erster Ordnung bereits durch eine Barriere in der niedrigsten Ordnung des effektiven Potentials erzeugt. Wir erhalten für die Amplituden der Gravitationswellen eine obere Grenze von $h_o^2\tilde{\Omega}_{GW} \simeq 3\cdot 10^{-11}$. Demnach wird es im Fall starker Phasenübergänge möglich sein, das Gravitationswellenspektrum mit dem weltraumgestützten Interferometer LISA zu beobachten, worüberhinaus die Sensitivität des (korrelierten) BBO-Detektors eine Detektion der Spektra des gesamten Parameterbereichs erlauben wird. Unter Ausnutzung der Korrelation der charakteristischen Parameter α und β bestimmen wir abschließend die für eine Messung der Spektra durch die spezischen Detektoren erforderlichen unteren Grenzen $\alpha(T_*)$ in Abhängigkeit der Tunneltemperatur T_*.

Contents

I. Theoretical Framework 7

List of Figures

List of Tables

Introduction

Preface

A direct detection of gravitational waves (GWs) will probably become reality in the near future. Currently, the first generation of ground-based interferometric GW detectors, such as LIGO [8, 7] and VIRGO [52, 9], is already operational, while the second generation of spaceborne interferometers like LISA [67, 68, 69, 22, 153] and BBO [107, 139] is planned to be launched within the next years. On the one hand, these experiments aim to search for GW signals from individual astrophysical events as for instance coalescing binary systems [21, 2, 5] (e.g., white dwarf binaries), continuous gravitational sources [4] as rotating neutron stars or orbiting black hole systems as well as GW wave bursts [20, 3]. On the other hand, the searches focus on (stochastic) GW backgrounds of astrophysical sources [90, 44] such as core collapse of supernovae, but also of cosmological origin.

Stochastic GW backgrounds of cosmological origin are constituted by (redshifted) relic gravitational waves from the early stages in the evolution of the Universe, carrying unaltered information about the state of the universe at the time of their production. Thus, these gravitational waves can serve, in case of their detection, as cosmological probes for fundamental concepts of particle physics at unexplored high energies which will never be reachable by accelerator or collider experiments.

Possible cosmological sources for the production of stochastic gravitational waves compose inflation [17, 197, 14], preheating after inflation [151, 79, 78, 95], first-order phase transitions [138, 125, 49, 103, 112], a pre-big-bang phase of expansion [42, 96], cosmic topological defects [201, 202, 45, 46, 30] (e.g. vibration of cosmic strings) or dynamics of extra dimensions [189, 59, 60]. Among these hypothetical sources, the GW production during inflation (by quantum generation of gravitons) is theoretically strongly motivated. A detection of the relic gravitational waves from inflation, which will be achievable by the space interferometer BBO, would be a smoking-gun signal from inflation and would in particular allow to test the paradigm of inflation as an era of exponential expansion in the early Universe.[1]

---

[1] The WMAP constraint on the energy scale of the inflaton requires at least a GW amplitude of $h_o^2\Omega_{GW} \lesssim 10^{-14} \ldots 10^{-15}$ of the inflationary GW spectrum [191]. The detection of this relic GW background from

We will however focus on the stochastic background of gravitational waves produced by cosmological *first-order phase transitions*. In a first-order phase transition the Universe finds itself in a metastable state (the symmetric "true vacuum" state) which is separated from the false vacuum state (the broken phase) by a barrier in the potential of the order parameter, usually a scalar field ϕ [23, 167]. The phase transition from the true to the false vacuum state proceeds by nucleation of true-vacuum bubbles via quantum tunneling. If the rate of bubble nucleation exceeds the expansion rate of the Universe, the bubbles percolate leaving the Universe in the broken-symmetry phase.
During first-order phase transitions stochastic gravitational waves can be produced by colliding phase boundaries (bubble collisions) [207, 137, 136, 167, 50, 112], turbulent motion of the plasma [135, 77, 48, 99] or magnetic fields [110, 199, 11, 39, 48]. We will focus on the production of gravitational waves by bubble collisions. In this case, the vacuum energy (latent heat) gained in the phase transition is transferred to kinetic energy of the bubble wall and bulk motion of the plasma. A large amount of the vacuum energy is stored close to the bubble walls. When bubble collisions break the spherical symmetry of the individual bubbles, this energy is partially released into gravitational waves.
Quantitatively, a first-order phase transition is characterized by the phase transition strength. The phase transition strength is defined as ratio of the vacuum expectation value (VEV) of the regarded scalar field ϕ at the critical temperature T_C of the phase transition to the latter. For a strongly first-order phase transition the phase transition strength has to lie above the lower bound [61]

$$\frac{\langle\phi(T_C)\rangle}{T_C} \gtrsim 1. \tag{0.1}$$

Note that this is the same condition as required for viable baryogenesis avoiding sphaleron washout [87, 88].[2]

Within the thermal evolution of the Universe a number of phase transitions are expected to have been occurred. In particular, the QCD phase transition proceeded at a temperature $T_{QCD} = 150\,\mathrm{MeV}$ [118, 188, 187]. Above this temperature the deconfinement of quarks and gluons generates a quark-gluon plasma. At temperatures of $T_{EW} = 10^2$ GeV the spontaneous breakdown of the $SU(2)_L \otimes U(1)_Y$ symmetry to $U(1)_{em}$ induces the electroweak phase transition (EWPT) [75, 74, 43]. Further phase transitions could have occurred even earlier at temperatures up to the grand-unification (GUT) scale of the order $T_{GUT} = 10^{16}$ GeV [19]. Based on the fact that the running couplings of the Standard Model unify to a single gauge coupling at the temperatures $T_{GUT} = 10^{16}$ GeV, the key idea of GUTs is to describe the fundamental interactions by a unique gauge group G including the Standard Model gauge

---

inflation will be one of the main goals of the space interferometer BBO ("Big Bang Observer").

[2] Two possible combustion modes of the energy liberated by bubble collisions exist, deflagration and detonation. The latter allows large production of gravitational waves if the bubble wall velocity is bigger than the speed of sound. This is the same condition for "local baryogenesis" (B and CP violating processes close to the bubble wall) to dominate "non-local baryogenesis" (only CP violating processes). As the subsequently expanding bubbles can drive the primordial plasma out of thermal equilibrium, these requirements allow to fulfill the Sakharov conditions for successful baryogenesis. To avoid sphaleron washout, the sphaleron process need to be sufficiently suppressed in the broken phase leading to the condition in (0.1).

symmetry as a subgoup (for a review see for instance [142]). Via a pattern of the spontaneous symmetry breaking during the thermal evolution of the Universe, this symmetry is subsequently broken down to the Standard Model gauge symmetry. Hence, in extensions of the Standard Model phase transitions might have been occurred at considerably higher temperatures [89].

Due to the failure in providing an explanation on open issues as dark matter and dark energy, the origin of neutrino masses, the baryon asymmetry of the Universe or the hierarchy problem, an extension of the Standard Model is necessarily required. The Standard Model itself can be rather considered as an effective theory with a low physical cutoff, which can be probed with current particle physics experiments as for instance the LHC.

In the Standard Model the EWPT is neither strong enough for viable baryogenesis, nor for production of detectable gravitational waves . Indeed, the requirement of a strongly first-order phase transition in the Standard Model imposes an upper bound on the Higgs mass which is below the current experimental bound and therefore excluded [35]. Non-perturbative lattice simulations revealed that the phase transition is not of first order, but rather a smooth crossover (between first and second order) [123, 181, 66].

Partially motivated by the importance for baryogenesis, the EWPT has been studied in extensions of the Standard Model such as the Minimal Supersymmetric Standard Model (MSSM) [98, 166, 86, 41], the Next-to-Minimal Supersymmetric Standard Model (NMSSM) [172, 70, 111, 158], where an additional gauge singlet in the Higgs sector is introduced, and its restricted version, the nMSSM [168, 71, 158, 114] solving the μ-problem of the NMSSM[3], or the Standard Model with dimension-six Higgs potential [105, 104, 36]. In the MSSM a strong enough phase transition requires light Higgs and stop masses leaving only marginally possibilities for viable baryogenesis [179], whereas the N(n)MSSM provides a phase transition which is strong enough for baryogenesis. Simultaneously, the lightest neutralino could simultaneously provide the dark matter of the Universe.

Detectible relic gravitational waves from first-order phase transitions can give a hint for the physics beyond the Standard Model. In particular, it has been investigated if the EWPT in the MSSM, N(n)MSSM and the Standard Model with dimension-six Higgs potential provide the possibility of observable gravitational waves. In the MSSM a detection of the GW spectrum is excluded [23]. Whereas in the N(n)MSSM and the Standard Model with dimension-six Higgs potential the gravitational radiation will be not detectable by LISA (possessing a minimal sensitivity of $h_o^2\Omega_{GW} \sim 10^{-11}$), but only by the cross-correlated BBO ($h_o^2\Omega_{GW} \sim 10^{-17}$) in case of extremely strong phase transitions [113]. However, for a wide range of the model parameter space a detection is excluded even for BBO. This is partially caused by the correlation between the strength of the phase transition and the peak frequency of the GW spectrum: Strongly first-order phase transitions are required for generating a peak amplitude of the GW spectrum which overlaps with the minimal sensitivity the GW detectors and hence will be detectable. Since stronger phase transitions proceed at lower

---

[3] The MSSM suffers from the so-called μ-problem due to domain walls. For consistency of the theory the mass mixing term μ between the two Higgs doublet in the superpotential has to be of the order of the electroweak scale being much smaller than the GUT scale and additionally stable under perturbative corrections. An elegant way to solve this problem consists in introducing an additional gauge singlet in the Higgs sector so that the the mass term is generated dynamically as the singlet develops its VEV.

temperatures and create larger bubbles, the peak frequency of the GW spectrum is simultaneously shifted to lower frequencies which might lie beyond the experimentally accessible frequency range [113, 112]. (The spaceborne detectors as LISA and BBO are sensitive in the frequency range $f \simeq 10^{-4} \ldots 1\,\mathrm{Hz}$, while a frequency range of $f \simeq$ few Hz ...few kHz is accessible by ground based detectors like LIGO and VIRGO [156].)

Concept of the Thesis

Our motivation in this thesis is therefore to investigate first-order phase transitions in extensions of the Standard Model which are assumed to proceed at temperatures between the electroweak and the GUT scale,

$$T_{EW} < T < T_{GUT}. \tag{0.2}$$

Due to this high temperature scale the peak frequency of the GW spectrum, arising from bubble collisions during the first-order phase transition, will lie in the high-frequency part of the experimentally accessible frequency range. If we additionally require the phase transition to be strongly first-order so that a high peak amplitude is generated, the GW spectrum might light in the experimentally sensitive range an hence would be detectable. In turn, the gravitational waves could serve as cosmological probes of the underlying physical conception of the model.

Within the framework of this thesis, we will explicitly investigate two extensions of the Standard Model, which provide different mechanisms for generating a strongly first-order phase transition, with regard to their possibility of providing detectable gravitational waves. The most studied mechanism to achieve a first-order phase is based on inducing the necessary barrier between the true and the false vacuum thermally by using the bosonic finite-temperature one-loop corrections to generate a cubic term in the effective potential. We will apply this mechanism to the Standard model extended by an additional real gauge singlet. The importance of this model is due to the fact that a large variety of extensions of the Standard Model contain elements which transform non-trivially under a hidden sector gauge group, but as singlets under the Standard Model gauge group [83, 84]. The Standard Model Higgs field plays a special role with respect to the hidden sector since the only renormalizable interaction of such scalars with the Standard Model occurs via the Higgs sector. This can in consequence serve as window into the hidden sector and might provide important theoretical and phenomenological implications [186, 170, 38].
The second model we will discuss is the left-right symmetric model which is based on the gauge symmetry group $SU(2)_L \otimes SU(2)_R \otimes U(1)_{B-L}$ [169, 163, 190]. Besides its original conception for explaining parity violation by incorporating it as spontaneous broken symmetry [162], the left-right symmetric model associates a physical meaning to the $U(1)$ generator arising as the $B-L$ quantum number and provides additional sources for CP violation . The extension of the gauge group is associated with an enlargement of the Standard Model particle content by right-handed (Majorana) neutrinos as well as right-handed massive gauge bosons. Since these right-handed particle escape experimental detection, the right-handed

particles have to acquire their masses during L-R symmetry breaking at large scale. As the left-right symmetric model incorporates a barrier of the effective potential already at tree-level (and not due to thermal corrections), the associated phase transition will be strongly first-order and hence suitable for a possible generation of detectable gravitational waves.

This thesis is structured as follows. In Part I we will develop the theoretical framework necessary to investigate gravitational waves from first-order phase transition at high temperature scales. Therefore, we will first review the conceptions of thermal field theory (cf. Chap. 1). As the study of spontaneous symmetry breaking at finite temperature can be reduced to the investigation of the effective potential of a field inside a thermal bath, we will compute the effective potential, including zero-temperature and finite temperature corrections to the tree-level potential, up to the one-loop order. Afterwards, we will determine in Chap. 2 the GW spectrum from bubble collisions during first-order phase transitions and in particular discuss the key parameters characterizing the GW spectrum.

In Part II, we will apply the derived formulae to the cases of the singlet extension of the Standard Model (cf. Chap. 3) and the left-right symmetric model (cf. Chap. 4). For both models, we will compute the effective potential in order to investigate the phase transition. In detail, we will determine the critical temperature and the corresponding VEV of the effective potential and discuss the parameter constraints necessary to generate a physically viable phase-transition scenario in the specific model. Afterwards, we will compute the parameters characterizing the GW spectrum arising from the considered phase transition. Finally, we will perform a numerical analysis of the gravitational wave spectrum to discuss whether the physical conception of the model can be probed by the detection of gravitational waves. We will summarize and discuss our results in the Conclusions.

In the Appendix we compute the bosonic thermal masses for the singlet extension of the Standard Model (cf. Chap. A). These are needed to generate the thermal barrier for the first-order phase transition. Besides, the field-dependent gauge boson masses for the left-right symmetric model are derived in Chap. B.

To be able to compare the GW spectra derived from the models to the experimental sensitivities, we review in Chap. C the different types of interferometric GW detectors and compute their sensitivity curves from the experimental data.

Notations and Conventions

As usual in particle physics, we will work in natural units where the reduced Planck constant $\hbar$, the speed of light c as well as the Boltzmann constant k equal

$$\hbar = c = k = 1. \tag{0.3}$$

We will display Lorentz indices by small Greek letters as for instance $\mu, \nu = 0, 1, 2, 3$, whereas Latin indices, e.g. $i, j = 1, 2, 3, \ldots$, will refer to conventional summations. In addition, we will use the Einstein summation convention by implicitly summing over repeated indices.

Part I.

Theoretical Framework

Chapter 1

Thermal Field Theory

In order to investigate first-order phase transitions proceeding at high temperatures in the early stages of the Universe, we have to use the framework of *thermal* quantum field theory. In comparison to the classical field theory, quantum field theory at zero temperature involves virtual particles (in form of internal loops) which affect the field energy density by emission and reabsorbing processes. To include these quantum corrections, the classical field theory is generalized to an effective theory. The corresponding potential density is called the effective potential. Moreover, in thermal field theory, thermal fluctuations of the quantum fields have to be taken into account. Therefore, a generalization of the effective potential at finite temperature is required.

As the study of spontaneous symmetry breaking can be reduced to the determination of the nature of the ground state of the effective potential, i.e. the vacuum state of the theory, the effective potential will provide our basic tool for the investigation of phase transitions at finite temperature. In this chapter, we will discuss the main aspects of thermal field theory related to the effective potential. If not marked otherwise, we will thereby refer to the reviews [31, 126, 40, 175, 177, 178, 180].

1.1. Effective Potential at Zero Temperature

The fundamental quantity of quantum field theories is the Lagrangian density $\mathcal{L} = \mathcal{L}\left[\phi_i, \partial_\mu \phi_i\right]$, which is usually referred to simply as Lagrangian. It is a functional of the space-time dependent quantum fields $\phi_i(x^\mu) \equiv \phi_i(x)$ and their derivatives $\partial_\mu \phi_i$.[1] In general, $\phi_i(x)$ might represent scalar, vector and fermion fields.

The integral of the Lagrangian density over the four dimensional space-time defines the action S as a functional of the quantum fields ϕ_i,

$$S\left[\phi_i\right] = \int d^4x\, \mathcal{L}\left[\phi_i, \partial_\mu \phi_i\right]. \tag{1.1}$$

---

[1] We will denote functions by parentheses, e.g. $\phi_i(x)$, and functionals, such as $\mathcal{L} = \mathcal{L}\left[\phi_i, \partial_\mu \phi_i\right]$, by square brackets.

1.1.1. Generating Functionals

Consider now a theory described by one real *scalar* field $\phi(x)$ with Lagrangian $\mathcal{L}\big[\phi_i, \partial_\mu \phi_i\big]$. The Lagrangian is required to be intrinsically invariant with respect to the underlying gauge symmetry. In the presence of an external field $J(x)$ however, the coupling of the field $\phi(x)$ to the external source causes a symmetry breaking term in the Lagrangian [121],

$$\mathcal{L}\big[\phi_i, \partial_\mu \phi_i\big] \to \mathcal{L}\big[\phi_i, \partial_\mu \phi_i\big] + \phi(x)\, J(x)\,. \tag{1.2}$$

The determination of the vacuum expectation value (VEV) of the field $\phi(x)$ in the presence of the external source $J(x)$ can be reduced to a pure variational problem by using the analogy between the vacuum-transition amplitude of the S-matrix in quantum field theories and the partition function Z in statistical mechanics [37]. In the Feynman path-integral representation [91] this analogy reads

$$\langle 0^+ | 0^- \rangle_J = Z[J] \equiv \int \mathcal{D}\phi \, \exp\left(i \int d^4x \left\{ \mathcal{L}\big[\phi_i, \partial_\mu \phi_i\big] + \phi(x)\, J(x) \right\} \right), \tag{1.3}$$

where $Z[J]$ constitutes the generating functional of the source field. The definition of the free energy functional $W[J]$ by

$$Z\,[J] \equiv \exp(i\, W[J]) \tag{1.4}$$

(in analogy to the free energy in statistical physics) allows for deriving the VEV of the field $\phi(x)$ in the presence of the external source J, defined as the classical field $\phi_{cl}(x)$, by functional variation

$$\begin{aligned} \phi_{cl}(x) &\equiv \frac{\langle 0^+ | \phi(x)\, | 0^- \rangle_J}{\langle 0^+ | 0^- \rangle_J} = -\frac{\delta W[J]}{\delta J(x)} \\ &= \frac{\int \mathcal{D}\phi\, \phi(x)\, \exp\left(i \int d^4x \left\{ \mathcal{L}\big[\phi_i, \partial_\mu \phi_i\big] + \phi(x)\, J(x) \right\} \right)}{\int \mathcal{D}\phi\, \exp\left(i \int d^4x \left\{ \mathcal{L}\big[\phi_i, \partial_\mu \phi_i\big] + \phi(x)\, J(x) \right\} \right)}\,. \end{aligned} \tag{1.5}$$

It is convenient to perform a Legendre transformation of $W[J]$ to introduce the effective action $\Gamma[\phi_{cl}]$ (constituting the quantum analogy to the Gibbs free energy in statistical physics) as a functional of the classical field ϕ_{cl},

$$\begin{aligned} \Gamma[\phi_{cl}] &\equiv W[J] - \int d^4x\, \frac{\delta W[J]}{\delta J(x)} J(x) \\ &= W[J] - \int d^4x\, \phi_{cl}(x)\, J(x)\,. \end{aligned} \tag{1.6}$$

Expanding the energy functional $W[J]$ and the effective action $\Gamma[\phi_{cl}]$ in a Taylor series in terms of J and ϕ_{cl}, respectively,[2]

$$iW[J] = \sum_{n=0}^{\infty} \frac{i^n}{n!} \int d^4x_1 \ldots d^4x_n\; J(x_1) \ldots J(x_n)\; G_c{}^{(n)}(x_1, \ldots, x_n)\,, \tag{1.7}$$

$$\Gamma[\phi_{cl}] = \sum_{n=0}^{\infty} \frac{i^n}{n!} \int d^4x_1 \ldots d^4x_n\; \phi_{cl}(x_1) \ldots \phi_{cl}(x_n)\; \Gamma^{(n)}(x_1, \ldots, x_n)\,, \tag{1.8}$$

---

[2] Alternatively, the effective action $\Gamma[\phi_{cl}]$ can be expanded in powers of momentum about the point with vanishing external momenta, i.e. about an constant value ϕ_{cl} of the classical field $\phi_{cl}(x)$ [205, 64].

points out their physical importance. The energy functional $W[J]$ constitutes the generating functional for the connected Green's functions ${G_c}^{(n)}(x_1, \ldots, x_n)$, while the effective action arises as generating functional for the one-particle irreducible (1PI) Green's functions $\Gamma^{(n)}(x_1, \ldots, x_n)$, defined as the sum of all connected Feynman diagrams, which cannot be disconnected by removing a single internal line, and evaluated without propagators on the external lines [205].
If we now perform a Fourier transformation of $\Gamma^{(n)}(x_1, \ldots, x_n)$ to momentum space and require the classical field to be space-time independent, $\phi_{cl}(x) \equiv \phi_{cl}$, (1.8) becomes [175]

$$\Gamma[\phi_{cl}] = \sum_{n=0}^{\infty} \frac{1}{n!}\, \phi_{cl}^n\, (2\pi)^4\, \delta^{(4)}(0)\, \Gamma^{(n)}(p_i = 0) = \int d^4x \sum_{n=0}^{\infty} \frac{1}{n!}\, \phi_{cl}^n\, \Gamma^{(n)}(p_i = 0)\,. \tag{1.9}$$

Thereby, we have used the integral definition of the Dirac δ-function in the last step. The comparison of the above equation with the effective potential $V_{eff}(\phi_{cl})$, which is defined in analogy to (1.1) by

$$\Gamma[\phi_{cl}] \equiv -\int d^4x\, V_{eff}(\phi_{cl}) \tag{1.10}$$

as a function of the classical field ϕ_{cl}, finally allows for deriving a general expression of the effective potential,

$$V_{eff}(\phi_{cl}) = -\sum_{n=0}^{\infty} \frac{1}{n!}\, \phi_{cl}^n\, \Gamma^{(n)}(p_i = 0)\,. \tag{1.11}$$

Since the classical field ϕ_{cl} in the absence of an external source equals the VEV of quantum field ϕ (cf. (1.5)) and $\frac{\delta\Gamma[\phi_{cl}]}{\delta\phi_{cl}} = -J$ (cf. (1.6)), the condition for spontaneous symmetry breaking reads

$$\frac{\delta\Gamma[\phi_{cl}]}{\delta\phi_{cl}} = 0 \qquad \text{for } \phi_{cl} \neq 0 \tag{1.12}$$

or equivalently by using (1.10)

$$\frac{\partial V_{eff}(\phi_{cl})}{\partial\phi_{cl}} = 0 \qquad \text{for } \phi_{cl} \neq 0. \tag{1.13}$$

Hence, the study of spontaneous symmetry breaking can be reduced to the computation of the effective potential whose minimum will determine the nature of the ground state [205].

1.1.2. Functional Evaluation of the Effective Potential at Zero Temperature

According to (1.11), the calculation of the effective potential requires the summation of infinite series of Feynman diagrams at vanishing external momentum. However, it is possible by usage of the path-integral formalism to deduce a formula representing the effective potential as a series expansion to a given loop-order, wherein each order contains a *finite* number of Feynman diagrams [119]. Define therefore a Lagrangian $\hat{\mathcal{L}}(\phi_{cl};\phi(x))$ by shifting the scalar field $\phi(x)$ by the constant classical field ϕ_{cl}

$$\int d^4x\, \hat{\mathcal{L}}(\phi_{cl};\phi(x)) \equiv S\left[\phi_{cl}+\phi(x)\right] - S\left[\phi_{cl}\right] - \int d^4x\, \phi(x)\, \frac{\delta S\left[\phi_{cl}\right]}{\delta\phi_{cl}}, \tag{1.14}$$

where the subtraction of the shifted action $S\left[\phi_{cl}\right]$ ensures the vacuum energy to be zero and the last term is required for canceling the tadpole part of the shifted action.
Next we decompose the Lagrangian $\hat{\mathcal{L}}(\phi_{cl};\phi(x))$ into a free term, containing the quadratic field contributions and providing the propagator $\mathcal{D}(\phi_{cl};x-y)$ of the shifted theory, and an interaction term for the higher-order field contributions,

$$\hat{\mathcal{L}}(\phi_{cl};\phi(x)) = \hat{\mathcal{L}}_0(\phi_{cl};\phi(x)) + \hat{\mathcal{L}}_{int}(\phi_{cl};\phi(x))\,. \tag{1.15}$$

By using the fact that the propagator in the shifted theory $\mathcal{D}(\phi_{cl};x-y)$ also satisfies the relation

$$i\,\mathcal{D}^{-1}(\phi_{cl};x-y) = \left.\frac{\delta S\left[\phi\right]}{\delta\phi(x)\,\delta\phi(y)}\right|_{\phi=\phi_{cl}} \tag{1.16}$$

and performing a Fourier transform of the inverse propagator to $i\,\mathcal{D}^{-1}(\phi_{cl};p)$, the effective potential finally reads

$$\begin{aligned} V_{eff}(\phi_{cl}) &= V_0(\phi_{cl}) - \frac{i}{2}\int\frac{d^4p}{(2\pi)^4}\,\ln\left[\det\left\{i\,\mathcal{D}^{-1}(\phi_{cl};p)\right\}\right] \\ &\qquad + i\left\langle \exp\left[i\int d^4x\,\hat{\mathcal{L}}_{int}(\phi_{cl};\phi(x))\right]\right\rangle \\ &= V_0(\phi_{cl}) + V_1^{T=0}(\phi_{cl}) + V_{n\geq 2}^{T=0}(\phi_{cl})\,. \end{aligned} \tag{1.17}$$

Therein, the zero-loop contribution $V_0(\phi_{cl})$ just equals the classical (tree-level) potential, whereas the second term is the zero-temperature one-loop correction to the effect potential and the last term summarizes all higher-order loop corrections.

1.1.3. One-Loop Effective Potential at Zero Temperature

Scalar Fields. Since we calculated (1.17) from the premise of a theory described by one real scalar field $\phi(x)$ (cf. Sec. 1.1.1), the shifted propagator in the one-loop contribution of the above equation is given by $i\,\mathcal{D}^{-1}(\phi_{cl};p) = p^2 - m^2(\phi_{cl})$, containing the *shifted* mass

$$m^2(\phi_{cl}) \equiv \left.\frac{\partial^2 V_0(\phi+\phi_{cl})}{\partial\phi^2}\right|_{\phi=0}. \tag{1.18}$$

After inserting the propagator in (1.17) and performing a Wick rotation $p^0 = ip_E^0$ with $p_E \equiv \left(-ip^0, \vec{p}\right)$ to Euclidean four-dimensional space-time[3], we obtain the final expression

---

[3] In the following, we will omit the explicit notation of the subindex E, denoting the Euclidean momenta.

of the one-loop contribution to the effective potential for one real scalar field as[4]

$$V_{1_S}^{T=0}(\phi_{cl}) = \frac{1}{2}\int \frac{d^4p}{(2\pi)^4}\,\ln\left[p^2 + m^2(\phi_{cl})\right]. \tag{1.19}$$

The generalization of this equation to the case of multiple *complex* scalar fields ϕ_i with Lagrangian $\mathcal{L} = \partial^\mu\phi^k\,\partial_\mu\phi_k^\dagger - V_0(\phi_i)$, $i, k \in \{1, \ldots, N_S\}$, implies the existence of N_S classical fields $\phi_{i_{cl}}$ and hence the replacing of the shifted mass by a mass matrix $\mathcal{M}_S^2(\phi_{i_{cl}})$ whose elements are defined by [205]

$$\left(\mathcal{M}_S^2(\phi_{i_{cl}})\right)_{kl} = m_{kl}{}^2(\phi_{i_{cl}}) \equiv \left.\frac{\partial^2 V_0\left(\phi_i + \phi_{i_{cl}}\right)}{\partial\phi_{k_{cl}}\,\partial\phi_{l_{cl}}}\right|_{\phi_i=0} \qquad \text{for } k, l \in \{1, \ldots, N_S\}\,. \tag{1.20}$$

Consequently, (1.19) transforms into

$$V_{1_S}^{T=0}(\phi_{i_{cl}}) = \frac{1}{2}\int \frac{d^4p}{(2\pi)^4}\,\mathrm{Tr}\left(\ln\left[p^2 + \mathcal{M}_S^2(\phi_{i_{cl}})\right]\right), \tag{1.21}$$

where the trace acts on the field-space indices k, l (cf. (1.20)).
The computational methods of Sec. 1.1.1 and Sec. 1.1.2 can be analogously applied all previous procedures applied to derive the one-loop contribution to the effective potential in theories containing fermions and gauge bosons.

Fermion Fields. For multiple fermion fields ψ_a, describing the fermionic sector of a theory by the Lagrangian $\mathcal{L} = i\overline{\psi}_k\gamma\,\partial\psi^k - \overline{\psi}_k\left(\mathcal{M}_f^2\right)^k_l\,\partial\psi^l$ with $k, l \in \left\{1, \ldots, N_f\right\}$, the mass-matrix elements arise as linear combinations of the Yukawa couplings Γ^k_l to the classical scalar field ϕ_{cl}, $\left(\mathcal{M}_f^2\,(\phi_{cl})\right)^k_l = \Gamma^k_l\,\phi_{cl}$. In this case, the one-loop contribution to the effective potential is calculated to be

$$V_{1_f}^{T=0}(\phi_{cl}) = -\lambda\int \frac{d^4p}{(2\pi)^4}\,\mathrm{Tr}\left(\ln\left[p^2 + \mathcal{M}_f^2(\phi_{cl})\right]\right), \tag{1.22}$$

wherein $\lambda = 1$ for Weyl fermions and $\lambda = 2$ for Dirac fermions [175].

Gauge-Boson Fields. Consider a theory where gauge-bosons are implemented by a contribution $\mathcal{L} = -\frac{1}{4}\mathrm{Tr}\left(F_{\mu\nu}F^{\mu\nu}\right) + \frac{1}{2}\left(D_\mu\phi\right)^\dagger\left(D^\mu\phi\right)$ to the Lagrangian ($F_{\mu\nu}$ denotes the field-strength tensor and D_μ the covariant derivative of the corresponding symmetry group). The gauge-boson one-loop contribution in the Landau gauge, requiring no ghost-field compensating terms yields

$$V_{1_{gb}}^{T=0}(\phi_{cl}) = \frac{3}{2}\int \frac{d^4p}{(2\pi)^4}\,\mathrm{Tr}\left(\ln\left[p^2 + \mathcal{M}_{gb}^2(\phi_{cl})\right]\right). \tag{1.23}$$

---

[4] The zero-temperature one-loop contribution to the effective potential is usually refered to as Coleman-Weinberg contribution since Coleman and E. Weinberg initially performed calculations of the effective potential at one-loop order [65, 205]. Higher order computations were first done by Jackiw [119].

In a theory with scalar, fermion and gauge-boson fields the full finite-temperature one loop contribution at zero-temperature arises as the sum of (1.19), (1.22) and (1.23), multiplied by the degrees of freedom g_i of the corresponding particle. The degrees of freedom g_i constitute the product of the particle's spin-, color- and charge-state degrees.

1.1.4. Renormalization

As the zero-temperature one-loop contributions (1.19), (1.22) and (1.23) are ultraviolet (UV) divergent, we have to apply the conventional renormalization procedure to make the theory finite and hence physically meaningful. In the process of *regularization* the UV divergences are absorbed by appropriate counterterms in the Lagrangian, whereby the parameters of the theory get *renormalized*. The theory written as function of the renormalized parameters is finite. Depending on the choice of renormalization conditions, different renormalization schemes exist.

We will use dimensional regularization which has been introduced by t'Hooft and Veltman [196]. This regularization scheme bases on an analytic continuation procedure of the Feynman integrals to the complex plane in the number of space-time dimensions D, wherein the singularities of the integrals arising as poles in $\frac{1}{D-4}$ have to be subtracted out. By introducing the regulator $\varepsilon > 0$, we can compute the integrals in the zero-temperature one-loop contributions (1.19), (1.22) and (1.23) in $D = 4 - \varepsilon$ dimensions with infinities parametrized by $\frac{1}{\varepsilon}$. The resulting expressions read

$$V_1^{T=0}(\phi_{cl}) = \frac{1}{64\pi^2} \sum_i g_i\, a_i\, m_i^4(\phi_{cl}) \left[\ln\left(\frac{m_i^2(\phi_{cl})}{\mu^2} \right) - C_i - C_{UV} + \mathcal{O}(\varepsilon) \right], \tag{1.24}$$

where the summation index i refers to all bosonic and fermionic particles of the theory and μ^2 denotes the mass scale introduced to balance the dimension of the integration measure. The constants a_i, C_i and C_{UV} are defined as

$$(a_i, C_i) \equiv \begin{cases} \left(1, \frac{3}{2}\right) & \text{for scalars} \\ \left(-2\lambda, \frac{3}{2}\right) & \text{for fermions} \\ \left(3, \frac{5}{6}\right) & \text{for gauge-bosons} \end{cases}, \tag{1.25}$$

$$C_{uv} \equiv \left(\frac{1}{\varepsilon} - \gamma_E + \ln(4\pi) \right), \tag{1.26}$$

containing the Euler-Mascheroni constant $\gamma_E \simeq 0.5772$ [101].

Subsequently, the regularized effective potential of (1.24) has to be renormalized. In the context of effective potentials one usually uses the $\overline{MS}$ (modified minimal subtraction) scheme wherein the divergent term proportional to C_{UV} is absorbed by the counterterms and thus subtracted from the regularized potential,

$$V_1^{T=0}(\phi_{cl}) = \frac{1}{64\pi^2} \sum_i g_i\, a_i\, m_i^4(\phi_{cl}) \left[\ln\left(\frac{m_i^2(\phi_{cl})}{\mu^2} \right) - C_i \right]. \tag{1.27}$$

If we additionally introduce modified degrees of freedom as

$$\bar{g_i} \equiv g_i\, a_i, \tag{1.28}$$

to incorporate the constant a_i,[5] we can summarize the full one-loop contribution to the effective potential at zero-temperature by

$$V_1^{T=0}(\phi_{cl}) = \frac{1}{64\pi^2} \sum_i \bar{g_i}\, m_i^4(\phi_{cl}) \left(\ln\left[\frac{m_i^2(\phi_{cl})}{\mu^2} \right] - C_i \right), \tag{1.29}$$

where the constants C_i are defined in (1.25).

1.2. Effective Potential at Finite Temperature

As conventional quantum field theory describes particle interactions in a surrounding vacuum, it is suitable to be applied to interactions taking place in nearly perfectly shielded accelerators. However, in the early stages of the Universe particles interactions proceeded in a thermal bath of matter and radiation with a non-negligible temperature and density. A description of these interactions thus requires a modification of quantum field theory to incorporate finite-temperature effects.
The formalism of thermal field theory was developed by Weinberg [206], Bernard [33] as well as Dolan and Jackiw [76], while finite-temperature effects in quantum field theory and their cosmological implications (such as inflationary models and phase transitions) were first considered by Kirzhnits and Linde [130, 131, 132, 146, 148].[6]

1.2.1. Generating Functionals and Thermal Green's Functions

The methods of thermal field theory are closely related those of thermodynamics and quantum statistical physics due to the fact that the background state for the particle interactions constitutes a thermal bath at the temperature T of the universe. The finite-temperature generating functionals $Z^T\,[J]$, $W^T[J]$ and $\Gamma^T[\phi_{cl}]$ are defined analogously to the zero-temperature case of Sec. 1.1.1, but include the *thermal* Green's functions defined as grand canonical average of the time-ordered product of the n field operators [175]

$$G^{T\,(n)}(x_1, \ldots, x_n) \equiv \frac{\mathrm{Tr}\left(e^{-\beta H}\, T\{\phi(x_1)\,,\,\ldots\,,\phi(x_n)\}\right)}{\mathrm{Tr}\,(e^{-\beta H})}, \tag{1.30}$$

where $\beta \equiv \frac{1}{T}$. Two particularly appropriate appropriate ways for the computation of the thermal Green's functions are given by the imaginary and real time formalism [31, 126].

---

[5] The introduction of modified degrees of freedom $\bar{g_i}$ will be in particular useful for the summarization of finite-temperature contributions to the effective potential (cf. (1.48) and (1.50)).

[6] Kirzhnits and Linde suggested in particular symmetry restoration to occur in relativistic field theories above a critical temperature T_C by drawing an analogy to the Meissner-Ochsenfeld effect in superconductors [146].

	Zero temperature	**Finite temperature**
Boson propagator	$\frac{i}{p^2-m^2},\ p^\mu = (p_0, \vec{p})$	$\frac{i}{p^2-m^2},\ p^\mu \equiv (i\omega_{b_n}, \vec{p})$
Fermion propagator	$\frac{i}{\gamma\cdot p-m},\ p^\mu = (p_0, \vec{p})$	$\frac{i}{\gamma\cdot p-m},\ p^\mu \equiv (i\omega_{b_n}, \vec{p})$
Loop integral	$\int \frac{d^4p}{(2\pi)^4}$	$iT\ \sum_{n=-\infty}^{\infty} \int \frac{d^3p}{(2\pi)^3}$
Vertex δ-function	$(2\pi)^4\ \delta^{(4)}(\sum_i p_i)$	$\frac{(2\pi)^3}{iT}\ \delta(\sum_i \omega_i)\ \delta^{(3)}(\sum_i \vec{p}_i)$

Table 1.1: *Comparison of Feynman rules at zero temperature and at finite temperature in the imaginary time formalism.* The Matsubara frequencies ω_{b_n} and ω_{f_n} for bosonic and fermionic fields are given by (1.31) and (1.32), respectively.

The basic idea of the *imaginary time formalism* constitutes in expressing the grand canonical averages of the thermal Green's functions as VEVs in ordinary quantum field theory evolved by an imaginary time $t = i\beta$. This results merely in a change of boundary conditions in Minkowski space-time in comparison to the zero-temperature case. In Euclidean space-time however the change of boundary condition entails the remarkable consequence that the thermal Green's functions become periodic for bosonic fields and antiperiodic for fermionic field with period $\beta \equiv \frac{1}{T}$. The periodicity in Euclidean time direction directly implies a replacement of the continuous frequencies ip_0 by the discrete bosonic and fermionic Matsubara frequencies [157]

$$\omega_{b_N} = 2\pi n T, \tag{1.31}$$

$$\omega_{f_n} = (2n+1)\,\pi T, \tag{1.32}$$

and hence a modification of the Feynman rules at finite-temperature. The finite-temperature Feynman rules arising in the imaginary time formalism are summarized in Tab. 1.1.

In the *real time formalism* the straight time contour from real initial time t_i to $t_i - i\beta$ is replaced by a contour from t_i to real final time t_f before going suitable back $t_i - i\beta$. The piecewise composition of the resulting complex time contour leads to more complicated Feynman rules, but avoids the analytic continuations required in the imaginary time formalism. Besides, the propagators computed in the real time formalism are automatically separated into a zero- and finite-temperature part.

Since the propagators and Feynman rules in the imaginary and real time formalism however give the same physical results, we will choose the imaginary time formalism for the computation of the effective potential at finite temperature.

1.2.2. One-Loop Effective Potential at Finite Temperature

In this section we will use the Feynman rules derived in the imaginary time formalism to compute the effective potential at finite temperature up to the one-loop order. Generally,

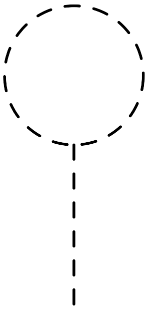

Figure 1.1: *Scalar tadpole diagram.* The derivative of the effective potential $V_{1_S}^T(\phi_{cl})$ in (1.34) with respect to the classical field ϕ_{cl} corresponds to a scalar tadpole diagram.

the one-loop effective potential can be written as the sum of the tree-level potential $V_0(\phi_{cl})$ corrected by the one-loop contribution at finite temperature $V_1^T(\phi_{cl})$,

$$V_{eff}(\phi_{cl}) = V_0(\phi_{cl}) + V_1^T(\phi_{cl})\,. \tag{1.33}$$

As we will explicitly see, the one-loop correction at finite temperature can be separated into a temperature-independent part, equaling exactly the zero-temperature one-loop contribution $V_1^{T=0}(\phi_{cl})$ of Sec. 1.1.2, and a temperature-dependent part $V_1^{T\neq 0}(\phi_{cl})$ which will be computed in the following.

Scalar Fields. According to the finite-temperature Feynman rules, depicted in Tab. 1.1, the zero-temperature one-loop contribution of (1.19) for a single real scalar field transforms into

$$V_{1_S}^T(\phi_{cl}) = \frac{T}{2}\sum_{n=-\infty}^{\infty}\int\frac{d^3p}{(2\pi)^3}\,\ln\left[\omega_{b_n}^2 + \omega^2\right], \tag{1.34}$$

with the bosonic Matsubara frequencies ω_{b_n}, defined in (1.31), and $\omega^2 \equiv \vec{p}^2 + m^2(\phi_{cl})$. Different ways for the evaluation of the above equation exist. The infinite sum can be for instance evaluated by the use of summation identities, whereas a possible solution for the integral is obtained by closing the integration interval in the complex plane to subsequently apply the residues theorem [76].

A subtle way for the evaluation of (1.34) consists however in computing its derivative in the shifted theory, $\frac{dV_{1_S}^T(\phi_{cl})}{d\phi_{cl}}$, and subsequently re-integrating [175]. Diagrammatically the derivative of the effective potential corresponds to the tadpole diagram depicted in Fig. 1.1. Since only the shifted mass $m^2(\phi_{cl})$, included in the definition of ω^2, depends on the classical field ϕ_{cl}, the computation can be equivalently performed with respect to the shifted mass,

$$\frac{dV_{1_S}^T(\phi_{cl})}{dm^2(\phi_{cl})} = \frac{T}{2}\sum_{n=-\infty}^{\infty}\int\frac{d^3p}{(2\pi)^3}\,\frac{1}{\omega_{b_n}^2 + \omega^2}\,. \tag{1.35}$$

By use of several series representations (for details see [175]) the infinite sum can be transformed into an infinite integral which can be computed by analytic continuation to the complex plane. Thereby, the integral naturally separates into a temperature-dependent and a temperature-independent part given by

$$\frac{dV^T_{1_S}(\phi_{cl})}{dm^2(\phi_{cl})} = \frac{1}{2}\int\frac{d^3p}{(2\pi)^3}\left(\frac{1}{2\omega}+\frac{1}{\omega}\,\frac{1}{e^{\frac{\omega}{T}}-1}\right). \tag{1.36}$$

After integration with respect to $m^2(\phi_{cl})$, the final results arises as

$$\begin{aligned} V^T_{1_S}(\phi_{cl}) &= \int\frac{d^3p}{(2\pi)^3}\left(\frac{\omega}{2}+T\;\ln\left[1-e^{-\frac{\omega}{T}}\right]\right) \\ &= \frac{1}{2}\int\frac{d^4p}{(2\pi)^4}\;\ln\left[p^2+m^2(\phi_{cl})\right]+\frac{T^4}{2\pi^2}\,J_B\!\left(\frac{m^2(\phi_{cl})}{T^2}\right) \\ &\equiv V^{T=0}_{1_S}(\phi_{cl})+V^{T\neq0}_{1_S}(\phi_{cl})\,, \end{aligned} \tag{1.37}$$

wherein the temperature-independent part exactly equals the zero-temperature one-loop contribution $V^{T=0}_{1_S}(\phi_{cl})$ of (1.19). The finite-temperature one-loop contribution,[7]

$$V^{T\neq0}_{1_S}(\phi_{cl}) = \frac{T^4}{2\pi^2}\,J_B\!\left(\frac{m^2(\phi_{cl})}{T^2}\right), \tag{1.38}$$

is expressed in terms of the thermal bosonic function $J_B\left(\frac{m^2(\phi_{cl})}{T^2}\right)$ defined as

$$J_B\!\left(\frac{m^2(\phi_{cl})}{T^2}\right) \equiv \int_0^\infty dx\,x^2\;\ln\left[1-e^{-\sqrt{x^2-\frac{m^2(\phi_{cl})}{T^2}}}\right]. \tag{1.39}$$

In the limit $\frac{m^2(\phi_{cl})}{T^2} \ll 1$ the thermal bosonic function can be expanded as

$$\begin{aligned} J_B\!\left(\frac{m^2(\phi_{cl})}{T^2}\right) \simeq &-\frac{\pi^4}{45}+\frac{\pi^2}{12}\,\frac{m^2(\phi_{cl})}{T^2}-\frac{\pi}{6}\left(\frac{m^2(\phi_{cl})}{T^2}\right)^{\frac{3}{2}} \\ &-\frac{1}{32}\left(\frac{m^2(\phi_{cl})}{T^2}\right)^2\;\ln\left[\frac{1}{a_B}\,\frac{m^2(\phi_{cl})}{T^2}\right] \\ &-2\pi^{\frac{7}{2}}\sum_{l=1}^{\infty}(-1)^l\,\frac{\zeta(2l+1)}{(l+1)!}\,\Gamma\!\left(l+\frac{1}{2}\right)\left(\frac{1}{4\pi}\,\frac{m^2(\phi_{cl})}{T^2}\right)^{l+2}, \end{aligned} \tag{1.40}$$

including the constant $a_B \equiv 16\pi^2\,e^{\frac{3}{2}-2\gamma_E}$ as well as the Riemann ζ-function and the Γ-function. Therefore, the finite-temperature one-loop contribution of (1.38) possesses a high-temperature expansion which will be useful for the investigation of phase transitions. Note

---

[7] As in the case of the zero-temperature one-loop contribution a generalization to the case of multiple scalar fields ϕ_{cl_i} is achieved by replacing the shifted mass by the mass matrix $\mathcal{M}^2_S\left(\phi_{cl_i}\right)$ (cf. (1.20)).

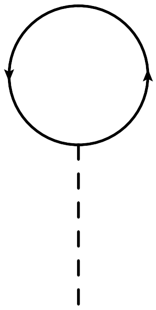

Figure 1.2: *Fermion tadpole diagram.* The depicted tadpole diagram corresponds to the derivative of the effective potential $V_{1_f}^T(\phi_{cl})$ in (1.41) with respect to the classical scalar field ϕ_{cl}.

in particular that the high-temperature expansion of the thermal bosonic function J_B incorporates a monomial cubic mass term $\propto \left(m^2(\phi_{cl})\right)^{3/2}$. This term will be crucial for generating first-order phase transitions as it allows to induce a thermal barrier in the effective potential.

The finite-temperature one-loop contributions to the effective potential for theories containing fermionic and gauge-boson fields can be derived by an analogous calculation procedure.

Fermion Fields. Applying the finite-temperature Feynman rules in the imaginary time formalism, given in Tab. 1.1, to a theory with fermion fields, the zero-temperature one-loop contribution of (1.22) is converted to

$$V_{1_f}^T(\phi_{cl}) = -\lambda\, T \sum_{n=-\infty}^{\infty} \int \frac{d^3p}{(2\pi)^3}\, \ln\left[\omega_{f_n}^2 + \omega^2\right], \tag{1.41}$$

where the fermionic Matsubara frequencies are defined in (1.32) and $\omega^2 \equiv \vec{p}^2 + M_f^2(\phi_{cl})$. In analogy to the case of scalar fields, the one-loop contribution at finite temperature $V_{1_f}^T(\phi_{cl})$ can be evaluated by computing the tadpole diagram of Fig. 1.2 in the shifted theory and re-integrating.Thereof, the final expression for the fermionic one-loop contribution at finite temperature arises as

$$\begin{aligned} V_{1_f}^T(\phi_{cl}) &= -2\lambda \int \frac{d^3p}{(2\pi)^3} \left(\frac{\omega}{2} + T\, \ln\left[1 - e^{-\frac{\omega}{T}}\right]\right) \\ &= -\lambda \int \frac{d^4p}{(2\pi)^4}\, \ln\left[p^2 + M_f^2(\phi_{cl})\right] - \lambda \frac{T^4}{\pi^2}\, J_F\left(\frac{M_f^2(\phi_{cl})}{T^2}\right) \\ &\equiv V_{1_f}^{T=0}(\phi_{cl}) + V_{1_f}^{T\neq 0}(\phi_{cl})\,, \end{aligned} \tag{1.42}$$

including the zero-temperature one-loop contribution $V_{1_f}^{T=0}(\phi_{cl})$ of (1.22). The finite-temperature one-loop contribution

$$V_{1_f}^{T\neq 0}(\phi_{cl}) = -\lambda \frac{T^4}{\pi^2}\, J_F\left(\frac{M_f^2(\phi_{cl})}{T^2}\right) \tag{1.43}$$

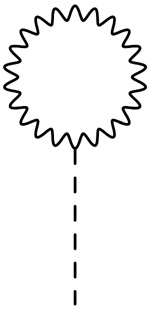

Figure 1.3: *Gauge-boson tadpole diagram.* In a theory with gauge-boson fields the derivative of the effective potential $V_{1_{gb}}^{T}(\phi_{cl})$ with respect to the classical scalar field ϕ_{cl} diagrammatically corresponds to a gauge-boson tadpole diagram.

includes the thermal fermionic function $J_F\left(\frac{M_f^2(\phi_{cl})}{T^2}\right)$ which is defined as (cf. (1.39))

$$J_F\left(\frac{M_f^2(\phi_{cl})}{T^2}\right) \equiv \int_0^\infty dx\, x^2 \,\ln\left[1 + e^{-\sqrt{x^2+\frac{M_f^2(\phi_{cl})}{T^2}}}\right]. \tag{1.44}$$

As the thermal fermionic function can be expanded in the limit $\frac{M_f^2(\phi_{cl})}{T^2} \ll 1$ as

$$\begin{aligned} J_F\left(\frac{M_f^2(\phi_{cl})}{T^2}\right) \simeq & -\frac{7\pi^4}{360} + \frac{\pi^2}{24}\,\frac{M_f^2(\phi_{cl})}{T^2} \\ & - \frac{1}{32}\left(\frac{M_f^2(\phi_{cl})}{T^2}\right)^2 \ln\left[\frac{1}{a_F}\,\frac{M_f^2(\phi_{cl})}{T^2}\right] \\ & - \frac{\pi^{\frac{7}{2}}}{4}\sum_{l=1}^{\infty}(-1)^l\,\frac{\zeta(2l+1)}{(l+1)!}\left(1 - 2^{-2l-1}\right)\Gamma\!\left(l + \frac{1}{2}\right)\left(\frac{1}{\pi^2}\,\frac{M_f^2(\phi_{cl})}{T^2}\right)^{l+2} \end{aligned} \tag{1.45}$$

with constant $a_F \equiv \pi^2\, e^{\frac{2}{3}-2\gamma_E}$, a high-temperature expansion of the fermionic finite-temperature one-loop contribution $V_{1_f}^{T\neq 0}(\phi_{cl})$ in (1.43) exists. Note that the high-temperature approximation of the thermal fermionic function J_F, in contrast to J_B (cf. (1.40)), does not include a cubic term. Therefore, thermally induced barriers in first-order phase transitions arise merely from the bosonic finite-temperature one-loop contribution.

Gauge-Boson Fields. The gauge-boson one-loop contribution to the finite-temperature effective potential is obtained by computing the tadpole diagram of Fig. 1.3 in the shifted theory and re-integrating. After evaluating the tadpole expression the final expression is given by

$$\begin{aligned} V^T_{1_{gb}}(\phi_{cl}) &= \frac{3}{2}\int\frac{d^4p}{(2\pi)^4}\,\ln\left[p^2+M^2_{gb}(\phi_{cl})\right]+3\,\frac{T^4}{2\pi^2}\,J_B\left(\frac{M^2_{gb}(\phi_{cl})}{T^2}\right) \\ &\equiv V^{T=0}_{1_{gb}}(\phi_{cl})+V^{T\neq 0}_{1_{gb}}(\phi_{cl})\,, \end{aligned} \tag{1.46}$$

where the zero-temperature one-loop contribution $V^{T=0}_{1_{gb}}(\phi_{cl})$ equals the expression derived in 1.23, while the finite-temperature one-loop contribution,

$$V^{T\neq 0}_{1_{gb}}(\phi_{cl}) = \frac{T^4}{2\pi^2}\,J_B\left(\frac{M^2_{gb}(\phi_{cl})}{T^2}\right), \tag{1.47}$$

includes the thermal bosonic function J_B, defined in (1.39) and possessing a high-temperature expansion given in (1.40). Note that the finite-temperature one-loop contribution of gauge-boson fields also provides a cubic term $\propto \left(m^2(\phi_{cl})\right)^{3/2}$ due the high-temperature expansion of the thermal bosonic function.

In a theory containing scalar, fermion and gauge-boson fields the finite-temperature one-loop contribution arises as the sum of (1.38), (1.43) and (1.47) multiplied by the degrees of freedom of the single particles. By use of the definition of *modified* degrees of freedom g_i in(1.28) the full finite-temperature one-loop contribution to the effective potential can be summarized as

$$V^{T\neq 0}_{1}(\phi_{cl}) = \frac{T^4}{2\pi^2}\sum_i \bar{g}_i\,J_{F,B}\left(\frac{m_i^2(\phi_{cl})}{T^2}\right), \tag{1.48}$$

wherein the summation index i refers to all bosonic and fermionic particles of the theory.

1.2.3. Ring-Diagram Contributions to the Effective Potential

The emergence of the subleading term of order $\frac{3}{2}$ in the high-temperature expansion of the thermal bosonic function J_B (cf. (1.40)) is a manifestation of the breakdown of perturbative expansion in thermal field theory. At finite temperature infrared (IR) divergences, generated by long-range fluctuations [195], break down the perturbative expansion in terms of small coupling constants. Thus, the finite-temperature one-loop contribution to the effective potential is incomplete as higher-loop corrections of the same order appear in the IR limit [76]. The dominant contribution of these multi-loop corrections arises from the ring diagrams (or so-called daisy diagrams [72]) which constitute N-loop diagrams with $(N-1)$ loops ring attached to the remaining one (cf. Fig. 1.4). The ring diagrams are taken into account in the effective potential by using propagators resummed in the IR limit of vanishing momenta, $\omega_n = \vec{p} = 0$, leading to a shift of the bosonic field-dependent masses $m_i^2(\phi_{cl})$ by the self-energy $\Pi_i(\phi_{cl}, T)$ in the IR limit. Therefore, the field-dependent masses are replavced by *thermal* field-dependent masses (so-called Debye masses) [53],

$$M_i^2(\phi_{cl}, T) \equiv m_i^2(\phi_{cl}) + \Pi_i(\phi_{cl}, T)\,. \tag{1.49}$$

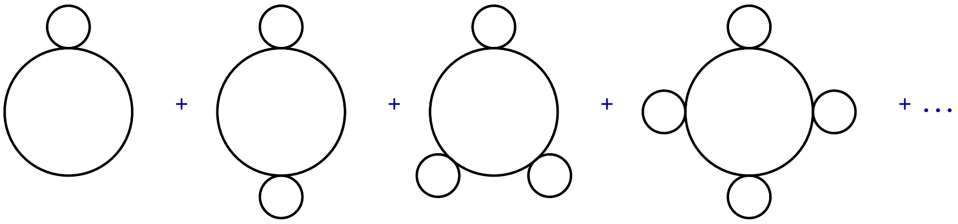

Figure 1.4: *Ring diagrams to leading order.* In this figure, the solid lines of the ring diagrams are assumed to represent scalar, fermion as well as gauge-boson fields. The small loops correspond to thermal loops in the IR limit, being separately IR divergent, but IR finite when summarized.

Note that only the bosonic sector of the theory demonstrates the breakdown of perturbation theory since only the zero-mode of the bosonic Matsubara frequencies $\omega_{b_N} = 2\pi n T$, behaves as a massless degree of freedom and generates IR divergences at high temperature, whereas the fermionic Matsubara frequencies $\omega_{f_n} = (2n+1)\pi T$ for $n = 0$ behave as non-negligible mass contributions of order T. Furthermore, in the IR limit the gauge-boson polarization tensor can be expressed in terms of the longitudinal projection tensor [53]. Consequently, only the longitudinal polarization of the gauge bosons acquire a thermal-mass correction.

In the so-called self-consistent method [25] the ring diagrams are implemented in the effective potential by shifting all Matsubara modes for the bosonic fields by the self-energies. This shift generates a temperature dependency of the UV divergent parts so that the UV behavior of the theory becomes dependent on the IR dynamics what does not introduce calculational errors, but contradicts physical intuition. Alternatively, only the zero-modes of the bosonic Matsubara frequencies $\omega_{b_N} = 0$, incorporating the leading contribution of the ring diagrams at one-loop order, can be shifted. After resummation of zero-mode of the propagator in the IR limit, the ring-diagram contribution to the effective potential reads [72]

$$V_{ring}(\phi_{cl}, T) = -\frac{1}{12\pi} T \sum_{i=bosons} \bar{g}_i \left[\left(M_i^2(\phi_{cl}, T) \right)^{3/2} - \left(m_i^2(\phi_{cl}) \right)^{3/2} \right], \tag{1.50}$$

wherein the summation index i includes all bosonic particles of the model. In particular, the longitudinal and transversal polarizations of the gauge bosons have to be taken into account separately. As the transversal polarizations of the gauge-boson self-energies in the IR limit are zero, $\Pi_{gb_t}(\phi_{cl}, T) \simeq 0$, (1.50) leads only to a thermal shift of the longitudinal polarizations of the gauge bosons.

The ring-diagram contribution to the effective potential modifies the cubic terms by replacing the field-dependent masses by thermal masses and is therefore crucial for the analysis of the phase transition.

1.3. Summarization of Contributions to the Effective Potential

The summarization of the contributions to the effective potential in of (1.29), (1.48) and (1.50) yields the full finite-temperature one-loop effective potential

$$\begin{aligned}
V_{eff}(\phi_{cl}) &= V_0(\phi_{cl}) + V_1^{T=0}(\phi_{cl}) + V_1^{T\neq 0}(\phi_{cl}) + V_{ring}^{T=0}(\phi_{cl}) \\
&= V_0(\phi_{cl}) + \frac{1}{64\pi^2}\sum_i \bar{g}_i\, m_i^4(\phi_{cl})\left(\ln\left[\frac{m_i^2(\phi_{cl})}{\mu^2}\right] - C_i\right) \\
&\quad + \frac{T^4}{2\pi^2}\sum_i \bar{g}_i\, J_{F,B}\left(\frac{m_i^2(\phi_{cl})}{T^2}\right) \\
&\quad - \frac{1}{12\pi} T \sum_{i=bosons} \bar{g}_i \left[\left(M_i^2(\phi_{cl}, T)\right)^{3/2} - \left(m_i^2(\phi_{cl})\right)^{3/2}\right],
\end{aligned} \tag{1.51}$$

including all bosonic and fermionic particles of the theory. The constants C_i and the modified degrees of freedom $\bar{g}_i$ are defined in (1.25) and (1.28), respectively. The above expression will provide the basic formula for the computation of the effective potential in the models investigated in Part II.

Chapter 2

Gravitational Waves from First-Order Phase Transitions

The behavior of the effective potential in dependence on the temperature determines the dynamics of the phase transition. First-order phase transitions, characterized by a barrier separating the metastable symmetric phase and the broken phase,[1] proceed via nucleation of true-vacuum bubbles inside the false-vacuum phase. In this chapter we will review the two main production mechanisms of gravitational waves during first-order phase transitions, namely bubble collisions and turbulence, and provide the necessary equations for the computation of the parameters α and β which characterize the GW spectrum. Finally, we will discuss the GW spectrum from bubble collisions.

2.1. Production Mechanisms of Gravitational Waves during First-Order Phase Transitions

During a first-order phase transition the Universe finds itself in a metastable symmetric phase (the "false vacuum" state) separated from the "true vacuum" broken state by a barrier in the effective potential [167]. The phase transition from the symmetric to the broken state proceeds by nucleation of true-vacuum bubbles inside the "sea" of false vacuum. In *weakly* first-order phase transitions bubble nucleation occurs by quantum tunneling and by thermal

---

[1] According to the *Ehrenfest classification*, the order n of a phase transition corresponds to those lowest-order derivative of the free energy F which is discontinuous with respect to a thermodynamic variable, for instance the temperature T [193, 34]. As the Ehrenfest classification however does not take account of phase transitions where divergences in the derivative of the free energy occur, the *modern classification* [34] distinguishes only between first-order (discontinuous) and second-oder (continuous) phase transitions. Cosmological first-order phase transitions involve in particular a latent heat $L \equiv -T\,\Delta S$ originating from a discontinuity in the entropy $S = \frac{\partial F(T)}{\partial T}$. This discontinuity arises due to a barrier in the effective potential which separates the true and the false vacuum. The emergence of a barrier distinguishes first-order phase transitions from second-order ones, which are for instance considered in the so-called new inflationary models [149, 16, 15].

fluctuations, whereas in *strongly* first-order phase transitions bubbles are merely nucleated via quantum tunneling [156, 103].

If the size of the nucleated bubbles is smaller than a critical size, their volume energy is not sufficient to overcome the shrinking effect of surface tension. However, as the cosmic temperature decreases due to the expansion of the Universe, bubbles which are larger than the critical size can be nucleated below a certain critical temperature T_C. Since the nucleated bubbles in this case start expanding, a part of the energy gained in the transition from the false to the true vacuum is released into the plasma raising its temperature, while the other part is converted into kinetic energy stored close to the bubble walls and bulk motions of the fluid.[2] The bubble wall velocity and energy of the expanding bubbles increase the more regions of space convert to the ground state. Simultaneously, the bubble walls become thinner so that the energy density of the wall grows rapidly. However, the spherical symmetry of the bubbles forbids energy to be directly transferred into gravitational waves [129]. If however two or mores *bubbles collide*, the spherical symmetry is broken allowing to release energy into gravitational radiation. Note that the breaking of spherical symmetry is a necessary condition for gravitational wave production. The emitted radiation does not depend on the internal structure of the colliding bubbles, but only on the kinetic energy stored in the uncollided bubble regions, i.e., it is only dependent on the shape of the uncollided regions [137]. This provides the basis for the so-called envelope approximation [136, 103, 112].

Two possible combustion modes for the energy liberated by the bubble collisions exist. These depend on the strength of the phase transition and hence on the velocity of the bubble walls: If the bubble wall profile propagates slower than the speed of sound, which is $c_S = {}^1\!/\sqrt{3}$ in a relativistic thermal bath, gravitational waves are produced by *deflagration* [194, 137, 138, 136]. However, the amount of kinetic energy stored close to the bubble walls and hence the characteristic bubble wall velocities are so small that gravitational wave production is strongly suppressed [167]. Besides, deflagration is not stable against non-spherical hydrodynamic perturbations [124]. If the bubble boundaries in contrast propagate faster than the speed of sound c_S, the combustion of energy proceeds via *detonation* [194, 125], associated by a large production of gravitational waves. The bubble expansion proceeds via detonation in case of strongly first-order phase transitions (which are required for a detectable GW signal) so that we will restrict our considerations to this combustion mode in the following. Besides, this ensures the thin-wall approximation (cf. Sec. 2.2.2) to be valid (cf. [129]).

Additionally, the bubble expansions cause macroscopic motions in the cosmic plasma. If at least two bubbles collide, anisotropic stirring of the plasma develops at a length scale comparable to the bubble radii at the collision time and *turbulent motions* arise. Turbulent motions constitute another possible mechanism of GW production. [135, 77, 48, 99].

The total stochastic GW background from first-order phase transitions is the sum of the contributions from bubble collisions and turbulent motions. At low frequencies the dominant contribution to the GW spectrum arises from turbulence, whereas the high-frequency part

---

[2] Expanding bubbles constitute a possible source to drive the hot plasma in the early Universe out of equilibrium. Departure from thermal equilibrium is in turn required by the Sakharov conditions for viable baryogenesis.

of the spectrum is mainly determined by the contribution from bubble collisions [167]. For stronger phase transitions the peak frequency of the GW spectrum is shifted to lower frequencies which might lie below the experimentally sensitive range (see for instance [113]). Therefore, the high-frequency part of the GW spectrum dominated by bubble collisions becomes particularly important with regard to detectability.
As the turbulence contribution to the GW spectrum is still discussed and different approaches lead to different peak frequencies, we will focus on the contribution from bubble collisions here.

2.2. Characteristic Parameters of the Gravitational Wave Spectrum

The GW spectrum from first-order phase transitions is generally characterized by two essential parameters, namely $\alpha(T_*)$ and $\beta(T_*)$, evaluated at the tunneling temperature T_* of the phase transition. In the following, we will provide the necessary formulae for the calculation of the parameters α and β which will subsequently determine the GW spectrum.

2.2.1. Parameter α

The parameter α is defined as the ratio of the false-vacuum energy density $\epsilon(T)$ and the thermal energy density $e(T)$ of the symmetric phase [125],

$$\alpha \equiv \frac{\epsilon(T)}{e(T)}. \tag{2.1}$$

Commonly, the symmetric (high-temperature) phase is described by the equation of state of a relativistic gas with thermal energy density

$$e(T) = \frac{\pi^2}{30} g_* T^4. \tag{2.2}$$

Therein, the temperature-dependent quantity g_* counts the total number of *effective* degrees of freedom including only the relativistic particle species with masses $m_i \ll T$ [133],

$$g_* = \sum_{i=bosons} g_i \left(\frac{T_i}{T}\right)^4 + \frac{7}{8} \sum_{i=fermions} g_i \left(\frac{T_i}{T}\right)^4, \tag{2.3}$$

where g_i denotes the degrees of freedom of the corresponding particle (cf. Sec. 1.1.4) and the relative factor $\frac{7}{8}$ originates from the difference in Fermi and Bose statistics. Since the summation only includes those particles with mass $m_i \ll T$, the number of effective degrees of freedom depends on the temperature[3]. For temperatures $T \gtrsim 300\,\text{GeV}$ however, all

---

[3] For most of the evolution of the Universe all particle species had a common temperature T. Only after the decoupling of the neutrinos, i.e., for $T \ll 1\,\text{MeV}$, the neutrino temperature T_ν evolves as $T_\nu = \left(\frac{4}{11}\right)^{1/3} T$ and has to be taken into account separately.

Standard Model particles can be regarded as extremely relativistic. In this case the total number of effective degrees of freedom for the Standard Model yields $g_{*_{SM}} = 106.75$. According to the definition in statistical mechanics, the false-vacuum energy density $\epsilon(T)$, which provides the energy available to be transferred to GWs, [129]

$$\begin{aligned}\epsilon(T) &\equiv \Delta V_{eff}(T) - T\Delta S \\ &= \Delta V_{eff}(T) - T\frac{\partial \Delta V_{eff}(T)}{\partial T}.\end{aligned} \tag{2.4}$$

arises as the Legendre transformation of the difference in free-density

$$\Delta V_{eff}(T) \equiv V_{eff}(\phi_-, T) - V_{eff}(\phi_+, T) \tag{2.5}$$

with ϕ_- and ϕ_+ denoting the false and the true vacuum, respectively. At the critical temperature T_C the false-vacuum energy density equals the latent heat, $L = \epsilon(T_C)$, since the degeneracy of the true and the false vacuum leads to a vanishing potential difference $\Delta V_{eff}(T_C) = 0$,

$$L \equiv -T_C \left.\frac{\partial \Delta V_{eff}(T)}{\partial T}\right|_{T=T_C}. \tag{2.6}$$

between the false vacuum energy (latent heat) density and the plasma thermal energy density, computed at the transition temperature T_*, $\alpha(T_*)$. It gives a measure of the transition strength: For $\alpha \ll 1$ the phase transition is very weak, for $\alpha \sim \mathcal{O}(1)$ the phase transition is very strong.

2.2.2. Parameter β

The second essential parameter for the determination of the GW spectrum, namely β, corresponds to the rate of (time) variation of the bubble nucleation rate Γ itself. Hence, this parameter is related to the duration τ of the phase transition approximately by $\tau \simeq \beta^{-1}$ and to the typical radius of the colliding bubbles, setting the length scale of the problem, by $\langle R\rangle \propto v_b\tau \simeq \frac{v_b}{\beta}$.[4]
At finite temperature the bubble nucleation rate per unit volume is given by [103]

$$\Gamma(t) \sim \Gamma_0(t)\, e^{-S(t)}, \tag{2.7}$$

where the prefactor $\Gamma_0(t) \sim T^4$ and $S(t) \simeq \frac{S_3}{T}$. Therein, S_3 denotes the three-dimensional Euclidean action. Consequently, the parameter β which is defined as [167]

$$\beta \equiv -\left.\frac{dS}{dt}\right|_{t=t_*} \simeq \frac{1}{\Gamma}\left.\frac{d\Gamma}{dt}\right|_{t=t_*}, \tag{2.8}$$

---

[4] Different choices for $\langle R\rangle$ are possible. Using for instance the maximum of the bubble volume distribution in momentum space approximately yields $\langle R\rangle \simeq 5\, v_b\tau$, whereas referring to the size of the largest bubble leads to $\langle R\rangle \simeq v_b\tau$. The different choices of the length scale are one possible cause of the uncertainty in the contribution from turbulence to the GW spectrum [113].

constitutes the logarithmic time derivative of the bubble nucleation rate. If we expand $S(t) \simeq S(t_*) - \beta(t - t_*)$ about the transition time t_* and take the approximate adiabatic expansion of the universe into account, $\frac{dT}{dt} = -T\,H(t)$, where the Hubble parameter $H(t)$ describes the expansion rate of the universe, we obtain from (2.8) the normalized dimensionless parameter

$$\frac{\beta}{H_*} = T_* \frac{d}{dT}\left(\frac{S_3(T)}{T}\right)\bigg|_{T=T_*}, \tag{2.9}$$

whereby T_* is the tunneling temperature of the phase transition In detail, T_* corresponds to the temperature where the probability for nucleating one bubble per horizon volume and time approaches 1, $\frac{\Gamma}{H_*^4} \sim \mathcal{O}(1)$. This guarantees that bubble percolation arises even for an inflationary expansion of the universe [104]. Since the Hubble parameter arises from the Friedmann-Lemaître equations as

$$H_*^2 = \frac{8\pi G}{3}\rho_{tot} = \frac{8\pi^3 g_* T_*^4}{90\,M_{Pl}^2} \tag{2.10}$$

and hence the $H_*^2 \propto \frac{T_*^4}{M_{Pl}^2}$, the condition $\frac{\Gamma}{H_*^4} \sim \mathcal{O}(1)$ translates into $\frac{S_3(T_*)}{T_*} \simeq 4\,\ln\left(\frac{M_{Pl}}{T_*}\right)$. If we assume temperatures of the electroweak scale $T_* \simeq 10^2$ GeV and approximate the Planck mass by $M_{Pl} \simeq 10^{19}$ GeV, the probability of a single bubble to be nucleated in a horizon volume of order $\mathcal{O}(1)$ is well approximated in the Early Universe by

$$\frac{S_3(T_*)}{T_*} \simeq 140. \tag{2.11}$$

Note that the exponential factor of the tunneling probability ensures this approximation to be valid for a broad temperature range [129]. According to $\frac{S_3(T_*)}{T_*} \simeq 4\,\ln\left(\frac{M_{Pl}}{T_*}\right)$, the dimensionless quantity $\frac{\beta}{H_*}$ depends only logarithmically on the temperature scale. While the size of the bubbles increases by orders of magnitude between the nucleation and percolation, the temperature T_* and hence the parameters α and $\frac{\beta}{H_*}$ nearly remain unchanged [104].

Euclidean Action

According to (2.9), it is necessary to compute the Euclidean action $S_3(T)$ to determine the normalized parameter $\frac{\beta}{H_*}$. At zero temperature the Euclidean action reads [150]

$$S_3 \equiv \int d\tau\, d^3x \left[\frac{1}{2}\left(\frac{\partial\phi}{\partial\tau}\right)^2 + \frac{1}{2}\left(\vec{\nabla}\phi\right)^2 + V_{eff}(\phi)\right] \tag{2.12}$$

with Euclidean time τ. In the case of field theory at finite temperature T, the Euclidean field theory is periodic in imaginary time with period $\frac{1}{T}$ (cf. Sec. 1.2.1). As the temperature of the universes decreases by evolution in time, the Euclidean action acquires additionally a dependence on cosmic time t. Therefore, it has to be computed in the space of functions periodic in Euclidean (Wick rotated) time $\tau = it$ so that [23]

$$S_3 = \int_0^{\frac{1}{T}} d\tau\, d^3x \left[\frac{1}{2} \left(\frac{\partial \phi}{\partial \tau} \right)^2 + \frac{1}{2} \left(\vec{\nabla} \phi \right)^2 + V_{eff}(\phi, T) \right], \tag{2.13}$$

where $V_{eff}(\phi, T)$ is the effective potential which has to be shifted to $V_{eff}(0, T) = 0$) for the computation [23]. For large temperatures T however, the Euclidean Action S_3 becomes time-independent. Hence, for tunneling in a thermal system, the $O(4)$ symmetry of (2.13) is replaced by an O(3) symmetry and the corresponding Euclidean action reads

$$\begin{aligned} S_3(T) &= \int d^3x \left[\frac{1}{2} \left(\vec{\nabla} \phi \right)^2 + V_{eff}(\phi, T) \right] \\ &= 4\pi \int_0^{\infty} d\varrho\, \varrho^2 \left[\frac{1}{2} \left(\frac{\partial \phi(\varrho)}{\partial \varrho} \right)^2 + V_{eff}(\phi(\varrho)\,, T) \right], \end{aligned} \tag{2.14}$$

where we have assumed spherical symmetry by defining $\varrho \equiv \sqrt{\vec{x}^2}$ in the last step.
In the semi-classical theory of tunneling [63, 47, 150], the tunnel probability depends on the action of the so-called bounce solution. This configuration fulfills the classical Euclidean equation of motion. In the case of tunneling at finite temperature the equation of motion is given by [10, 147, 150]

$$\frac{d^2\phi}{d\phi^2} + \frac{\gamma}{\varrho} \frac{d\phi}{d\varrho} = \frac{dV_{eff}(\phi, T)}{d\phi} \tag{2.15}$$

with damping coefficient $\gamma = 2$.[5] It has to be solved for the *inverted* potential and the boundary conditions

$$\left. \frac{d\phi(\varrho)}{d\varrho} \right|_{\varrho=0} = 0, \qquad \lim_{\varrho \to \infty} \phi(\varrho) = \phi_-, \tag{2.16}$$

where ϕ_- denotes the symmetric minimum (false vacuum) of the potential $V_{eff}(\phi, T)$.
By generalizing the thermal case to n scalar fields, $\vec{\phi} \equiv (\phi_1, \ldots, \phi_n)$, (2.14) transforms into

$$S_3(T) = 4\pi \int_0^{\infty} d\varrho\, \varrho^2 \left[\frac{1}{2} \left(\frac{\partial \vec{\phi}(\varrho)}{\partial \varrho} \right)^2 + V_{eff}\left(\vec{\phi}(\varrho)\,, T \right) \right], \tag{2.17}$$

where $\left(\frac{\partial \vec{\phi}(\varrho)}{\partial \varrho} \right)^2 = \sum_{i=1}^{n} \left(\frac{\partial \phi_n(\varrho)}{\partial \varrho} \right)^2$. The corresponding n equations of motion

$$\frac{d^2\vec{\phi}}{d\phi^2} + \frac{2}{\varrho} \frac{d\vec{\phi}}{d\varrho} = \vec{\nabla} V_{eff}\left(\vec{\phi}, T \right) \tag{2.18}$$

with $\vec{\nabla} = \left(\frac{\partial}{\partial \phi_1}, \ldots, \frac{\partial}{\partial \phi_n} \right)$ can be interpreted as classical particle moving in the n-dimensional inverted potential with a time-dependent damping term [134].

---

[5] In the case of tunneling in vacuum the damping coefficient equals $\gamma = 3$.

Thin-Wall Approximation. If the bubble radius $R(T)$ becomes much larger than the thickness of the wall $d \equiv \partial_\phi^2 V_{eff}(\phi, T)\Big|_{\phi=\phi_+}$ [102], $R(T) \gg d$, it is possible to neglect the second term in the equation of motion (2.15). In this thin-wall regime, where the maxima of the inverted potential are almost degenerate, $V_{eff}(\phi_+, T) \simeq V_{eff}(\phi_-, T)$, the finite-temperature Euclidean action of (2.14) can be approximated by [150]

$$S_3(T) = -\frac{4\pi}{3} R(T)^3 \, \Delta V_{eff}\,(T) + 4\pi \, R(T)^2 \, S_1(T)\,, \tag{2.19}$$

where $\Delta V_{eff}\,(T)$, defined in 2.5, denotes the difference between the two maxima of the inverted potential and

$$\begin{aligned} S_1 &= \int_0^\infty d\varrho \left[\frac{1}{2} \left(\frac{\partial \phi(\varrho)}{\partial \varrho} \right)^2 + V_{eff}(\phi(\varrho)\,, T) \right] && (2.20) \\ &\simeq \int_{\phi_+}^{\phi_-} d\phi \, \sqrt{2V(\phi(\varrho))} && (2.21) \end{aligned}$$

is the one-dimensional Euclidean action $S_1(T)$ in the thin-wall approximation. As the temperature-dependent radius of the bubble, determined according to Hamilton's principle of least action by variation of (2.19), is given by

$$R(T) = \frac{2\,S_1(T)}{\Delta V_{eff}\,(T)}, \tag{2.22}$$

an explicit expression for the three-dimensional Euclidean action at finite temperature can be derived by inserting (2.22) in (2.19),[6]

$$S_3(T) = \frac{16\pi S_1(T)^3}{3\left(\Delta V_{eff}\,(T)\right)^2}. \tag{2.23}$$

Note that equating (2.11) and (2.23) allows to directly determine the tunneling temperature T_*. Furthermore, (2.11) can be used to derive for the parameter $\frac{\beta}{H_*}$ the expression (cf. (2.9))

$$\begin{aligned} \frac{\beta}{H_*} &\equiv T_* \frac{d}{dT} \left(\frac{S_3(T)}{T} \right) \Bigg|_{T=T_*} \\ &= -\frac{S_3(T_*)}{T_*} \left(1 + 2 \frac{T_*}{\Delta V_{eff}(T_*)} \, \frac{d\Delta V_{eff}(T)}{dT} \Bigg|_{T=T_*} \right) \\ &\simeq -280 \, \frac{T_*}{\Delta V_{eff}(T_*)} \, \frac{d}{dT} \left(\frac{\Delta V_{eff}(T_*)}{T_*} \right) \Bigg|_{T=T_*} \,, \end{aligned} \tag{2.24}$$

---

[6] By an analogously performed calculation the three-dimensional Euclidean action at zero temperature in the thin-wall approximation emerges as

$$S_3 = \frac{27\pi^2 S_1(T)^4}{3\left(\Delta V_{eff}\,(T)\right)^3}.$$

where we have assumed in the second step that the term corresponding to the logarithmic derivative of $\frac{\Delta V_{eff}(T_*)}{T_*}$ is the dominant contribution in the sum. (We will see explicitly in Sec. 4.5 and Sec. 4.6 that this is justified.)

2.2.3. Parameters v_b and κ

Apart from α and β, two additional parameters are in principle needed for determining the GW spectrum from bubble collisions, namely the expansion velocity v_b of the bubble walls and the fraction κ of false-vacuum energy density (latent heat) transformed into fluid kinetic energy (bulk motion) instead of heating the plasma. In general, the determination of v_b and κ requires to take friction effects into account due to departures from thermal equilibrium in the vicinity of the bubble walls [198, 165, 120]. However, in the case of denotation, where the bubble walls propagate faster than the speed of sound, these quantities are merely functions of α, $v_b(\alpha)$ and $\kappa(\alpha)$, independently on the microphysics driving the phase transition [167]. For strongly first-order phase transitions the velocity of the bubble walls in the case of detonation is approximately given by [194]

$$v_b(\alpha) = \frac{\frac{1}{\sqrt{3}} + \sqrt{\alpha^2 + \frac{2}{3}\alpha}}{1+\alpha}, \tag{2.25}$$

constituting an increasing function in terms of α which varies between the speed of sound $c_S = \frac{1}{\sqrt{3}}$ (in a relativistic thermal bath) and the speed of light $c = 1$. As the exact value of v_b however is dependent on the underlying theory (v_b may be affected for instance by particle scatterings with the bubble wall) , we will assume for the purpose of this work

$$v_b(\alpha) \simeq 1. \tag{2.26}$$

(As we require strongly first-order phase transitions to allow for a detectable GW signal, this constitutes an appropriate assumption.)
The efficiency factor $\kappa(\alpha)$, indicating the ratio of false vacuum-energy density transferred into kinetic energy of the bulk fluid, can be determined numerically as a function of the parameter α yielding [125]

$$\kappa(\alpha) \simeq \frac{1}{1+0.715\,\alpha}\left(0.715\,\alpha + \frac{4}{27}\sqrt{\frac{3}{2}\,\alpha}\right). \tag{2.27}$$

The efficiency $\kappa(\alpha)$ increases with the enlargement of α by varying between $\kappa(\alpha) = 0 \ldots 1$. As (2.27) is only approximately numerically determined and we require strongly first-order phase transitions, we will assume in the following

$$\kappa(\alpha) \simeq 1. \tag{2.28}$$

2.3. Gravitational Wave Spectrum from Bubble Collisions

The GW spectrum is in general expressed in terms of the energy density of gravitational waves ρ_{GW} per logarithmic frequency interval, normalized to the critical energy density ρ_C for a close universe [156, 167]

$$\Omega_{GW}(f) \equiv \frac{1}{\rho_C}\frac{d\rho_{GW}}{d\ln(f)}. \tag{2.29}$$

As the critical energy density, arising from the Friedmann-Lemaître equations as

$$\rho_C = \frac{3H_0^2}{8\pi G}, \tag{2.30}$$

incorporates an experimental uncertainty in the Hubble parameter $H_0 = h_0 \cdot 100\,\frac{\mathrm{km}}{\mathrm{s{\cdot}Mpc}}$ (with h_0 parametrizing the experimental uncertainty), the GW spectrum is usually described by the dimensionless quantity $h_o^2\Omega_{GW}(f)$.
In the following, we will first derive the peak frequency $\tilde{f}$ and the peak amplitude $\tilde{\Omega}_{GW}$ of the GW spectrum, which have been redshifted from the time (or equivalently the temperature) of their production during the phase transition to the present time. Subsequently, we will express the GW spectrum $h_o^2\Omega_{GW}(f)$, which is observable today, in terms of $\tilde{f}$ and $\tilde{\Omega}_{GW}$.

Peak frequency $\tilde{f}$. If we work in the Friedmann-Robertson-Walker (FRW) metric including the cosmological scale factor $a(T)$ and assume a radiation-dominated Universe at the time of the phase transition, the frequency scales as $a(T)^{-1}$. Therefore, the redshifted frequency of the gravitational waves, produced at the temperature T_* with a frequency f_*, arises at the present time as

$$f = \frac{a(T_*)}{a(T_0)}\, f_* = \left(\frac{g_{S_0}}{g_*}\right)^{\frac{1}{3}} \frac{T_0}{T_*}\, f_*, \tag{2.31}$$

where we used the fact that the entropy per comoving volume remains constant in an adiabatic expanding Universe, $S(T) \propto a(T)^3\, g_S(T)\, T^3$. Thereby, the relativistic degrees of freedom g_S related to the entropy $S(T)$ (not to the thermal energy density $e(T)$) emerge from (2.3) by replacing the quartic power terms of T by a cubic ones. At the present time the relativistic degrees of freedom are $g_S(T_0) \simeq 3.91$ (for three neutrino species) [103], whereas the temperature of the cosmic microwave background (CMB) is given by $T_0 = 2.725\,\mathrm{K} = 2.348 \cdot 10^{-13}\,\mathrm{GeV}$ [92]. Inserting this in (2.31) and expressing the frequency f_* in terms of the Hubble parameter H_* yields the redshifted frequency observed today

$$f \simeq 6 \cdot 10^{-3}\,\mathrm{mHz}\left(\frac{f_*}{H_*}\right)\left(\frac{T_*}{100\,\mathrm{GeV}}\right)\left(\frac{g_*}{100}\right)^{\frac{1}{6}}. \tag{2.32}$$

Using this relation, the peak frequency of the GW spectrum at the present time emerges as

$$\tilde{f} = 16.5 \cdot 10^{-3}\,\mathrm{mHz} \left(\frac{f_*}{\beta}\right)\left(\frac{\beta}{H_*}\right)\left(\frac{T_*}{100\,\mathrm{GeV}}\right)\left(\frac{g_*}{100}\right)^{\frac{1}{6}}, \tag{2.33}$$

where the function $\frac{f_*}{\beta}$ is numerically approximated as [112]

$$\frac{\tilde{f}_*}{\beta} \simeq \frac{0.62}{1.8 - 0.1\, v_b(\alpha) + v_b^2(\alpha)}. \tag{2.34}$$

As we assume $v_b(\alpha) \simeq 1$ where $\frac{\tilde{f}_*}{\beta} \simeq 0.23$, the peak frequency $\tilde{f}$ in dependency of the characteristic parameter $\frac{\beta}{H_*}$, the tunneling temperature T_* and the degrees of freedom g_* finally reads

$$\tilde{f} = 3.79 \cdot 10^{-3}\,\mathrm{mHz} \left(\frac{\beta}{H_*}\right)\left(\frac{T_*}{100\,\mathrm{GeV}}\right)\left(\frac{g_*}{100}\right)^{\frac{1}{6}}. \tag{2.35}$$

Note that if we assume the phase transition to proceed at the electroweak scale $T_* \simeq 10^2$ GeV and choose typical values for the other parameters, $\frac{\beta}{H_*} \simeq 10^2 \ldots 10^3$ and $g_* \simeq 100$, the resulting peak frequency is $\tilde{f} = 0.5 \ldots 10\,\mathrm{mHz}$ [103], which remarkably coincides with the most sensitive frequency range of the GW detector LISA (cf. Chap. C).

Peak amplitude $\tilde{\Omega}_{GW}$. In the FRW metric the energy density scales like $a(T)^{-4}$ [103], whereas the critical energy density evolves as $H(T)^2$ (cf. (2.30)),

$$\rho_{GW} = \left(\frac{a(T_*)}{a(T_0)}\right)^4 \rho_{GW_*}, \quad \rho_C = \left(\frac{H_0}{H_*}\right)^2 \rho_{C_*}. \tag{2.36}$$

Using these relations and the expression for the Hubble parameter from the Friedmann-Lemaître equations of (2.10), the gravitational waves, which have been produced at the temperature T_* with a peak amplitude $\tilde{\Omega}_{GW_*}$, arise at present time with a peak amplitude (cf. (2.29))

$$\begin{aligned} \tilde{\Omega}_{GW} &= \left(\frac{a(T_*)}{a(T_0)}\right)^4 \left(\frac{H_*}{H_0}\right)^4 \tilde{\Omega}_{GW_*} \\ &\simeq 1.67 \cdot 10^{-5} \left(\frac{100}{g_*}\right)^{\frac{1}{3}} \frac{1}{h_0^2}\, \tilde{\Omega}_{GW_*}. \end{aligned} \tag{2.37}$$

Since the peak amplitude $\tilde{\Omega}_{GW_*}$ of the gravitational waves at the time of the proceeding of the phase transition can be written as [125]

$$\tilde{\Omega}_{GW_*} = \tilde{\Delta}\, \kappa(\alpha)^2 \left(\frac{H_*}{\beta}\right)^2 \left(\frac{\alpha}{\alpha+1}\right)^2, \tag{2.38}$$

the peak amplitude which would be observed today is obtained by redshifting from (2.37),

$$\begin{aligned} h_o^2\tilde{\Omega}_{GW} &= 1.67\cdot 10^{-5}\,\tilde{\Omega}_{GW_*}\left(\frac{100}{g_*}\right)^{\frac{1}{3}} \\ &= 1.67\cdot 10^{-5}\,\tilde{\Delta}\,\kappa(\alpha)^2\left(\frac{H_*}{\beta}\right)^2\left(\frac{\alpha}{\alpha+1}\right)^2\left(\frac{100}{g_*}\right)^{\frac{1}{3}}. \end{aligned} \tag{2.39}$$

Therein, the dimensionless function $\tilde{\Delta}$ has to be determined numerically. According to [112], it is approximately given by

$$\tilde{\Delta}\simeq\frac{0.11\,v_b^3(\alpha)}{0.42+v_b^2(\alpha)}, \tag{2.40}$$

yielding $\tilde{\Delta}\simeq 0.08$ for $v_b(\alpha)\simeq 1$. Assuming additionally $\kappa(\alpha)\simeq 1$, (2.39) finally leads to the expression

$$h_o^2\tilde{\Omega}_{GW} = 1.29\cdot 10^{-6}\left(\frac{H_*}{\beta}\right)^2\left(\frac{\alpha}{\alpha+1}\right)^2\left(\frac{100}{g_*}\right)^{\frac{1}{3}} \tag{2.41}$$

for the peak amplitude of the GW spectrum.

Graviational Wave Spectrum from Bubble Collisions

Following [112], we parametrize the GW spectrum $\Omega_{GW_*}(f_*)$ generated by bubble collisions during a first-order phase transition in the envelope approximation as

$$\Omega_{GW_*}(f_*) = \tilde{\Omega}_{GW_*}\,\frac{(a+b)\;\tilde{f}_*^b\;f_*^a}{b\,\tilde{f}_*^{(a+b)}+a\,f_*^{(a+b)}}, \tag{2.42}$$

where the exponents lie in the range $a\in[2.66,\,2.82]$ and $b\in[0.90,\,1.19]$. For a strongly first-order phase transition with $v_b(\alpha)\simeq 1$, the numerical simulation for a large number of colliding bubbles in [112] yields $a\simeq 2.8$ and $b\simeq 1.0$ so that the GW spectrum rises as $f_*^{3.0}$ for low frequencies and falls off as $f_*^{-1.0}$ for high frequencies. Note that the decrease of the GW spectrum including multi-bubble collisions is considerably slighter than in the case of two colliding bubbles where the spectrum falls off as $f_*^{-1.8}$ [125].
With $a\simeq 2.8$ and $b\simeq 1.0$ and by redshifting the peak frequency and amplitude according (2.35) and (2.41), the GW spectrum which is observed at the present time reads

$$h_o^2\Omega_{GW}(f) = h_o^2\tilde{\Omega}_{GW}\,\frac{3.8\cdot\tilde{f}\,f^{2.8}}{\tilde{f}^{3.8}+2.8\cdot f^{3.8}} \tag{2.43}$$

with

$$h_o^2\tilde{\Omega}_{GW} = 1.29\cdot 10^{-6}\left(\frac{H_*}{\beta}\right)^2\left(\frac{\alpha}{\alpha+1}\right)^2\left(\frac{100}{g_*}\right)^{\frac{1}{3}}, \tag{2.44}$$

$$\tilde{f} = 3.79\cdot 10^{-3}\,\mathrm{mHz}\left(\frac{\beta}{H_*}\right)\left(\frac{T_*}{100\,\mathrm{GeV}}\right)\left(\frac{g_*}{100}\right)^{\frac{1}{6}}. \tag{2.45}$$

The peak amplitude $h_o^2\tilde{\Omega}_{GW}$ of the GW spectrum is independent of the tunneling temperature T_* and hence does not depend on the energy scale of the phase transition. As the peak amplitude includes however the dimensionless parameters α and $\frac{\beta}{H_*}$, it rather depends on the *shape* of the effective potential at the temperature T_*, but not on T_* itself. The parameters α and $\frac{\beta}{H_*}$ are correlated by their dependence on $\Delta V_{eff}(T_*)$. In detail, bigger values of $\Delta V_{eff}(T_*)$ lead to an increase of the parameter α (cf. (2.4)) and a simultaneous decrease of $\frac{\beta}{H_*}$ (cf. (2.24)). For generating a peak amplitude within the experimentally accessible sensitivity range, α and $\frac{\beta}{H_*}$ roughly have to be of order [103]

$$\alpha \sim \mathcal{O}(1)\,, \qquad \frac{\beta}{H_*} \sim \frac{S_3(T_*)}{T_*} \sim \mathcal{O}(100)\,. \tag{2.46}$$

Stronger phase transitions generally lead to a decrease of the parameters T_* and $\frac{\beta}{H_*}$ (and hence an increase of α) [113, 112]. The equations (2.44) and (2.45) display explicitly that the peak amplitude $h_o^2\tilde{\Omega}_{GW}$ is consequently enlarged, whereas the peak frequency $\tilde{f}$ is lowered. For a detection of the GW spectrum it is required that both, the peak amplitude $h_o^2\tilde{\Omega}_{GW}$ as well as the peak frequency $\tilde{f}$, lie in the experimentally accessible region. Our intention will be therefore to consider phase transitions which are required to be *strongly first-order*, generating a high peak amplitude $h_o^2\tilde{\Omega}_{GW}$, and which additionally proceed at *high temperatures* ($T_{EW} < T_* < T_{GUT}$), shifting the peak frequency $\tilde{f}$ to the high-frequency range.

In Part II, we will investigate whether the gravitational waves from the first-order phase transitions in two extensions of the Standard Model will be detectable under these conditions and hence could serve as cosmological probes for the theoretical conception of the models. Thereby, the formulae in (2.43), (2.44) and (2.45) will constitute our main equations for the calculation of the GW spectra.

Part II.

Models

Chapter 3

Singlet Extension of the Standard Model

In this part we will study first-order phase transitions in two extensions of the Standard Model to investigate their possibility of providing detectable gravitational waves. The first model we will consider will be the minimal extension of the Standard Model by a real scalar gauge singlet S. Although there exists a large variety of Standard Model extensions, the importance of this model lies in the fact that many extensions contain hidden sectors whose elements transform non-trivially under a hidden sector gauge group, but as singlets under the Standard Model group [83, 84]. Since the only renormalizable interactions of such scalars occur via the Standard Model Higgs sector, these interactions can serve as window ("portal") into the hidden sector [186, 170, 38]. In the following, we will therefore assume the additional singlet S to couple only to the Standard Model Higgs doublet Φ.

3.1. Tree-Level Scalar Potential

In the singlet extension of the Standard Model the Lagrangian of the Higgs and singlet sector is given by

$$\mathcal{L}_{\Phi,S} = \left(D_\mu \Phi\right)^\dagger (D^\mu \Phi) + \frac{1}{2}\left(\partial_\mu S\right)(\partial^\mu S) - V_0(\Phi, S)\,, \tag{3.1}$$

where $D_\mu \equiv \partial_\mu + i\frac{g}{2}\sigma_a A_\mu^a + i\frac{g'}{2} Y B_\mu$ is the covariant derivative of the Standard Model $SU(2)_L \otimes U(1)_Y$ gauge group [176, 174]. The complex Higgs doublet

$$\Phi = \frac{1}{\sqrt{2}} \begin{pmatrix} \chi_1 + i\chi_2 \\ h + i\chi_3 \end{pmatrix} \tag{3.2}$$

contains the physical scalar Higgs field h and the three massless Goldstone fields $\chi_{1,2,3}$. $V_0(\Phi, S)$ denotes the tree-level potential consisting of the Standard Model Higgs potential

$V_H(\Phi) = -\mu_h^2 \left(\Phi^\dagger\Phi\right) + \lambda_h \left(\Phi^\dagger\Phi\right)^2$ with $\mu_h^2 > 0$ and $\lambda_h > 0$, a Higgs-singlet contribution $V_{HS}(\Phi, S)$ and a pure singlet potential $V_S(S)$. The most general (renormalizable) ansatz for the tree-level potential consists in [26, 82]

$$\begin{aligned} V_0(\Phi, S) &= V_H(\Phi) + V_{HS}(\Phi, S) + V_S(S) \\ &= -\mu_h^2 \left(\Phi^\dagger\Phi\right) + \lambda_h \left(\Phi^\dagger\Phi\right)^2 \\ &\qquad + \frac{a_1}{2} \left(\Phi^\dagger\Phi\right) S + \frac{a_2}{2} \left(\Phi^\dagger\Phi\right)^2 S^2 \\ &\qquad + b_1 S + \frac{b_2}{2} S^2 + \frac{b_3}{3} S^3 + \frac{b_4}{4} S^4 , \end{aligned} \tag{3.3}$$

where we require all parameters to be real.[1] To obtain the tree-level *scalar* potential in terms of the physical Higgs field h and the singlet S, the complex Higgs doublet Φ of (3.2) has to be expanded about its (zero-temperature) VEV [171, 174]

$$\langle\Phi\rangle = \frac{1}{\sqrt{2}} \begin{pmatrix} 0 \\ v \end{pmatrix} \tag{3.4}$$

so that $\Phi^\dagger\Phi = |\Phi|^2 = \frac{1}{2}(v+h)^2$. Inserting this in (3.3) and removing the field-independent (and hence physically unimportant) constant terms, yields the scalar tree-level potential $V_0(h, S)$. If we require additionally the potential to be invariant under the discrete $\mathbb{Z}_2$ symmetry transformation $S \to -S$, the odd-power terms in S vanish. Hence, the scalar tree-level potential takes the form

$$V_0(h, S) = -\frac{\mu_h^2}{2} h^2 + \frac{\lambda_h}{4} h^4 - \frac{\mu_S^2}{2} S^2 + \frac{\lambda_S}{4} S^4 + \frac{\lambda_m}{4} h^2 S^2 , \tag{3.5}$$

where we have redefined $a_2 \equiv \lambda_m$, $b_2 \equiv -\mu_S^2$ and $b_4 \equiv \lambda_S$ (with $\mu_S^2 > 0$, $\lambda_S > 0$). The real parameter λ_m is generally not restricted to be either positive or negative. In our further considerations we will assume $\lambda_m > 0$.

The singlet S is stable until thermal fluctuations induce the spontaneous breaking of the $\mathbb{Z}_2$ symmetry which is associated by a phase transition. To investigate this phase-transition scenario, we will next compute the effective potential.

3.2. Effective Potential

We will determine the effective potential in the singlet extension of the Standard Model up to the one-loop order at finite temperature by including the zero-temperature Coleman-Weinberg contributions $V_1^{T=0}(h, S)$, the finite-temperature corrections $V_1^{T\neq 0}(h, S)$ and the contributions $V_{ring}(h, S)$ from the ring diagrams. The tree-level potential corrected by these terms composes the full one-loop finite-temperature effective potential (cf. (1.51))

$$V_{eff}(h, S, T) = V_0(h, S) + V_1^{T=0}(h, S) + V_1^{T\neq 0}(h, S, T) + V_{ring}(h, S, T) . \tag{3.6}$$

We start with computing the zero-temperature Coleman-Weinberg contributions $V_1^{T=0}(h, S, T)$.

---

[1] The normalization factors of the parameters are chosen with regard to the simplicity of the Higgs and singlet couplings arising from the tree-level potential.

3.2.1. One-Loop Effective Potential at Zero Temperature

According to (1.29), the one-loop correction to the tree-level potential at zero temperature in the $\overline{MS}$ renormalization scheme is given by

$$V_1^{T=0}(h,S) = \frac{1}{64\pi^2} \sum_i \bar{g}_i \, m_i^4(\phi_{cl}) \left(\ln \left[\frac{m_i^2(h,S)}{\mu^2} \right] - C_i \right), \tag{3.7}$$

where the constants C_i and the modified degrees of freedom $\bar{g}_i$ are defined in (1.25) and (1.28), respectively. Hereby, the summation over the index i includes all particles of the model, i.e. the Standard Model fermions and bosons as well as the additional S-boson. Since the dominant mass contributions will emerge from the top quark t, the gauge bosons $W^\pm$ and Z, the Goldstone bosons $\chi_{1,2,3}$, the Higgs h and the singlet S, we will restrict our considerations to the latter and neglect all other (fermionic) particle contributions in the following.

To compute the one-loop contribution $V_1^{T=0}(h,S)$ of (3.7), we have to determine the modified degrees of freedom g_i and the field-dependent masses $m_i(h,S)$ for the considered particles.

The degrees of freedom arise as the product of the particle's spin-, color- and charge-state degrees. According to (1.28) in Sec. 1.1.3, the modified degrees of freedom for the regarded particles are

$$\begin{aligned} \bar{g}_t &= -12, & \bar{g}_\chi &= 3, \\ \bar{g}_W &= 6, & \bar{g}_h &= 1, \\ \bar{g}_Z &= 3, & \bar{g}_S &= 1. \end{aligned} \tag{3.8}$$

Note that we have used the modified degrees of freedom to by absorb the prefactor (-1) of the zero-temperature one-loop contribution for the top quark.

Due to the restriction of the S-boson coupling to the Higgs field, the field-dependent masses for the top quark t and the gauge bosons $W^\pm$, Z are independent of the singlet field and hence remain unchanged in comparison to the Standard Model [176]

$$\begin{aligned} m_t^2(h) &= \frac{y_t^2}{2} h^2, \\ m_W^2(h) &= \frac{g^2}{4} h^2, \\ m_Z^2(h) &= \frac{g^2 + g'^2}{4} h^2, \end{aligned} \tag{3.9}$$

where y_t denotes the top-quark Yukawa coupling, while g and g' are the $SU(2)_L$- and $U(1)_Y$-couplings of the Standard Model gauge group, respectively.[2]

The field-dependent masses of the Goldstone bosons $\chi_{1,2,3}$, the Higgs h and the singlet S are

---

[2] At high temperatures the Z-boson and the photon are not mass eigenstates. As discussed in [72], treating them as such in the computation however gives the correct results.

on the contrary affected by the Higgs-singlet interactions. They are derived as eigenvalues of the field-dependent mass matrix $\mathcal{M}^2(h,S)$, defined in (1.20), with respect to the tree-level potential $V_0(h,S)$. The diagonalization of the mass matrix

$$\mathcal{M}^2(h,S) = \begin{pmatrix} m^2_{hh}(h,S) & m^2_{hS}(h,S) \\ m^2_{Sh}(h,S) & m^2_{SS}(h,S) \end{pmatrix} \equiv \begin{pmatrix} \frac{\partial^2 V_0(h,S)}{\partial h^2} & \frac{\partial^2 V_0(h,S)}{\partial h\,\partial S} \\ \frac{\partial^2 V_0(h,S)}{\partial S\,\partial h} & \frac{\partial^2 V_0(h,S)}{\partial S^2} \end{pmatrix}, \tag{3.10}$$

whose elements are given by

$$\begin{aligned} m^2_{hh}(h,S) &= -\mu_h^2 + 3\lambda_h h^2 + \frac{\lambda_m}{2} S^2, \\ m^2_{SS}(h,S) &= -\mu_S^2 + 3\lambda_S S^2 + \frac{\lambda_m}{2} h^2, \\ m^2_{hS}(h,S) &= m^2_{hS}(h,S) = \lambda_m hS, \end{aligned} \tag{3.11}$$

yields the physical Higgs and singlet eigenmasses

$$\begin{aligned} m^2_{h,S}(h,S) &= \frac{1}{2}\left\{m^2_{hh}(h,S) + m^2_{SS}(h,S) \mp \sqrt{\left[m^2_{hh}(h,S) - m^2_{SS}(h,S)\right]^2 + 4\,m^2_{hS}(h,S)}\right\} \\ &= \frac{1}{2}\left\{-\mu_h^2 - \mu_S^2 + \left(3\lambda_h + \frac{\lambda_m}{2}\right) h^2 + \left(3\lambda_S + \frac{\lambda_m}{2}\right) S^2 \right. \\ &\qquad \left. \mp \sqrt{\left[-\mu_h^2 + \mu_S^2 + \left(3\lambda_h - \frac{\lambda_m}{2}\right) h^2 - \left(3\lambda_S - \frac{\lambda_m}{2}\right) S^2\right]^2 + 4\,\lambda_m\, hS}\,\right\}. \end{aligned} \tag{3.12}$$

The field-dependent masses of the Goldstone bosons equal the pure Higgs contribution in the mass matrix , $m^2_\chi(h,S) = m^2_{hh}(h,S)$.

Thus, we have determined the Coleman-Weinberg contribution $V_1^{T=0}(h,S)$ in the singlet extension of the Standard Model by the degrees of freedom of (3.8) and the field-dependent masses of (3.9) and (3.12). Next, we will have to derive the finite-temperature one-loop contribution $V_1^{T\neq 0}(h,S,T)$.

3.2.2. One-Loop Effective Potential at Finite Temperature

Since we will investigate the phase transition in the singlet model for temperatures between the electroweak and the GUT scale, it is justified to use the high-temperature expansion $\left(m_i^2(h,S) \ll T^2\right)$ of the finite-temperature one-loop contribution (cf. (3.32)),

$$V_1^{T\neq 0}(h,S,T) = \frac{T^4}{2\pi^2} \sum_i \bar{g}_i\, J_{F,B}\left(\frac{m_i^2(h,S)}{T^2}\right), \tag{3.13}$$

and to include only the dominant contributions from the thermal bosonic and fermionic functions J_B (1.40) and J_F (1.45),

$$\begin{aligned} J_F\left(\frac{m_i^2(h,S)}{T^2}\right) &\simeq \frac{7\pi^4}{360} - \frac{\pi^2}{24}\frac{m_i^2(h,S)}{T^2}, \\ J_B\left(\frac{m_i^2(h,S)}{T^2}\right) &\simeq -\frac{\pi^4}{45} + \frac{\pi^2}{12}\frac{m_i^2(h,S)}{T^2} - \frac{\pi}{6}\left(\frac{m_i^2(h,S)}{T^2}\right)^{\frac{3}{2}}, \end{aligned} \tag{3.14}$$

in the calculation of the effective potential. By inserting the above expressions for J_B and J_F in (3.15), we determine the finite-temperature one-loop contribution in the singlet extension as

$$
\begin{aligned}
V_1^{T\neq 0}(h,S,T) = & g_t\left[-\frac{7\pi^2}{720}T^4+\frac{1}{48}T^2 m_t^2(h)\right] \\
& + \sum_{i=W,Z,\gamma,\chi,h,S}\bar{g}_i\left[-\frac{\pi^2}{90}T^4+\frac{1}{24}T^2 m_i^2(h,S)-\frac{1}{12\pi}T\left(m_i^2(h,S)\right)^{\frac{3}{2}}\right].
\end{aligned}
\tag{3.15}
$$

Note that the thermal bosonic function J_B, in contrary to J_F, includes a contribution $\propto \left(m_i^2(h,S)\right)^{3/2}$ being crucial for the investigation of the phase transition. As this term generates a cubic contribution of the singlet field S in the effective potential, it leads to a thermally induced barrier and hence provides the necessary ingredient for a first-order phase transition.
However, the emergence of the monomial term of order $\frac{3}{2}$ reveals the breakdown of perturbation theory in the high-temperature expansion due to IR divergences. As explained in (Sec. 1.2.3), we consequently have to include the contribution of the ring diagrams in the calculation of the one-loop effective potential.

3.2.3. Ring-Diagram Contributions to the Effective Potential

Due to the ring-diagram contribution to the effective potential (cf. (1.50))

$$
V_{ring}(h,S,T) = -\frac{1}{12\pi}T\sum_{i=W_{l,t},Z_{l,t},\gamma_{l,t},\chi,h,S}\bar{g}_i\left[\left(M_i^2(h,S,T)\right)^{3/2}-\left(m_i^2(h,S)\right)^{3/2}\right], \tag{3.16}
$$

the field-dependent masses $m_i^2(h,S)$ of the finite-temperature one-loop contribution are replaced by the *thermal* field-dependent masses, defined in (1.49) as

$$
M_i^2(h,S,T) \equiv m_i^2(h,S) + \Pi_i(h,S,T), \tag{3.17}
$$

wherein $\Pi_i(h,S,T)$ denotes the self-energy of the bosonic field i in the IR limit. In the gauge-boson sector, only the longitudinal polarizations are thermally shifted as the transversal polarizations of the self-energies in the IR limit are zero, $\Pi_t(h,S,T) \simeq 0$. The longitudinal and transversal components of the modified gauge-boson degrees of freedom for the gauge bosons are given by

$$
\begin{aligned}
\bar{g}_{W_l} &= 2, \quad \bar{g}_{W_t} = 4 \\
\bar{g}_{Z_l} &= 1, \quad \bar{g}_{Z_t} = 2, \\
\bar{g}_{\gamma_l} &= 1, \quad \bar{g}_{\gamma_t} = 2.
\end{aligned}
\tag{3.18}
$$

Note that the only contribution of the massless photon to the ring-contributions emerges due to the non-vanishing longitudinal polarization of the self-energy Π_{γ_l}.

The computation of the self-energies in the singlet extension of the Standard Model, which is explained in detail in Sec. A.1, yields the following results

$$\begin{aligned}
\Pi_{W_l} &= \frac{11}{6} g^2\, T^2, \\
\Pi_{Z_l} &= -\frac{g^2}{4}\, h^2 + \frac{11}{6} g'^2\, T^2 = -m_W^2\,(h) + \frac{11}{6} g'^2\, T^2, \\
\Pi_{\gamma_l} &= \frac{g^2}{4}\, h^2 + \frac{11}{6} g^2\, T^2 = m_W^2\,(h) + \frac{11}{6} g^2\, T^2,
\end{aligned} \tag{3.19}$$

for the longitudinal components of the gauge bosons (cf. (A.10), (A.11)) and

$$\begin{aligned}
\Pi_{SS} &= \left(\frac{\lambda_S}{4} + \frac{\lambda_m}{6}\right) T^2, \\
\Pi_{hh} = \Pi_{\chi} &= \left(\frac{\lambda_h}{2} + \frac{\lambda_m}{24} + \frac{3g^2 + g'^2}{16} + \frac{y_t^2}{4}\right) T^2, \\
\Pi_{hS} &= \Pi_{Sh} \simeq 0,
\end{aligned} \tag{3.20}$$

for the Higgs and singlet contributions (cf. (A.6)).Thereof, the physical Higgs and Singlet thermal masses, $M_h^2(h,S,T)$ and $M_S^2(h,S,T)$ are computed as eigenvalues of thermal mass matrix

$$\mathcal{M}^2_{thermal}(h,S,T) = \begin{pmatrix} M_{hh}^2(h,S,T) & M_{hS}^2(h,S,T) \\ M_{Sh}^2(h,S,T) & M_{SS}^2(h,S,T) \end{pmatrix}, \tag{3.21}$$

where the single elements are given by

$$\begin{aligned}
M_{SS}^2\,(h,S,T) &= m_{SS}^2\,(h,S) + \,\Pi_{SS}\,(T)\,, \\
M_{hh}^2(h,S,T) &= m_{hh}^2(h,S) + \,\Pi_{hh}(T)\,, \\
M_{Sh}^2(h,S,T) &= M_{hS}^2\,(h,S,T) \simeq m_{hS}^2\,(h,S)\,.
\end{aligned} \tag{3.22}$$

with $m_{SS}^2\,(h,S)$, $m_{hh}^2(h,S)$ and $m_{hS}^2\,(h,S)$ given in (3.11). After diagonalization of $\mathcal{M}^2_{thermal}(h,S,T)$, the thermal Higgs and singlet eigenmasses emerge, in analogy to the non-thermal case, as

$$M_{h,S}^2\,(h,S,T) = \frac{1}{2}\left\{M_{hh}^2(h,S) + M_{SS}^2\,(h,S) \mp \sqrt{\left[M_{hh}^2(h,S) - M_{SS}^2\,(h,S)\right]^2 + 4\,m_{hS}^2\,(h,S)}\right\} \;\cdot \tag{3.23}$$

Finally, by summarizing the one-loop corrections to the tree-level potential (3.5) at zero- and finite temperature, (3.7) and (3.15), respectively, and including the ring-diagram contributions of (3.16), the full one-loop effective potential at finite temperature in the singlet extension of the Standard Model reads

$$\begin{aligned}
V_{eff}(h,S,T) &= V_0(h,S) + V_1^{T=0}(h,S) + V_1^{T\neq 0}(h,S,T) + V_{ring}(h,S,T) \\
&= -\frac{\mu_h^2}{2}h^2 + \frac{\lambda_h}{4}h^4 - \frac{\mu_S^2}{2}S^2 + \frac{\lambda_S}{4}S^4 + \frac{\lambda_m}{4}h^2S^2 \\
&\quad + \frac{1}{64\pi^2}\sum_{i=t,W,Z,\gamma,\chi,h,S}\bar{g}_i\, m_i^4(h,S)\left(\ln\left[\frac{m_i^2(h,S)}{\mu^2}\right] - C_i\right) \\
&\quad + g_t\left[-\frac{7\pi^2}{720}T^4 + \frac{1}{48}T^2 m_t^2(h)\right] \\
&\quad + \sum_{i=W,Z,\gamma,\chi,h,S}\bar{g}_i\left[-\frac{\pi^2}{90}T^4 + \frac{1}{24}T^2 m_i^2(h,S)\right] \\
&\quad - \frac{1}{12\pi}T\sum_{i=W_{l,t},Z_{l,t},\gamma_{l,t},\chi,h,S}\bar{g}_i\left(M_i^2(h,S)\right)^{\frac{3}{2}}.
\end{aligned} \tag{3.24}$$

In the following, we will neglect the constant terms $\propto T^4$ in the effective potential. As these terms are *field-independent*, they are neither physically important for the phase-transition scenario (cf. Sec. 3.3.2) nor for the spectrum of gravitational waves (cf. Sec. 3.5.1).

3.2.4. High-Temperature Approximation of the Effective Potential

Our intention is to investigate whether the first-order phase transition in the singlet model provides the possibility for detectable gravitational waves at temperatures between the electroweak and the GUT scale.

Within this temperature range, the dominant corrections to the tree-level potential will arise from the temperature-dependent one-loop and ring contributions. To derive a high-temperature approximation of the effective potential, zero-temperature Coleman-Weinberg corrections can be neglected. Additionally, the restriction to the high-temperature scale leads to a natural decoupling of the singlet field S from the low-energy sector of the model. This allows in particular to neglect the contributions of the Higgs field h to the effective potential, including the dependency of field-dependent (thermal) masses on h. Consequently, the field-dependent masses of the Standard Model particles vanish, while the Higgs and singlet eigenmasses are reduced to a pure dependency on S.

Following this considerations, the full one-loop effective potential of (3.24) reads in the high-temperature approximation

$$\begin{aligned}
V_{eff}(S,T) &\simeq V_0(S) + V_1^{T\neq 0}(S,T) + V_{ring}(S,T) \\
&\simeq -\frac{\mu_S^2}{2}S^2 + \frac{\lambda_S}{4}S^4 \\
&\quad + \sum_{i=\chi,h,S}\bar{g}_i\left[\frac{1}{24}T^2 m_i^2(S) - \frac{1}{12\pi}T\left(M_i^2(S,T)\right)^{\frac{3}{2}}\right].
\end{aligned} \tag{3.25}$$

Therein, the field-dependent Higgs and singlet eigenmasses, computed in (3.12), reduce to

$$m_h^2(S) = m_\chi^2(S) \simeq -\mu_h^2 + \frac{\lambda_m}{2} S^2, \tag{3.26}$$

$$m_S^2(S) \simeq -\mu_S^2 + 3\lambda_S S^2, \tag{3.27}$$

and lead to the thermal eigenmasses (cf. (3.23))

$$M_h^2(S,T) = M_\chi^2(S,T) \simeq -\mu_h^2 + \frac{\lambda_m}{2} S^2 + c_h T^2, \tag{3.28}$$

$$M_S^2(S,T) \simeq -\mu_S^2 + 3\lambda_S S^2 + c_S T^2. \tag{3.29}$$

with

$$c_h \equiv \left(\frac{\lambda_h}{2} + \frac{\lambda_m}{24}\right), \tag{3.30}$$

$$c_S \equiv \left(\frac{\lambda_S}{4} + \frac{\lambda_m}{6}\right). \tag{3.31}$$

Note in particular that the neglection of the Higgs field h diagonalizes the mass matrices (3.10) and (3.21) so that the Higgs and singlet (thermal) eigenmasses can be directly read off from the diagonal elements, for instance $m_h^2(S) \equiv m_{hh}^2(S)$ and $M_h^2(S,T) \equiv M_{hh}^2(S)$. Inserting $\overline{g}_\chi = 3$, $\overline{g}_h = 1$ and $\overline{g}_S = 1$ in (3.25) finally yields for the effective potential in the high-temperature approximation

$$\begin{aligned} V_{eff}(S,T) = \frac{1}{2}\left(-\mu_S^2 + c_S T^2\right) S^2 + \frac{\lambda_S}{4} S^4 - \frac{1}{24}\left(4\mu_h^2 + \mu_S^2\right) T^2 \\ - \frac{1}{12\pi} T \left[4\left(M_h^2(S,T)\right)^{\frac{3}{2}} + \left(M_S^2(S,T)\right)^{\frac{3}{2}}\right] \end{aligned} \tag{3.32}$$

with $M_{h,S}^2(S,T)$ given in (3.28) and (3.29). This expression for the effective potential consists our basic equation for the further investigation of the phase transition.

3.3. Investigation of the Phase Transition

3.3.1. Phase-Transition Scenario

We will consider the following phase-transition scenario in the singlet extension of the Standard Model: Due to the symmetry restoration at high temperatures, the symmetric phase $S(T) = 0$ initially constitutes the absolute stable minimum of the effective potential. When the temperature is lowered, a local minimum, separated from the symmetric phase at the origin by a barrier in the effective potential, occurs at $S(T) \neq 0$. As long as the temperature is larger than the critical temperature T_C, where both minima become degenerate, the singlet is stable. Thereafter, thermal fluctuations can induce the spontaneous breaking of the $\mathbb{Z}_2$-symmetry and the phase transition from the false to the true vacuum proceeds, whereby the singlet acquires a (non-vanishing) VEV. The emergence of the barrier in the effective potential thereby restricts the phase transition to be of first order.

3.3.2. Conditions for a First-Order Phase Transition

A first-order phase transition necessarily requires two conditions to be fulfilled.[3] These can be used to determine the critical temperature T_C of the phase transition and the corresponding singlet VEV $\langle S(T_C)\rangle \equiv \pm S_C$ (with $S_C > 0$). At first, the emergence of a barrier between the true and the false vacuum state requires the development of a second minimum apart from the origin [178],

$$\left.\frac{\partial V_{eff}(S,T)}{\partial S}\right|_{S\neq 0} = 0 \quad \text{with} \quad \left.\frac{\partial^2 V_{eff}(S,T)}{\partial S^2}\right|_{S\neq 0} > 0, \tag{3.33}$$

whereof the temperature-dependent singlet VEV $\langle S(T)\rangle \neq 0$ can be derived. Secondly, the definition of T_C as the temperature where both minima become degenerate leads to the condition [178]

$$\Delta V_{eff}(T)\Big|_{T=T_C} = 0 \tag{3.34}$$

with (cf. (2.5))

$$\Delta V_{eff}(T) \equiv V_{eff}(S=0,T) - V_{eff}(S=\langle S(T)\rangle, T)\,. \tag{3.35}$$

From 3.34 the critical temperature T_C of the phase transition and subsequently the corresponding singlet VEV S_C can be computed. The ratio between S_C and T_C defines in turn the strength of the phase transition. For a *strongly* first-order phase transition it has to lie in the range [61]

$$\frac{S_C}{T_C} \gtrsim 1. \tag{3.36}$$

The effective potential of (3.25) only allows to determine the critical temperature and the singlet VEV numerically due to the emergence of the terms of order $\frac{3}{2}$ containing the thermal masses. However, it is possible to derive an approximate analytical solution for these quantities which will reveal their functional dependence on the model parameters.

Analytical Approximation of the Critical Temperature and the Singlet VEV

We will consider two approximations of the effective potential in (3.25) which allow to determine the critical temperature and the singlet VEV analytically. The first approximation will consist in the neglection of the thermal masses of the Higgs and the singlet, whereas the second approximation will base on a constraint imposed on the Higgs thermal mass by still neglecting the singlet contribution.

---

[3] Reviews on finite-temperature phase transitions, where the characteristics of first- and second-order phase transitions are discussed, can be found for instance in [175, 177, 178, 180, 133].

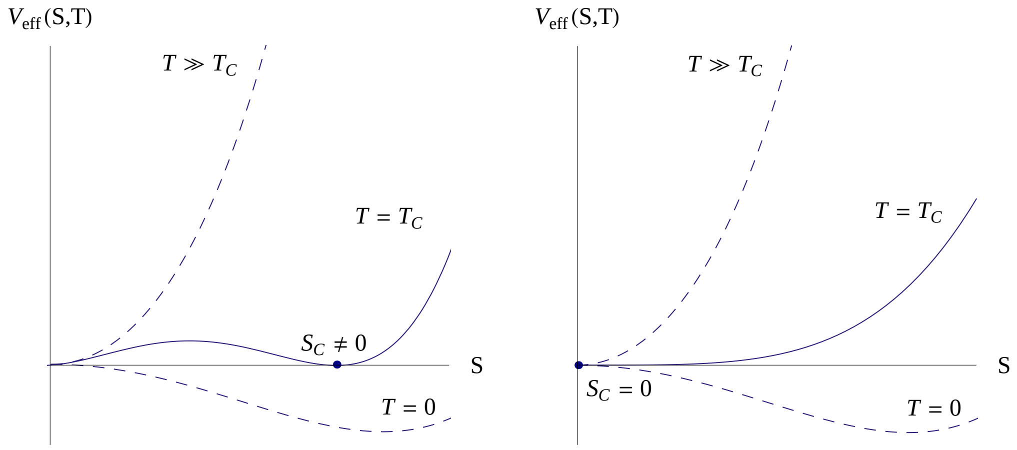

(a) *First-order phase transition.* **(b)** *Second-order phase transition.*

Figure 3.1: *Comparison of first- and second-order phase transitions in the singlet extension of the Standard Model.* The barrier between the true and the false vacuum in the effective potential, which is generated in the singlet model by a thermally induced cubic, distinguishes first-order and second-order phase transitions. (Note that we have only depicted the effective potential for $S > 0$.)

Neglection of the Higgs and Singlet Thermal Masses. If we neglect the thermal masses of the Higgs and the singlet,

$$M_h^2(S,T) = 0, \; M_S^2(S,T) = 0, \tag{3.37}$$

the effective potential of (3.32) becomes

$$V_{eff}(S,T) = \frac{1}{2}\left(-\mu_S^2 + c_S T^2\right) S^2 + \frac{\lambda_S}{4} S^4 - \frac{1}{24}\left(4\mu_h^2 + \mu_S^2\right) T^2. \tag{3.38}$$

with c_S defined in (3.31). In this approximation the thermally induced cubic term $\propto S^3$, which is contained in the thermal mass contributions and generates the barrier between the true and the false vacuum state, vanishes. Therefore, the phase transition is not of first-order any more, but reduces to a second-order phase transition [175]. As depicted in Fig. 3.1, the temperature-dependent singlet VEV, derived as minimum of the effective potential (3.38), yielding

$$\langle S(T) \rangle = \pm\sqrt{\frac{\mu_S^2 - c_S T^2}{\lambda_S}}, \tag{3.39}$$

collapses with the symmetric phase to an inflection point in the origin at the critical temperature,

$$\langle S(T_C) \rangle = 0, \tag{3.40}$$

implying $S_C = 0$. At $T = T_C$ the quadratic term $\propto S^2$ in the effective potential of (3.38) thus changes in sign, so that the critical temperature can be determined as[4]

$$\left.\frac{\partial^2 V_{eff}(S,T)}{\partial S^2}\right|_{S=0,T=T_C} = 0 \quad \Rightarrow T_C = \sqrt{\frac{\mu_S^2}{c_S}}. \tag{3.41}$$

The strength of the second-order phase transition (at the critical temperature) therefore vanishes, $\frac{S_C}{T_C} = 0$.
The considered case of the second-order phase transition reveals the relevance of the thermally induced barrier for the phase-transition scenario. In the second approximation, we will therefore include the Higgs thermal mass to generate a barrier between the degenerated minima, but still neglect the singlet thermal mass to preserve the possibility for deriving an analytical solution for the critical temperature and the singlet VEV. (The physical motivation on which these assumptions are based will be explained in Sec. 3.3.3.)

Neglection of the Singlet Thermal Mass. If we assume the thermal masses of the Higgs and the singlet to take the form

$$M_h^2(S,T_C) = \frac{\lambda_m}{2} S^2, \;\; M_S^2(S,T_C) = 0 \tag{3.42}$$

at the critical temperature, a pure cubic singlet contribution $\propto S^3$, providing the barrier for the first-order phase transition, arises in the effective potential (cf. (3.25))

$$\begin{aligned} V_{eff}(S,T_C) = &\frac{1}{2}\left(-\mu_S^2 + c_S T_C^2\right) S^2 - \frac{1}{3\pi}\left(\frac{\lambda_m}{2}\right)^{\frac{3}{2}} T_C S^3 + \frac{\lambda_S}{4} S^4 \\ &- \frac{1}{24}\left(4\mu_h^2 + \mu_S^2\right) T_C^2. \end{aligned} \tag{3.43}$$

In analogy to the “Mexican hat” form of the Higgs potential [100], the above equation can be rewritten by the ansatz

$$\begin{aligned} V_{eff}(S,T_C) &= \frac{\lambda_S}{4}(S - S_C)^2 S^2 \\ &= \frac{\lambda_S}{4} S_C^2 S^2 - \frac{\lambda_S}{2} S_C S^3 + \frac{\lambda_S}{4} S^4 \end{aligned} \tag{3.44}$$

(where the physically irrelevant last term in (3.43) could be included as constant in the ansatz, but has been ignored here). The comparison of the terms $\propto S^2$ and $\propto S^3$ in (3.43) and (3.44) yields the singlet VEV, the critical temperature and the strength of the phase

---

[4] Note that the condition $\Delta V_{eff}(T)\big|_{T=T_C} = 0$ with $\Delta V_{eff}(T)$ given in (3.34), generally determines the critical temperature regardless of the order of the phase transition and hence yields the same result as obtained by (3.41).

transition,

$$S_C = \pm\sqrt{\frac{2\left(-\mu_S^2 + c_S T_C^2\right)}{\lambda_S}} = \sqrt{\frac{2}{36\pi^2 \frac{\lambda_S}{\lambda_m^3} c_s - 1} \frac{\mu_S^2}{\lambda_S}}, \tag{3.45}$$

$$T_C = \sqrt{\frac{\mu_S^2}{c_S - \frac{1}{36\pi^2}\frac{\lambda_m^3}{\lambda_S}}}, \tag{3.46}$$

$$\frac{S_C}{T_C} = \frac{\sqrt{2}}{6\pi}\frac{\lambda_m^{\frac{3}{2}}}{\lambda_S} \tag{3.47}$$

with c_S given in (3.31). Thereby, the additional term $-\frac{1}{36\pi^2}\frac{\lambda_m^2}{\lambda_S}$ in the expression for the critical temperature corresponds to the correction to the effective potential arising from the thermal Higgs mass (the cubic singlet term). Although it reduces the critical temperature only marginally (due to the suppression by the factor $\frac{1}{36\pi^2}$), it is essential for generating a singlet VEV $S_C \neq 0$.
Note that dimensional reasons require the singlet VEV S_C and the critical temperature T_C to be proportional to the dimensionful parameter μ_S^2. The choice of μ_S^2 will therefore set the temperature scale for the phase transition. Consequently, the strength of the phase transition, defined as ratio of S_C and T_C, is independent of the temperature scale, but only depend on the (small) couplings (cf. (3.47)). This is a general feature of first-order phase transitions generated by thermally induced barriers [82].

Based on this considerations, we will determine numerically the singlet VEV, the critical temperature and the phase transition strength for the full effective potential of (3.32),

$$\begin{aligned} V_{eff}(S,T) \simeq{}& \frac{1}{2}\left(-\mu_S^2 + c_S T^2\right)S^2 + \frac{\lambda_S}{4}S^4 - \frac{1}{24}\left(4\mu_h^2 + \mu_S^2\right)T^2 \\ & - \frac{1}{12\pi}T\left[4\left(M_h^2(S,T)\right)^{\frac{3}{2}} + \left(M_S^2(S,T)\right)^{\frac{3}{2}}\right] \end{aligned} \tag{3.48}$$

including both the Higgs and singlet thermal masses $M_h^2(S,T)$ and $M_S^2(S,T)$ of (3.28) and (3.29), respectively. In the numerical analysis, we have to regard the constraints on the model parameters to obtain a physically viable phase-transition scenario. We will discuss these parameter constraints in the following section.

3.3.3. Parameter Constraints

The choice of model parameters for the numerical analysis is restricted to those regions in parameter space which preserve the physical relevance of the model. These regions are determined by the following parameter constraints:

Vacuum Stability. The zero-temperature tree-level potential of (3.5),

$$V_0(h,S) = -\frac{\mu_h^2}{2}h^2 + \frac{\lambda_h}{4}h^4 - \frac{\mu_S^2}{2}S^2 + \frac{\lambda_S}{4}S^4 + \frac{\lambda_m}{4}h^2S^2 \tag{3.49}$$

with $\mu^2_{h,S} > 0$ and $\lambda_{h,S,m} > 0$, has to be bounded from below to guarantee the vacuum stability of the theory. Thus, the potential is required to reach infinity when the Higgs and singlet field become infinite in any direction [12], i.e.,

$$V_0(h,S) \to \infty \text{ for } \begin{cases} h \to \infty & \text{or} \quad S \to \infty \\ h \to \infty & \text{and} \quad S \to \infty \end{cases}. \tag{3.50}$$

Since the large-field behavior of the tree-level potential is dominated by the quartic contributions in terms of the fields h and S, vacuum stability is ensured if the constraint

$$\lambda_h \lambda_S > \lambda_m^2 \tag{3.51}$$

is fulfilled.

Higgs mass and VEV. The low-energy features of the singlet model are dictated by the Standard Model phenomenology. In particular, the Standard Model Higgs potential has to be regained at temperatures of the electroweak scale where $T \ll \mu_S^2$. Furthermore, the singlet model has to reproduce the experimentally determined (zero-temperature) VEV and mass of the Higgs boson correctly.

At zero temperature the singlet VEV yields approximately (cf. (3.39)) $\langle S(0)\rangle \equiv S_0 = \sqrt{\mu_S^2/\lambda_S}$. By inserting this expression in the tree-level potential $V_0(\Phi, S)$ given in (3.3), a redefined Higgs potential

$$\overline{V}_H(\Phi) = V_0(\Phi, \langle S\rangle) = -\overline{\mu}_h^2 \left(\Phi^\dagger\Phi\right) + \lambda_h \left(\Phi^\dagger\Phi\right)^2 \tag{3.52}$$

can be derived. Therein, the contributions of the singlet VEV to the tree-level potential have been absorbed by introducing the parameter

$$\overline{\mu}_h^2 \equiv \mu_h^2 - \frac{\lambda_m}{2}\frac{\mu_S^2}{\lambda_S}. \tag{3.53}$$

The Higgs VEV $v = \sqrt{\overline{\mu}_h^2/2\lambda_h}$ and the squared Higgs mass $m_h^2 = 4\overline{\mu}_h^2 = 8\lambda_h v^2$ emerge from the vanishing first derivative and the second derivative of the redefined Higgs potential with respect to the Higgs field, respectively. By setting $v = 250\,\mathrm{GeV}$ and $m_h = 125\,\mathrm{GeV}$,[5] the last equation transforms into the constraint

$$\lambda_h = \frac{m_h^2}{8v^2} = \frac{1}{32} \simeq 0.03. \tag{3.54}$$

Since this constraint includes the ratio between the Higgs VEV and the respective mass, it determines the parameter λ_h independently of the temperature scale. The Higgs mass m_h and hence the Higgs VEV v, in contrary, are negligible at temperatures significantly above the electroweak scale, requiring the redefined parameter $\overline{\mu}_h^2$ to vanish as well. Inserting $\overline{\mu}_h^2 \simeq 0$ in (3.53) then yields as a second constraint

$$\mu_h^2 \simeq \frac{\mu_S^2}{2}\frac{\lambda_m}{\lambda_S}. \tag{3.55}$$

---

[5] This choice of the Higgs mass is in accordance with the current experimental results [57, 1, 32].

Parameter	Constraint	Free
λ_h	$\lambda_h = \frac{m_h^2}{8v^2} = \frac{1}{32} \simeq 0.03$ (3.54)	×
λ_S	$\lambda_S = \frac{\lambda_m^2}{6\lambda_h-\lambda_m}$ (3.57)	×
λ_m	/	√
μ_h^2	$\mu_h^2 = \frac{\mu_S^2}{2}\frac{\lambda_m}{\lambda_S}$ (3.55)	×
μ_S^2	/	√

Table 3.1: *Free and constrained parameters in the singlet extension of the Standard Model.* Since the parameters μ_h^2, λ_h and λ_S are restricted by either phenomenological or model constraints, the remaining free parameters of the singlet model are μ_S^2 and λ_m. The dimensionful parameter μ_S^2 will determine the symmetry breaking scale, while the choice of λ_m will be the crucial ingredient for determining the strength of the phase transition.

Thermal Higgs mass. The above equation relates the parameter μ_h^2 to the symmetry breaking scale set by μ_S^2. As μ_S^2 likewise determines the scale of the critical temperature T_C, we require these contributions in the Higgs thermal mass to cancel each other at the critical temperature, $\mu_h^2 = c_h\, T_C^2$. This generates a strong cubic term $\propto S^3$ in the effective potential by the reduction of the Higgs thermal mass to a pure singlet contribution (cf. (3.28)),

$$M_h^2(S, T_C) = \frac{\lambda_m}{2} S^2. \tag{3.56}$$

After inserting μ_h^2, given in (3.55), and T_C, approximated by (3.41), in the condition $\mu_h^2 = c_h\, T_C^2$, we solve the resulting equation for λ_S and obtain the constraint

$$\lambda_S = \frac{\lambda_m^2}{6\lambda_h - \lambda_m}. \tag{3.57}$$

Free and Constrained Parameters in the Singlet Extension of the Standard Model

The parameter constraints for the singlet extension of the Standard Model are summarized Tab. 3.1. As the two parameters μ_h^2 and λ_h are constrained by the Higgs phenomenology and the model constraint on the thermal Higgs mass restricts the parameter λ_S, two of the five model parameters, namely μ_S^2 and λ_m, remain free to choose. (As we will see in Sec. 3.4.1, the upper bound imposed on λ_m by the requirement of vacuum stability will be implicitly fulfilled.) The choice of the dimensionful parameter μ_S^2 will determine the symmetry breaking scale and hence the order of magnitude of the critical temperature T_C as well as the singlet VEV S_C. The strength of the phase transition $\frac{S_C}{T_C}$, which is consequently dimensionless, cannot depend on the parameter μ_S^2, but only on the couplings. Therefore, the choice of the free parameter λ_m will be dominantly determine the strength of the phase transition.
As the determination of the critical temperature, the singlet VEV and the phase transition strength for the full effective potential of (3.48) is not achievable by analytical means, we

will next perform a numerical analysis by taking into account the derived parameter constraints.

3.4. Numerical Analysis of the Phase Transition

Our intention for the numerical analysis of the phase transition is to investigate whether the parameter constraints allow for a choice of parameters appropriate to provide a strongly first-order phase transition in the singlet extension of the Standard Model. Since stronger phase transitions in general generate GW spectra with higher peak amplitudes $h_0^2\Omega_{GW}$, this requirement will be crucial with regard to the detectability of the gravitational radiation.

3.4.1. Determination of the Parameter Space

Which regions of the parameter space are allowed to choose for the parameters in the singlet extension of Standard Model? The space of parameters is confined by the parameter constraints guaranteeing a physical viable phase-transition scenario. These determine the parameters λ_h, λ_S and μ_S^2, whereas the parameters λ_m and μ_S^2 are not constrained. In the following, we will discuss the allowed range for the choice of λ_m and will set the scale for the symmetry breaking to occur by choosing μ_S^2.

Range of λ_m. In general, the renormalizability of the theory restricts the couplings λ_h, λ_S and λ_m to values < 1. While the parameter λ_h is dictated by the low-energy Higgs phenomenology, $\lambda_h \simeq 0.03$ (cf. (3.54)), the parameter λ_S will be determined by the constraint (3.57) in dependency on λ_m. By requiring $\lambda_S < 1$, we can thus derive an upper bound on the parameter λ_m,

$$\lambda_m < 0.16 \tag{3.58}$$

(where we consider only the case $\lambda_m > 0$). Note that this upper bound additionally ensures the condition for vacuum stability in (3.51) to be implicitly fulfilled. Besides, it guarantees $\lambda_S > 0$ since $\lambda_m < 6\lambda_h$ (cf. (3.57)).

Since the couplings λ_h and λ_S are confined by the parameter constraints, the choice of λ_m will determine the strength of the phase transition. (As discussed before, the dimensionless phase transition strength cannot depend on the dimensionful free parameter μ_S^2.) According to (3.36), a strongly first-order phase transition requires a strength of at least $\frac{s_C}{T_C} \gtrsim 1$. For very large values of $\frac{s_C}{T_C}$ the phase transition is however expected to never be completed [81]. Therefore, we require the strength of the phase transition to be $\frac{s_C}{T_C} \lesssim 4$. By inserting the constraint (3.57) on λ_S in the approximate analytical expression (3.45) for the strength of the phase transition, the demand $\frac{s_C}{T_C} \lesssim 4$ transforms into a lower bound on λ_m,

$$\lambda_m \gtrsim 1.24 \cdot 10^{-5}. \tag{3.59}$$

For the numerical analysis, we will thus vary λ_m in the range $0.16 > \lambda_m \gtrsim 1.24 \cdot 10^{-5}$.

Choice of μ_S^2 In the singlet extension of the Standard Model μ_S^2 is the only parameter which is neither confined by a parameter constraints nor is restricted to a certain range of parameter space. This allows in particular a free choice of the symmetry breaking scale set by μ_S^2. Since our intention is to investigate the phase-transition at a temperature scale between the electroweak and the GUT scale, $T_{EW} < T_* < T_{GUT}$ with $T_{EW} \simeq 10^2$ GeV and $T_{GUT} \simeq 10^{16}$ GeV , we will choose

$$\mu_S^2 = 10^{10}\,(\text{GeV})^2 \tag{3.60}$$

for the further analysis, leading to values of the critical temperature in the range $T_C \simeq 10^5 \ldots 10^7$ GeV. We will discuss the results of the numerical analysis in detail in the following section.

3.4.2. Results of the Numerical Analysis

A selection of the results from the numerical analysis is given in Tab. 3.2. We compare the numerical solutions to the corresponding solutions obtained from the approximately analytical determined expressions (3.45)-(3.47) for critical temperature, the singlet VEV and the strength of the phase transition.

The numerical as well as the approximate analytical analysis yield results for the critical temperature T_C of the phase transition which only differ marginally. However, the numerical and analytical solutions for singlet VEV S_C deviate the stronger, the bigger the value of λ_m. This deviation originates from the contribution of the thermal Higgs mass at the critical temperature, $M_h^2(S, T_C) = \frac{\lambda_m}{2} S^2$ (cf. (3.56)), which has been included for the numerical determination of S_C, but was neglected for deriving an approximate analytical solution. For small values of λ_m the contribution of the thermal Higgs mass is negligible in comparison to the one of the singlet thermal mass. Thus, the solution for S_C derived numerically from the full effective potential is well approximated by the analytical solution of (3.45) for small values of λ_m.

Since the strength of the phase transition is defined as ratio of S_C and T_C, it displays the same behavior as the singlet VEV. This is depicted in Fig. 3.2. For values of λ_m close to the upper bound, the numerical results differ from those derived from the approximate analytical solution, while the functional dependence of the strength of the phase transition is well approximated by the analytical solution (3.47),

$$\frac{S_C}{T_C} = \frac{\sqrt{2}}{6\pi}\frac{\lambda_m^{\frac{3}{2}}}{\lambda_S}, \tag{3.61}$$

for small values of λ_m. If $\lambda_m \ll \lambda_h$, the parameter constraint on λ_S, given in (3.57), reduces to $\lambda_S \simeq \frac{\lambda_m^2}{6\lambda_h}$. Hence, the dominant functional dependence of the phase transition strength on the model parameters arises as $\frac{S_C}{T_C} \propto \frac{1}{\sqrt{\lambda_m}}$.

	Numerical solution			**Appr. analytical solution**		
λ_m	S_C **[GeV]**	T_C **[GeV]**	$\frac{S_C}{T_C}$	S_C **[GeV]**	T_C **[GeV]**	$\frac{S_C}{T_C}$
$2 \cdot 10^{-5}$	$1.73 \cdot 10^{8}$	$5.49 \cdot 10^{7}$	3.15	$1.72 \cdot 10^{8}$	$5.49 \cdot 10^{7}$	3.15
$6 \cdot 10^{-5}$	$5.75 \cdot 10^{7}$	$3.17 \cdot 10^{7}$	1.82	$5.74 \cdot 10^{7}$	$3.17 \cdot 10^{7}$	1.82
$1 \cdot 10^{-4}$	$3.45 \cdot 10^{7}$	$2.45 \cdot 10^{7}$	1.41	$3.44 \cdot 10^{7}$	$2.45 \cdot 10^{7}$	1.41
$2 \cdot 10^{-4}$	$1.72 \cdot 10^{7}$	$1.73 \cdot 10^{7}$	0.99	$1.72 \cdot 10^{7}$	$1.73 \cdot 10^{7}$	0.99
$6 \cdot 10^{-4}$	$5.72 \cdot 10^{6}$	$9.99 \cdot 10^{6}$	0.57	$5.71 \cdot 10^{6}$	$9.99 \cdot 10^{6}$	0.57
0.001	$3.42 \cdot 10^{6}$	$7.73 \cdot 10^{6}$	0.44	$3.41 \cdot 10^{6}$	$7.73 \cdot 10^{6}$	0.44
0.01	$3.27 \cdot 10^{5}$	$2.36 \cdot 10^{6}$	0.14	$3.13 \cdot 10^{5}$	$2.36 \cdot 10^{6}$	0.13
0.1	$2.76 \cdot 10^{4}$	$4.78 \cdot 10^{5}$	0.06	$9.76 \cdot 10^{3}$	$4.70 \cdot 10^{5}$	0.02

Table 3.2: *Results of the numerical analysis for the first-order phase transition in the singlet extension of the Standard Model in comparison with the results of the approximate analytical expressions.* For the numerical analysis we have chosen the free parameter μ_S^2 to be $\mu_S^2 = 10^{10}\,(\mathrm{GeV})^2$ yielding critical temperatures of the order $10^5 \ldots 10^7$ GeV, whereas the parameter λ_m has been varied in the allowed range leading to different values of the phase transition strength. The highlighted values compose the lower bound for a strongly first-order phase transition.

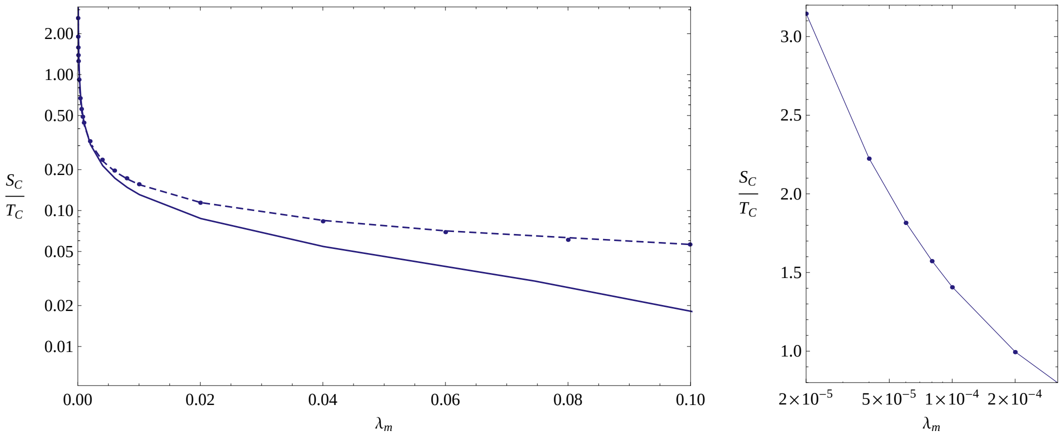

(a) *Functional dependency of the phase transition strength $\frac{S_C}{T_C}$ on the parameter λ_m varied in the allowed range.* While the dashed line constitutes a trendline for values of the phase transition strength (indicated by dots) which have been numerically determined from the full effective potential in (3.48), the solid line displays the functional behavior of the approximate analytically derived expression (3.47). The deviation for bigger values of λ_m results from the neglection of the thermal Higgs mass in the approximate solution.

(b) *Functional dependency of the phase transition strength $\frac{S_C}{T_C}$ on the parameter λ_m in the range relevant for generating a strong first-order phase transition.* For small λ_m the numerical results (dots) are well approximated by the analytical solution for $\frac{S_C}{T_C}$ (solid line).

Figure 3.2: *Functional dependency of the phase transition strength on the parameter λ_m.*

For investigating whether the phase transition in this model provides the possibility of de-

tectable gravitational waves, we require it to be strongly first-order. For achieving a phase transition strength, lying in the range $1 \lesssim \frac{S_C}{T_C} \lesssim 4$, the dependence of $\frac{S_C}{T_C}$ on λ_m forces us to choose very small values for the parameter λ_m. In detail, we obtain a phase transition strength $\frac{S_C}{T_C} = 0.99$ for $\lambda_m = 2 \cdot 10^{-4}$ (cf. Tab.3.2), while even a value of $\lambda_m = 2 \cdot 10^{-5}$ is necessary for a considerable strongly first-order phase transition with $\frac{S_C}{T_C} = 3.14$.
Hence, to generate a strongly first-order phase transition by a thermally induced barrier in the singlet-extension of the Standard Model, it is necessary to choose (unnaturally) small values of the coupling λ_m. In the following section, we will discuss if observable gravitational waves could be induced from this phase-transition scenario and could in consequence serve as cosmological probes for the physical conception of the singlet model.

3.5. Gravitational Waves as Cosmological Probes

The characteristic features of the GW spectrum are the peak frequency $\tilde{f}$ and the peak amplitude $h_o^2\tilde{\Omega}_{GW}$ (cf. Sec.4.5.3). If the peak frequency lies in the experimentally sensitive frequency range and the peak amplitude additionally is higher than the minimal achievable sensitivity of the GW detectors, the GW spectrum will be detectable.[6]
The peak frequency, given by (2.45) as

$$\tilde{f} = 3.79 \cdot 10^{-3}\,\mathrm{mHz} \left(\frac{\beta}{H_*}\right)\left(\frac{T_*}{100\,\mathrm{GeV}}\right)\left(\frac{g_*}{100}\right)^{\frac{1}{6}}, \tag{3.62}$$

is determined (apart from g_*) by the parameter $\frac{\beta}{H_*}$ and the tunneling temperature T_* where the phase transition proceeds. Thus, the chosen temperature scale has a direct impact on the position of the peak frequency. Since we are allowed to choose the parameter μ_S^2, setting the temperature scale, we will be able to adapt the position of the peak frequency by variation of μ_S^2 to the experimentally accessible frequency range.
In contrast, the dimensionless peak amplitude $h_o^2\tilde{\Omega}_{GW}$ (cf. (2.44)),

$$h_o^2\tilde{\Omega}_{GW} = 1.29 \cdot 10^{-6} \left(\frac{H_*}{\beta}\right)^2 \left(\frac{\alpha}{\alpha+1}\right)^2 \left(\frac{100}{g_*}\right)^{\frac{1}{3}}, \tag{3.63}$$

cannot depend on the tunneling temperature T_* itself, but only on the dimensionless parameters $\alpha(T_*)$ and $\beta(T_*)$. Hence, these will be determined by the choice of λ_m. As stronger phase transition in general lead to GW spectra with higher peak amplitudes, we will consider the parameter λ_m in the range $\lambda_m = 2 \cdot 10^{-4} \ldots 2 \cdot 10^{-5}$ allowing for a phase transition strength $\frac{S_C}{T_C} = 0.99 \ldots 3.15$. For detectable gravitational radiation, the parameters α and $\frac{\beta}{H_*}$ are required to adopt values of the order (cf. (2.46))

$$\alpha \sim \mathcal{O}(1)\,, \quad \frac{\beta}{H_*} \sim \mathcal{O}(100)\,. \tag{3.64}$$

---

[6] In Sec.C.2 the different GW experiments are briefly reviewed and the sensitivity curves $h_o^2\Omega_{GW}(f)$ are computed from the experimental data.

In the following we will determine the parameter α for different strengths of the phase transition. We will in particular derive an upper bound on α in the singlet extension of the Standard Model. Since the parameters α and $\frac{\beta}{H_*}$ are correlated by the dependency on the potential barrier, as discussed in Sec. 2.3, we will be able to estimate the order of magnitude of $\frac{\beta}{H_*}$ corresponding to the value of the upper bound on α. This will consequently allow to anticipate whether the first-order phase transition in the singlet model provides the possibility of detectable gravitational waves.

3.5.1. Numerical Determination of the Parameter α

At first, we will derive the formulae necessary for the determination of the parameter α in the singlet model. Afterwards, we will explicitly compute α for different model parameters.

Determination of the Parameter α

According to (2.1), the temperature-dependent parameter $\alpha(T)$ is defined as the ratio of the false-vacuum energy density $\epsilon(T)$ and the thermal energy density $e(T)$ of the symmetric phase,

$$\alpha \equiv \frac{\epsilon(T)}{e(T)}. \tag{3.65}$$

Thereby, the thermal energy density, $e(T) = \frac{\pi^2}{30} g_* T^4$, includes the total number of effective degrees of freedom g_* of the singlet model. As the extension of the Standard Model by an additional singlet S enlarges the number of degrees of freedom by $g_S = 1$ (cf. (3.8)), we obtain from (2.3) a value $g_* = g_{*SM} + g_S = 107.75$ for the singlet model.
The false-vacuum energy density (2.4),

$$\epsilon(T) \equiv \Delta V_{eff}(T) - T \frac{\partial \Delta V_{eff}(T)}{\partial T}, \tag{3.66}$$

for the singlet extension of the Standard Model is derived from the potential difference $\Delta V_{eff}(T)$ between the symmetric and the broken vacuum state. For the full effective potential of (3.48), including the Higgs and singlet thermal masses, (3.28) and (3.29), respectively, this potential difference reads

$$\begin{aligned}\Delta V_{eff}(T) &\equiv V_{eff}(S=0,T) - V_{eff}(S=\langle S(T)\rangle, T)\\ &= \frac{1}{2}\left(\mu_S^2 - c_S T^2\right)\langle S(T)\rangle^2 - \frac{\lambda_S}{4}\langle S(T)\rangle^4\\ &\quad - \frac{1}{12\pi} T \sum_{i=\chi,h,S} g_i \left[\left(M_i^2(0,T)\right)^{\frac{3}{2}} - \left(M_i^2(\langle S(T)\rangle, T)\right)^{\frac{3}{2}}\right].\end{aligned} \tag{3.67}$$

For characterizing the GW spectrum, the temperature-dependent parameter $\alpha(T_*)$ has to be evaluated at the tunneling temperature T_* where the proceeding of the phase transition

$\frac{S_C}{T_C}$	T_C [GeV]	L [(GeV)^4]	$e\,(T_C)$ [(GeV)^4]	$\alpha(T_C)$
3.15	$5.49 \cdot 10^{7}$	$2.98 \cdot 10^{26}$	$3.21 \cdot 10^{32}$	$9.274 \cdot 10^{-7}$
1.82	$3.17 \cdot 10^{7}$	$3.31 \cdot 10^{25}$	$3.56 \cdot 10^{31}$	$9.274 \cdot 10^{-7}$
1.41	$2.45 \cdot 10^{7}$	$1.19 \cdot 10^{25}$	$1.28 \cdot 10^{31}$	$9.273 \cdot 10^{-7}$
0.99	$1.73 \cdot 10^{7}$	$2.97 \cdot 10^{24}$	$3.20 \cdot 10^{30}$	$9.272 \cdot 10^{-7}$

Table 3.3: *Results of the numerical analysis for parameter α characterizing the GW spectrum of the singlet extension of the Standard Model.* For the analysis we have chosen a value of $\mu_S^2 = 10^{10}\,(\text{GeV})^2$ setting the temperature scale of the phase transition. In particular, this choice determines the order of magnitude of the latent heat L and the false vacuum energy e, evaluated at the critical temperature. The values for the parameter α are however independent on the choice of the temperature scale, but merely depend on the strength of the phase transition.

starts. However, the rather slight temperature dependence of α (in comparison to those of $\frac{\beta}{H_*}$) allows for an approximate evaluation of α at the critical temperature of the phase transition by assuming $T_* \simeq T_C$. Since the degeneracy of the minimum states causes a vanishing potential difference $\Delta V_{eff}\,(T_C) = 0$ (cf. (3.34)) at the critical temperature, the false-vacuum energy consequently equals the latent heat, $\epsilon\,(T_C) = L$, which is defined in (2.6). After inserting (3.67) in the above equation, the evaluation of (3.65) yields $\alpha(T_C)$. As $\alpha(T_C)$ cannot be calculated analytically in the singlet extension of the Standard Model, we will perform a numerical analysis by determining $\alpha(T_C)$ for different model parameters under the presumption of a strongly first-order phase transition.

Results of the Numerical Analysis

The results of the numerical analysis are presented in Tab. 3.3. Note that the latent heat and the thermal energy density both are proportional to the temperature scale so that the values for the parameter α, defined as the ratio of the latent heat and the thermal energy density, are not dependent on the temperature scale, but are related to the strength of the phase transition. As can been seen in Tab. 3.3, stronger phase transitions lead to an enlargement of the parameter α. However, the dependency of α on the phase transition strength is only marginal in this model. In the range $\frac{S_C}{T_C} = 0.99 \ldots 3.15$ the values for alpha only increase in the range $\alpha = (9.272 \ldots 9.274) \cdot 10^{-7}$. Thus, we obtain in the singlet extension of the Standard Model an upper bound $\alpha \lesssim 9.274 \cdot 10^{-7}$. This maximal value for α is more than six orders of magnitude smaller than $\mathcal{O}(1)$. Due to the correlation of α and $\frac{\beta}{H_*}$, the value for the parameter $\frac{\beta}{H_*}$ will simultaneously be several orders of magnitude bigger than $\mathcal{O}(100)$. Hence, the peak amplitude of the GW spectrum arising from the first-order phase transition in the singlet extension will be significantly too small for lying in the sensitive range of the GW detectors so that the GW spectrum will not be observable. Consequently, gravitational waves cannot serve as probe for the physical conception of the singlet model.

For inducing a strongly first-order phase transition in the singlet model by taking into account the parameter constraints, it is necessary to choose the values for the free parameter λ_m unnaturally small. As the parameter α (via the potential difference $\Delta V_{eff}\,(T)$) incorporates a dependency on the parameter λ_m, this will cause extremely small values of alpha. Physically, this means that the barrier induced by the thermal masses in the effective potential is significantly to low for generating detectable gravitational waves.

Chapter 4

Left-Right Symmetric Model

The most studied mechanism to achieve a strongly first-order phase transition is based on inducing a thermal barrier by the bosonic finite-temperature one-loop contributions. However, as we have seen explicitly in the case of the singlet extension of the Standard Model, the effect of thermally induced barriers is mostly too small to generate strongly first-order phase transitions providing the possibility of detectable gravitational waves. Therefore, we will study the left-right symmetric model of weak interactions in this chapter. The left-right symmetric is not only one of the most promising extensions of the Standard Model being theoretically well motivated, but additionally provides a barrier in the effective potential already at tree-level.

4.1. Concept of Left-Right Symmetric Models

Which basic idea motivates left-right symmetric models? The concept of left-right symmetric models was originally developed with regard to one of the remaining open questions of the Standard Model: the origin of parity violation in weak interactions [162]. While parity violation has to be incorporated in the Standard Model a posteriori by formulating a *chiral* electroweak gauge theory, it arises naturally as a spontaneously broken symmetry in left-right symmetric models.

Within the framework of gauge theories, minimal left-right symmetric models are implemented by extending the electroweak $SU(2)_L \otimes U(1)_Y$ gauge group of the Standard Model to a more naturally appearing

$$SU(2)_L \otimes SU(2)_R \otimes U(1)_{B-L} \tag{4.1}$$

symmetry [169, 163, 190].[1] The extension of the gauge group is associated with an enlargement of the Standard Model particle content by right-handed (Majorana) neutrinos as well as right-handed massive gauge bosons $W_R^{\pm}$ and Z_R. These can give rise to new physical

---

[1] Assuming the underlying gauge symmetry to be $\mathbb{Z}_2 \otimes SU(2)_R \otimes SU(2)_L \otimes U(1)_{B-L}$, two stages of symmetry

impacts.
Since the Lagrangian possesses a discrete left-right symmetry under exchange of the $SU(2)_L$ and $SU(2)_R$ field content, it is intrinsically parity-invariant. By assuming parity symmetry to be spontaneously broken at an energy scale much above the electroweak scale, left-right symmetric models hold the important feature to reproduce the Standard-Model phenomenology correctly at low energies: The right-handed massive gauge bosons would not be experimentally detectible due to their high masses, acquired during the spontaneous parity breaking. Below the symmetry-breaking scale parity violation occurs and thus leads to the observed $V-A$ structure of weak interactions at low energies.

Another deficiency of the Standard Model is the missing physical meaning of the hypercharge Y as generator of the $U(1)$ symmetry. Within left-right symmetric models on the contrary, all generators of the electroweak sector have a direct physical meaning, since the $B-L$ quantum number arises as $U(1)$ generator [161]. The electric charge formula in the left-right symmetric model [29],

$$Q = I_{L_3} + I_{R_3} + \frac{B-L}{2}, \tag{4.2}$$

(with I_{L,R_3} denoting the third component of the weak isospin) is therefore modified in comparison to the Standard Model where $Q = I_{L_3} + \frac{Y}{2}$ [18].

Depending on the restriction to exact or merely close-to-exact left-right symmetry and on the definition of the Higgs sector, different classes and variants of left-right symmetric models exist. In general, the extension of the gauge group for including parity as spontaneous broken symmetry entails an enlargement of the Higgs sector. The additional Higgs representation is required to preserve the $L-R$ symmetry and to generate the correct symmetry breaking pattern, in particular providing the (large) VEV for the generation of the right-handed gauge-boson masses. While all variants of left-right symmetric models include a bidoublet field Φ, the further composition of the minimal Higgs sector to fulfill the above requirements differs. If the Higgs sector, apart from the bidoublet field, is composed of an additional left- and as well as right-handed Higgs *doublet*, the model fails to incorporate a natural explanation for the smallness of the observed neutrino masses via the see-saw mechanism [160, 161]. Since this requirement is however fulfilled in case of left- and right handed *triplet* Higgs fields $\Delta_{L,R}$, we will consider a left-right symmetric model with such a

---

breaking are required to obtain the Standard Model electroweak $SU(2)_L \otimes U(1)_Y$ symmetry [55, 54],

$$\mathbb{Z}_2 \otimes SU(2)_R \otimes SU(2)_L \otimes U(1)_{B-L} \underset{g_L \neq g_R}{\longrightarrow} SU(2)_R \otimes SU(2)_L \otimes U(1)_{B-L} \underset{M_{W_R,Z_R}}{\longrightarrow} SU(2)_L \otimes U(1)_Y$$

where the spontaneous breakdown of the parity symmetry $\mathbb{Z}_2$ at the first stage leads to different gauge couplings $g_L \neq g_R$ [162]. (The left-handed gauge bosons obtain their masses in the subsequent EWPT $SU(2)_L \otimes U(1)_Y \underset{M_{W_L,Z_L}}{\longrightarrow} U(1)_{em}$.)

minimal Higgs sector [190, 159]

$$\begin{aligned} \Phi &= \begin{pmatrix} \phi_1^0 & \phi_1^+ \\ \phi_2^- & \phi_2^0 \end{pmatrix} \mathrel{\widehat{=}} \left(\frac{1}{2}, \frac{1}{2}, 0\right), \\ \Delta_L &= \begin{pmatrix} \frac{\delta_L^+}{\sqrt{2}} & \delta_L^{++} \\ \delta_L^0 & -\frac{\delta_L^+}{\sqrt{2}} \end{pmatrix} \mathrel{\widehat{=}} (1,\, 0,\, 2)\,, \\ \Delta_R &= \begin{pmatrix} \frac{\delta_R^+}{\sqrt{2}} & \delta_R^{++} \\ \delta_R^0 & -\frac{\delta_R^+}{\sqrt{2}} \end{pmatrix} \mathrel{\widehat{=}} (0,\, 1,\, 2)\,. \end{aligned} \tag{4.3}$$

Therein, the electric charge of the single Higgs field components is indicated. The quantum numbers with respect to the $SU(2)_L$, $SU(2)_R$, and $U(1)_{B-L}$ gauge group are denoted in parentheses as convention.
The gauge-boson sector of left-right symmetric models consists of two triplet fields $W^\mu_{L,R}$ and a singlet field B^μ with the following assignment to the $SU(2)_L \otimes SU(2)_R \otimes U(1)_{B-L}$ gauge group [62]

$$W_L^\mu \mathrel{\widehat{=}} (3,\, 1,\, 0)\,, \quad W_R^\mu \mathrel{\widehat{=}} (1,\, 3,\, 0)\,, \quad B^\mu \mathrel{\widehat{=}} (1,\, 1,\, 0)\,. \tag{4.4}$$

Furthermore, the $SU(2)_{L,R}$ charge is assigned to the quarks (and likewise the leptons) in accordance to the left-right symmetry as [28]

$$\begin{aligned} \Psi_{iL} &= \begin{pmatrix} u_i \\ d_i \end{pmatrix}_L \mathrel{\widehat{=}} \left(2,\, 1,\, \frac{1}{3}\right), \\ \Psi_{iR} &= \begin{pmatrix} u_i \\ d_i \end{pmatrix}_R \mathrel{\widehat{=}} \left(1,\, 2,\, \frac{1}{3}\right), \end{aligned} \tag{4.5}$$

wherein $i = 1, 2, 3$ constitutes the generation index. The correct electric charges are obtained from these quantum numbers by use of (4.2).

4.2. Tree-Level Potential

In the considered model, the Lagrangian is required to be intrinsically invariant under the discrete left-right symmetry

$$\Psi_L \leftrightarrow \Psi_R\,,\ \Delta_L \leftrightarrow \Delta_R\,,\ \Phi \leftrightarrow \Phi^\dagger\,, \tag{4.6}$$

whereby Ψ_L and Ψ_R denote any left- and right-handed fermionic field of the theory. In the most general renormalizable form, fulfilling the requirements of gauge-invariance and discrete left-right symmetry, the Lagrangian decomposes into

$$\mathcal{L}_{L-R} = \mathcal{L}_f + \mathcal{L}_{gb} + \mathcal{L}_H\,. \tag{4.7}$$

Therein, the contribution $\mathcal{L}_f$ contains the fermionic kinetic energy terms and Yukawa couplings, whereas $\mathcal{L}_{gb}$ incorporates the kinetic terms of the gauge bosons. The Higgs contribution to the Lagrangian $\mathcal{L}_H$ consequently includes the kinetic energy terms of the scalar sector as well as the scalar interaction terms arising in the tree-level potential. Since we will need the Higgs contribution for further calculations, we deduce its explicit form

$$\begin{aligned}\mathcal{L}_H =& \mathrm{Tr}\left[\left(D_\mu\Phi\right)^\dagger\left(D^\mu\Phi\right)\right] + \mathrm{Tr}\left[\left(D_\mu\Delta_L\right)^\dagger\left(D^\mu\Delta_L\right)\right] + \mathrm{Tr}\left[\left(D_\mu\Delta_R\right)^\dagger\left(D^\mu\Delta_R\right)\right] \\ &- V_0(\Phi, \Delta_L, \Delta_R)\,,\end{aligned} \tag{4.8}$$

where the covariant derivatives of the left-right symmetric $SU(2)_L \otimes SU(2)_R \otimes U(1)_{B-L}$ gauge group are given by

$$\begin{aligned} D_\mu\Phi &\equiv \partial_\mu\Phi + i\frac{g}{2}\left(\sigma_a W^a_{L\mu}\,\Phi - \Phi\,\sigma_a W^a_{L\mu}\right), \\ D_\mu\Delta_L &\equiv \partial_\mu\Delta_L + i\frac{g_L}{2}\left(\sigma_a W^a_{L\mu}\,\Delta_L - \Delta_L\,\sigma_a W^a_{L\mu}\right) + i\frac{g'}{2}\,B_\mu\Delta_L, \\ D_\mu\Delta_R &\equiv \partial_\mu\Delta_R + i\frac{g_R}{2}\left(\sigma_a W^a_{R\mu}\,\Delta_R - \Delta_R\,\sigma_a W^a_{R\mu}\right) + i\frac{g'}{2}\,B_\mu\Delta_R. \end{aligned} \tag{4.9}$$

For deriving a general ansatz of the tree-level $V_0(\Phi, \Delta_L, \Delta_R)$ in (4.8), the requirements of gauge-invariance and left-right symmetry have to be fulfilled. The non-zero $B-L$ quantum number of the triplets Δ_L and Δ_R (cf. (4.3)) additionally forbids trilinear left-right symmetric terms, like $\Phi\Delta_L^\dagger\Delta_R$, in the tree-level potential restricting the allowed terms to quadratic combinations such as $\Delta_L^\dagger\Delta_R$ or $\Delta_L^\dagger\Phi\Delta_R\Phi^\dagger$. The most general form of the tree-level potential $V_0(\Phi, \Delta_L, \Delta_R)$ using the parametrization of [62] reads

$$V_0(\Phi, \Delta_L, \Delta_R) = V_\Phi(\Phi) + V_{\Phi\Delta}(\Phi, \Delta_L, \Delta_R) + V_\Delta(\Delta_L, \Delta_R)\,, \tag{4.10}$$

decomposed of a pure Higgs-bidoublet potential

$$\begin{aligned} V_\Phi(\Phi) = & -\mu_1^2\,\mathrm{Tr}\left(\Phi\Phi^\dagger\right) - \mu_2^2\left[\mathrm{Tr}\left(\tilde{\Phi}\Phi^\dagger\right) + \mathrm{Tr}\left(\Phi\tilde{\Phi}^\dagger\right)\right] \\ & + \lambda_1\left[\mathrm{Tr}\left(\Phi\Phi^\dagger\right)\right]^2 + \lambda_2\left\{\left[\mathrm{Tr}\left(\tilde{\Phi}\Phi^\dagger\right)\right]^2 + \left[\mathrm{Tr}\left(\Phi\tilde{\Phi}^\dagger\right)\right]^2\right\} \\ & + \lambda_3\left[\mathrm{Tr}\left(\tilde{\Phi}\Phi^\dagger\right)\right]\cdot\left[\mathrm{Tr}\left(\Phi\tilde{\Phi}^\dagger\right)\right] \\ & + \lambda_4\left\{\mathrm{Tr}\left(\Phi\Phi^\dagger\right)\left[\mathrm{Tr}\left(\tilde{\Phi}\Phi^\dagger\right) + \mathrm{Tr}\left(\Phi\tilde{\Phi}^\dagger\right)\right]\right\} \end{aligned} \tag{4.11}$$

with $\tilde{\Phi} \equiv \sigma_2\Phi^*\sigma_2$ [28], a bidoublet-triplet contribution

$$\begin{aligned} V_{\Phi\Delta}\left(\Phi, \Delta_L, \Delta_R\right) = \alpha_1 & \left\{\mathrm{Tr}\left(\Phi\Phi^\dagger\right)\left[\mathrm{Tr}\left(\Delta_L\Delta_L^\dagger\right) + \mathrm{Tr}\left(\Delta_R\Delta_R^\dagger\right)\right]\right\} \\ + \alpha_2 & \left\{\mathrm{Tr}\left(\tilde{\Phi}^\dagger\Phi\right)\left[\mathrm{Tr}\left(\Delta_L\Delta_L^\dagger\right) + \mathrm{Tr}\left(\Delta_R\Delta_R^\dagger\right)\right]\right\} \\ + \alpha_2^* & \left\{\mathrm{Tr}\left(\tilde{\Phi}\Phi^\dagger\right)\left[\mathrm{Tr}\left(\Delta_L\Delta_L^\dagger\right) + \mathrm{Tr}\left(\Delta_R\Delta_R^\dagger\right)\right]\right\} \\ + \alpha_3 & \left[\mathrm{Tr}\left(\Phi\Phi^\dagger\Delta_L\Delta_L^\dagger\right) + \mathrm{Tr}\left(\Phi\Phi^\dagger\Delta_R\Delta_R^\dagger\right)\right] \\ + \beta_1 & \left[\mathrm{Tr}\left(\Phi\Delta_R\Phi^\dagger\Delta_L^\dagger\right) + \mathrm{Tr}\left(\Phi^\dagger\Delta_L\Phi\Delta_R^\dagger\right)\right] \\ + \beta_2 & \left[\mathrm{Tr}\left(\tilde{\Phi}\Delta_R\Phi^\dagger\Delta_L^+\right) + \mathrm{Tr}\left(\tilde{\Phi}^\dagger\Delta_L\Phi\Delta_R^\dagger\right)\right] \\ + \beta_3 & \left[\mathrm{Tr}\left(\Phi\Delta_R\tilde{\Phi}^\dagger\Delta_L^\dagger\right) + \mathrm{Tr}\left(\Phi^\dagger\Delta_L\tilde{\Phi}\Delta_R^\dagger\right)\right] \end{aligned} \tag{4.12}$$

and a pure triplet potential

$$\begin{aligned} V_\Delta\left(\Delta_L, \Delta_R\right) = &-\mu_3^2 \operatorname{Tr}\left(\Delta_L^\dagger \Delta_L + \Delta_R^\dagger \Delta_R\right) \\ &+ \varrho_1 \left\{\left[\operatorname{Tr}\left(\Delta_L^\dagger \Delta_L\right)\right]^2 + \left[\operatorname{Tr}\left(\Delta_R^\dagger \Delta_R\right)\right]^2\right\} \\ &+ \varrho_2 \left\{\left[\operatorname{Tr}\left(\Delta_L^\dagger \Delta_L^\dagger\right)\right] \cdot \left[\operatorname{Tr}\left(\Delta_L \Delta_L\right)\right] + \left[\operatorname{Tr}\left(\Delta_R^\dagger \Delta_R^\dagger\right)\right] \cdot \left[\operatorname{Tr}\left(\Delta_R \Delta_R\right)\right]\right\} \\ &+ \varrho_3 \left[\operatorname{Tr}\left(\Delta_L^\dagger \Delta_L\right)\right] \cdot \left[\operatorname{Tr}\left(\Delta_R^\dagger \Delta_R\right)\right] \\ &+ \varrho_4 \left\{\left[\operatorname{Tr}\left(\Delta_L \Delta_L\right)\right] \cdot \left[\operatorname{Tr}\left(\Delta_R^\dagger \Delta_R^\dagger\right)\right] + \left[\operatorname{Tr}\left(\Delta_L^\dagger \Delta_L^\dagger\right)\right] \cdot \left[\operatorname{Tr}\left(\Delta_R \Delta_R\right)\right]\right\} . \end{aligned} \tag{4.13}$$

Note that the imposed left-right symmetry, as defined in (4.6), restricts the single terms of the tree-level potential to be self-conjugate and consequently the occurring parameters (except α_2)[2] to be real.

4.2.1. Mean-Field Approximation

In order to investigate phase-transition scenarios arising from the above tree-level potential $V_0(\Phi, \Delta_L, \Delta_R)$, it is essential to study the potential's behavior in dependence of the scalar-sector VEVs $\langle\Phi\rangle$, $\langle\Delta_L\rangle$ and $\langle\Delta_R\rangle$. Thus, we will use the mean-field approximation, by expressing the tree-level potential in terms of the VEVs, in our further considerations.

When the left- and right-handed triplets Δ_L and Δ_R acquire their VEVs, spontaneous breaking of the $B-L$ quantum number and additionally of parity symmetry, in case of $\langle\Delta_L\rangle \neq \langle\Delta_R\rangle$, occurs. Because of electric charge conservation, only the neutral components of the three scalar fields, ϕ_1^0, ϕ_2^0, δ_L^0 and δ_R^0, are allowed to acquire VEVS which we denote by the real parameters k_1, k_2,v_L and v_R, respectively. Therefore, the most general ansatz for the VEVs of the scalar fields reads [94, 184]

$$\langle\Phi\rangle = \begin{pmatrix} k_1 & 0 \\ 0 & k_2 \end{pmatrix}, \; \langle\Delta_L\rangle = \begin{pmatrix} 0 & 0 \\ v_L & 0 \end{pmatrix}, \; \langle\Delta_L\rangle = \begin{pmatrix} 0 & 0 \\ v_R & 0 \end{pmatrix}, \tag{4.14}$$

wherein the phenomenologically required separation of the $L-R$ symmetry-breaking scale from the electroweak scale imposes the constraint $v_R \gg k_{1,2}$.[3]

In our further considerations, we will need the explicit form of the pure triplet contribution to the tree-level potential, given in (4.13) in the mean-field approximation and therefore display it here separately. After inserting the VEVs of the scalar fields of (4.14) in (4.11), the only non-vanishing terms, arising to be $\operatorname{Tr}\left(\langle\Delta_L^\dagger\rangle\langle\Delta_L\rangle\right) = v_L^2$, $\operatorname{Tr}\left(\langle\Delta_R^\dagger\rangle\langle\Delta_R\rangle\right) = v_R^2$, reduce the triplet contribution to the effective potential in the mean-field approximation to

$$V_\Delta(v_L, v_R) = -\mu_3^2 \left(v_L^2 + v_R^2\right) + \varrho_1 \left(v_L^4 + v_R^4\right) + \varrho_3 \, v_L^4 \cdot v_R^4 \tag{4.15}$$

---

[2] The parameter α_2 has to be taken real by requiring the tree-level potential to be initially CP invariant allowing for spontaneous CP violation [73].

[3] Spontaneous CP violation is achieved by including a non-vanishing phase factor $e^{i\theta}$, $\theta \in \mathbb{R}$, in the ansatz for the bidoublet VEV $\langle\Phi\rangle$ [93, 62].

4.3. Effective Potential

In this section we will determine the one-loop effective potential at finite temperature which will be our main tool for the investigation of phase-transition scenarios arising in the left-right symmetric model. According to (1.51), the one-loop effective potential consists of the tree-level potential, given in (3.3)-(4.13) for the left-right symmetric model, complemented by the zero- and finite-temperature one-loop corrections including the ring-diagrams

$$\begin{aligned} V_{eff}(\Phi, \Delta_L, \Delta_R, T) = V_0(\Phi, \Delta_L, \Delta_R) + V_1^{T=0}(\Phi, \Delta_L, \Delta_R) \\ + V_1^{T\neq 0}(\Phi, \Delta_L, \Delta_R, T) + V_{ring}(\Phi, \Delta_L, \Delta_R, T)\,. \end{aligned} \tag{4.16}$$

We will focus on phase transitions occurring at the $L-R$ symmetry breaking scale, which is assumed to lie significantly above the electroweak scale ,$T_{L-R} > T_{EW}$. Hence, the behavior of the effective potential will be dominated by the dependence on the left- and right-handed triplet fields $\Delta_{L,R}$ so that the Higgs-bidoublet sector Φ in the effective potential can be neglected, $V_{eff}(\Phi, \Delta_L, \Delta_R, T) \simeq V_{eff}(\Delta_L, \Delta_R, T)$. This results in particular in a reduction of the tree-level potential $V_0(\Phi, \Delta_L, \Delta_R)$ (cf. (4.10)) to the pure triplet potential $V_\Delta(\Delta_L, \Delta_R)$, given in (4.13).

Due to the high temperature scale of the $L-R$ symmetry breaking, the dominant correction to the tree-level potential will arise from the finite-temperature one-loop contribution $V_1^{T=0}(\Delta_L, \Delta_R)$, including the quadratic field-dependent mass-terms $\propto T^2\, m_i^2(\Delta_L, \Delta_R)$. Therefore, we will neglect the zero-temperature one-loop $V_1^{T=0}(\Delta_L, \Delta_R)$ (cf. (3.32)) in the calculation of the effective potential.

In the following chapter we will study a phase-transition scenario in the left-right symmetric model where the barrier between the minima of the effective potential is not induced by the cubic terms of the finite-temperature corrections, but arises already within the tree-level potential. In this case, it is sufficient to consider only the leading-order terms of the finite-temperature one-loop correction, ignoring the cubic terms of the field-dependent and thermal masses, respectively [82]. Thus, we will not have to regard the ring-diagram corrections $V_{ring}(\Delta_L, \Delta_R, T)$ including the thermal masses in the effective potential.

Given the previous conditions, the effective potential at $L-R$ symmetry-breaking temperatures reduces to

$$V_{eff}(\Delta_L, \Delta_R, T) \simeq V_\Delta(\Delta_L, \Delta_R) + V_1^{T\neq 0}(\Delta_L, \Delta_R, T)\,, \tag{4.17}$$

where the bidoublet tree-level potential in the mean-field approximation is derived in (4.15). For determining the explicit form of the effective potential, we now have to compute the thermal one-loop correction $V_1^{T\neq 0}(\Delta_L, \Delta_R, T)$ to the tree-level potential.

4.3.1. One-Loop Effective Potential at Finite Temperature

The general form of the one-loop contribution in the high-temperature expansion arises as (cf. (3.32)),

$$V_1^{T\neq 0}(\Phi, \Delta_L, \Delta_R, T) = \frac{T^4}{2\pi^2} \sum_i \bar{g_i}\, J_{F,B}\left(\frac{m_i^2(\Phi, \Delta_L, \Delta_R)}{T^2}\right), \tag{4.18}$$

where $\bar{g}_i$ denotes the modified degrees of freedom of the corresponding particle and the summation index i includes all fermions and bosons of the left-right symmetric model with corresponding fermionic and bosonic functions $J_{B,F}$, in dependence of the field-dependent masses $m_i^2(\Phi, \Delta_L, \Delta_R)$.
However, at the left-right symmetry breaking scale, the sum over the model's particle content will be dominated by the mass-contributions of the left- and right-handed gauge bosons, $W_L^\pm$, $W_R^\pm$, Z_L and Z_R.[4] Consequently, only the latter will be included in the calculation of the thermal one-loop correction.
According to (1.40), the high-temperature expansion of the bosonic function J_B, including terms up to leading-order in the field-dependent masses, is given approximately given by

$$J_B\left(\frac{m_i^2(\Phi, \Delta_L, \Delta_R)}{T^2}\right) \simeq -\frac{\pi^4}{45} + \frac{\pi^2}{12}\,\frac{m_i^2(\Phi, \Delta_L, \Delta_R)}{T^2} \quad . \tag{4.19}$$

Hence, by neglecting the Higgs-triplet sector Φ and proceeding to the mean-field description in dependence of the VEVs v_L and v_R, the one-loop finite-temperature correction consists in

$$V_1^{T\neq 0}(v_L, v_R, T) = \sum_{i=W^\pm_{L,R}, Z_{L,R}} \bar{g}_i \left[-\frac{\pi^2}{90}\,T^4 + \frac{1}{24}\,T^2 m_i^2(v_L, v_R)\right]. \tag{4.20}$$

The modified degrees of freedom remain unchanged for the left-handed gauge bosons in comparison to the Standard Model (cf. (3.8)). Due to the imposed left-right symmetry, the right-handed gauge bosons are provided with degrees of freedom identical to those of the corresponding left-handed particles so that

$$\begin{aligned} \bar{g}_{W_R} &\equiv \bar{g}_{W_L} = 2 \cdot 3 = 6, \\ \bar{g}_{Z_R} &\equiv \bar{g}_{Z_L} = 3. \end{aligned} \tag{4.21}$$

In Sec. B.1 of the appendix, we compute the field-dependent masses for the gauge-bosons in the left-right symmetric model. The resulting expressions in the mean-field approximation are given by

$$\begin{aligned} m^2_{W_L}(v_L) &= \frac{g_L^2}{4}\,v_L^2\,, \\ m^2_{W_R}(v_R) &= \frac{g_R^2}{4}\,v_R^2\,, \\ m^2_{Z_{L,R}}(v_L, v_R) &= \frac{1}{8}\Big\{\left(g_L^2 + g'^2\right)v_L^2 + \left(g_R^2 + g'^2\right)v_R^2 \\ &\qquad \mp \sqrt{\left[\left(g_L^2 + g'^2\right)v_L^2 + \left(g_R^2 + g'^2\right)v_R^2\right]^2 + 4g'^4\,v_L^2 v_R^2}\Big\}. \end{aligned} \tag{4.22}$$

---

[4] In analogy to the Standard Model, the photons γ remains massless in the left-right symmetric model (cf. Sec. B.1).

After inserting (4.21) and (4.22) in (4.20) and simplifying the terms arising from the gauge-boson masses, we obtain the final expression for the one-loop finite-temperature contribution to the effective potential

$$\begin{aligned} V_1^{T\neq 0}(v_L, v_R, T) &= -\frac{\pi^4}{5}\,T^4 + \frac{1}{8}\,T^2\left[2m_{W_L}^2(v_L) + 2m_{W_R}^2(v_R) + m_{Z_L}^2(v_L, v_R) + m_{Z_R}^2(v_L, v_R)\right] \\ &= -\frac{\pi^4}{5}\,T^4 + T^2\left[\frac{3g_L^2 + g'^2}{32}\,v_L^2 + \frac{3g_L^2 + g'^2}{32}\,v_R^2\right]. \end{aligned} \tag{4.23}$$

In conclusion, the complete effective potential in the mean-field approximation, providing the basic ingredient for the further investigation of phase-transition scenarios in the left-right-symmetric model, arises as (cf. (4.17))

$$\begin{aligned} V_{eff}(v_L, v_R, T) &\simeq V_\Delta(v_L, v_R) + V_1^{T\neq 0}(v_L, v_R, T) \\ &= -\mu_3^2\left(v_L^2 + v_R^2\right) + \varrho_1\left(v_L^4 + v_R^4\right) + \varrho_3\, v_L^2 \cdot v_R^2 \\ &\quad - \frac{\pi^4}{5}\,T^4 + T^2\left[\frac{3g_L^2 + g'^2}{32}\,v_L^2 + \frac{3g_L^2 + g'^2}{32}\,v_R^2\right]. \end{aligned} \tag{4.24}$$

4.4. Investigation of the Phase Transition

Which phase-transition scenarios can we expect from this potential? The conception of left-right symmetric models incorporates in general two distinct phase transitions, the $L-R$ symmetry breaking phase transition and the EWPT. The latter has been treated in several variants of the left-right symmetric model [73, 58, 29, 115, 116] (including supersymmetric and unified extensions [55, 54, 184] and with regard to different cosmological implications such as CP violation [56, 28], baryogenesis via leptogenesis and bounds on the neutrino masses [164, 93, 94, 183, 27, 117, 182] or topological defects such as domain walls [143, 209, 208, 62].

Our intention however is to study the $L-R$ symmetry breaking phase transition at temperatures between the electroweak and the GUT scale and to investigate whether the gravitational waves, generated by a strongly first-order phase transition, can serve as cosmological probes for the physical concept of the left-right symmetric model. A possibility for enhancing the strength of a phase transition significantly is provided by considering the phase transition in the case of flat directions of the effective potential, as proposed in [82] for the singlet extension of the Standard Model. In the following section, we will apply this scenario of flat directions to the left-right symmetric model.

4.4.1. Phase-Transition Scenario

For the left-right symmetric model we will discuss the phase-transition scenario which is shown in Tab. 4.1. Due to symmetry restoration at very high temperatures, the absolute stable minimum of the effective potential is initially located at the origin $(\Delta_L, \Delta_R) = (0, 0)$. As

the temperature is lowered, the left-handed triplet field Δ_L develops a second minimum of the effective potential. At a certain critical temperature T_L both minima become degenerate inducing a phase transition $(0, 0) \to (v_L(T_L), 0)$, whereby the left-handed triplet field acquires a VEV $v_L(T_L)$. (Note that we will restrict our considerations in the left-right symmetric model, due to simplicity, to positive values of the VEVs. In general, the left- and right-handed triplet fields can acquire VEVs $\pm v_{L,R}(T)$.)
By the decrease of the temperature, the left-handed minimum $(v_L(T), 0)$ of the effective potential is lowered. Simultaneously, the right-handed triplet-fields Δ_R forms a minimum leading to the emergence of a barrier. When both minima become degenerate at the critical temperature $T_R \equiv T_C$ a first-order phase transition from the pure left-handed minimum state to the pure right-handed one,

$$(v_L(T_C), 0) \to (0, v_R(T_C)), \tag{4.25}$$

proceeds so that the right-handed triplet field acquires a VEV $v_R(T_C)$. This will be the phase transition we will investigate in detail in the further sections. Below the critical temperature, the right-handed minimum at $(0, v_R(T))$ evolves with the temperature to its zero-temperature value.[5]

The phase-transition scenario described above requires in particular a small deviation from the exact $L - R$ symmetry in the tree-level potential of (4.24) to allow for a successive development of the left- and right-handed minimum. (Otherwise both minima would be degenerated at any temperature). [6]If we therefore replace the parameter μ_3^2 in the tree-level potential by two distinct parameters $\mu_L^2 \neq \mu_R^2$ (with $\mu_{L,R}^2 > 0$), (4.24) transforms into

$$\begin{aligned} V_{eff}(v_L, v_R, T) = &\left(-\mu_L^2 + \frac{3g_L^2 + g'^2}{32} T^2\right) v_L^2 + \left(-\mu_R^2 + \frac{3g_R^2 + g'^2}{32} T^2\right) v_R^2 \\ &+ \frac{\lambda}{4}\left(v_L^4 + v_R^4\right) + \frac{\lambda_m}{4} v_L^2 v_R^2, \end{aligned} \tag{4.26}$$

where we have additionally neglected the physically irrelevant T^4-term and have redefined the parameters as $\varrho_1 \equiv \frac{\lambda}{4}$ and $\varrho_3 \equiv \frac{\lambda_m}{4}$ with $\lambda, \lambda_m \in \mathbb{R}$. Since the tree-level potential has to be bounded from below to ensure vacuum stability, the restriction $\lambda > 0$ is required. The parameter λ_m in generally can be either positive or negative. We will henceforth consider the case where $\lambda_m > 0$. Note in particular that the term $\frac{\lambda_m}{4} v_L^2 v_R^2$ generates the tree-level barrier in the effective potential determining the phase transition to be of first-order.

4.4.2. Conditions for a First-Order Phase Transition

We will now derive the functional dependence of the VEVs $v_{L,R}$ and the critical temperature T_C on the model parameters. Their form is imposed by the conditions for generating the

---

[5] At $T = T_{EW}$, the spontaneous breakdown of the $SU(2)_L \otimes U(1)_Y$ symmetry to $U(1)_{em}$ induces the EWPT, wherein the bidoublet field Φ (cf. (4.14)) acquires a left-handed VEV providing the masses for the left-handed gauge-bosons.

[6] A possible reason for a deviation from exact $L - R$ symmetry could be for instance a suppression of terms at the $L - R$ breaking scale if the model is descended from another unified model [62].

Scale	T	**Physical behavior**	**Minimum of V_{eff} at (Δ_L, Δ_R)**
GUT Scale	$T_{GUT} \simeq 10^{16}$ GeV		
L − R Symmetry Scale	$\gg T_L$	Symmetry restoration	$(0, 0)$
	T_L	Phase transition (left-handed triplet acquires VEV v_L)	$(0, 0) \rightarrow (v_L(T_L), 0)$ (degenerated minima)
	$< T_L$	Left-handed triplet VEV v_L	$(v_L(T), 0)$
	$T_R \equiv T_C$	First-order phase transition, (right-handed triplet acquires VEV v_L)	$(v_L(T_C), 0) \rightarrow (0, v_R(T_C))$ (degenerated minima)
	$< T_R$	Right-handed triplet VEV v_R	$(0, v_R(T))$
EW Scale	$T_{EW} \simeq 10^2$ GeV		

Table 4.1: *Considered phase-transition scenario in the left-right symmetric model.* We will investigate the first-order phase transition from the pure left-handed minimum state to the pure right-handed one proceeding at the critical temperature $T_R \equiv T_C$. (Note that we have denoted only positive VEVs of the left- and right-handed triplet fields.)

desired phase-transition scenario. In particular, the emergence of a barrier at the critical temperature, separating the left- and right-handed VEV, classifies the phase transition to be of first order. Thus, we will have to apply the conditions in (3.33) and (3.34) of Sec. 3.3.2 to the effective potential of (4.26). The starting point of our calculations will be the determination of the temperature-dependent left- and right-handed local minima of the effective potential.

Temperature-Dependent Left- and Right-Handed Minima

The left- and right-handed VEVs form degenerated minima of the effective potential $V_{eff}(v_L, v_R, T)$ at the critical temperature of the phase transition. They emerge as temperature-dependent non-zero stationary points $v_{L,R_{stat}}$ of the effective potential and are located on curves $D_{L,R}(T)$ with vanishing first derivative of the effective potential [82],

$$\frac{\partial V_{eff}(v_L, v_R, T)}{\partial v_R} = 0 \quad \Rightarrow \left\{ v^2_{R_{stat}} = 0,\ v^2_{R_{stat}} \equiv D^2_R(v_L, T) \right\}, \tag{4.27}$$

$$\frac{\partial V_{eff}(v_L, v_R, T)}{\partial v_L} = 0 \quad \Rightarrow \left\{ v^2_{L_{stat}} = 0,\ v^2_{L_{stat}}(v_R, T) \neq 0 \Rightarrow v^2_R \equiv D^2_L(v_{L_{stat}}, T) \right\}. \tag{4.28}$$

If we parametrize the curves with vanishing first derivative, arising from the effective potential of (4.26), in terms of v_L and T,

$$D_R^2(v_L, T) = \frac{1}{2\lambda}\left[4\mu_R^2 - \lambda_m v_L^2 - \frac{3g_R^2 + g'^2}{8}\,T^2\right], \tag{4.29}$$

$$D_L^2(v_L, T) = \frac{1}{\lambda_m}\left[4\mu_L^2 - 2\lambda v_L^2 - \frac{3g_L^2 + g'^2}{8}\,T^2\right], \tag{4.30}$$

their functional behavior becomes evident: They constitute parabolas which differ in the widths,[7] but possess a common symmetry axis at $v_L = 0$. With increasing temperature T the curves approach this axis so that symmetry restoration ($v_L = 0$) is ensured at high temperatures. At the intersection points of the parabolas, $D_L^2(v_L, T) = D_R^2(v_L, T)$, the effective potential develops coinciding left- and right-handed stationary points, $v_{L_{stat}}^2(T)$ and $v_{R_{stat}}^2(T)$ (determined via 4.28). These constitute left- and right-handed minima of the form

$$\begin{aligned} v_L(T) &= \sqrt{\frac{1}{4\lambda^2 - \lambda_m^2}\left[4\left(2\lambda\mu_L^2 - \lambda_m\mu_R^2\right) - \frac{3\left(2\lambda g_L^2 - \lambda_m g_R^2\right) + (2\lambda - \lambda_m)\,g'^2}{8}\,T^2\right]}, \\ v_R(T) &= \sqrt{\frac{1}{4\lambda^2 - \lambda_m^2}\left[4\left(2\lambda\mu_R^2 - \lambda_m\mu_L^2\right) - \frac{3\left(2\lambda g_R^2 - \lambda_m g_L^2\right) + (2\lambda - \lambda_m)\,g'^2}{8}\,T^2\right]}, \end{aligned} \tag{4.31}$$

if additionally the sufficient condition for local minima of (4.40) is fulfilled by requiring $\lambda > \frac{\lambda_m}{2}$.

Critical Temperature

The critical temperature T_C for the considered phase transition (cf. Tab. 4.1) from the pure left-handed minimum state to the respective right-handed one, $(v_L(T_C), 0) \rightarrow (0, v_R(T_C))$, can now be calculated from the condition of degeneracy of the minima: At $T = T_C$ the left- and right-handed minimum become degenerate so that their potential difference has to vanish (cf. (3.34))

$$\Delta V_{eff}(T)\Big|_{T=T_C} = 0. \tag{4.32}$$

Therein, the difference $\Delta V_{eff}(T) \equiv V_{eff}(v_L(T), 0, T) - V_{eff}(0, v_R(T), T)$, arising from the effective potential of (4.26) by insertion of the left- and right handed minima in (4.31), is given by

$$\Delta V_{eff}(T)\Big|_{T=T_C} = \frac{\lambda}{4\lambda^2 - \lambda_m^2}\left[c_1(g)\,T_C^4 - c_2\left(g, \mu^2\right)T_C^2 + c_3\left(\mu^2\right)\right] \tag{4.33}$$

---

[7] Note that the case of identical widths, where the curves $D_{L,R}(v_L, T)$ overlie each other, gives rise to flat directions of the effective potential. We will discuss this in more detail in Sec. 4.4.3.

with

$$\begin{aligned} c_1(g) &\equiv \frac{3}{256}\left(g_R^2 - g_L^2\right)\left[3\left(g_R^2 + g_L^2\right) + 2g'^2\right], \\ c_2\left(g, \mu^2\right) &\equiv \frac{1}{4}\left[3\left(g_R^2\mu_R^2 - g_L^2\mu_L^2\right) + g'^2\left(\mu_R^2 - \mu_L^2\right)\right], \\ c_3\left(\mu^2\right) &\equiv 4\left(\mu_R^2 - \mu_L^2\right). \end{aligned} \tag{4.34}$$

(Herein, we have indicated the functional dependence of the prefactors $c_{1,2,3}$ on $g_{L,R}$ and g' by "g" and on $\mu_{L,R}^2$ by "μ^2".)
Consequently, (4.32) yields a quartic equation with respect to T_C. Due to the restriction to $T_C > 0$ and by requiring consistency with the total symmetric case $\mu_R^2 \equiv \mu_L^2$ (cf. (4.24)), where the minima are degenerated at any temperature and hence $T_C = 0$, the four solutions of (4.32) for the critical temperature reduce to one unique result

$$T_C = 4\sqrt{\frac{2\left(\mu_R^2 - \mu_L^2\right)}{3\left(g_R^2 - g_L^2\right)}}, \tag{4.35}$$

where the conditions $g_R > g_L$ and $\mu_R^2 > \mu_L^2$, emerging from the parameter constraints in Sec. 4.4.3, have to be satisfied (and guarantee T_C to be real).

Left- and Right-Handed VEVs at the Critical Temperature

By inserting (4.35) in the expressions for the left- and right-handed minima (cf. (4.31)), we can subsequently determine the VEVs of the effective potential at the critical temperature T_C. The left-handed false vacuum and the right-handed true vacuum turn out to possess identical values at the critical temperature (so that the potential difference of the pure left- and right handed minimum state per se vanishes). We are therefore able to summarize the expressions for the VEVs at the critical temperature by $v_C \equiv v_L(T_C) = v_R(T_C)$ where

$$v_C = \sqrt{\frac{1}{2\lambda + \lambda_m}\,\frac{4\left[3\left(g_R^2\mu_L^2 - g_L^2\mu_R^2\right) - g'^2\left(\mu_R^2 - \mu_L^2\right)\right]}{3\left(g_R^2 - g_L^2\right)}}. \tag{4.36}$$

Strength of the Phase Transition

The determination of the critical temperature and the respective VEVs allows for calculating the strength of the phase transition, defined according to (3.36) as the ratio of the broken phase VEV and the critical temperature

$$\frac{v_C}{T_C} = \frac{1}{4}\sqrt{\frac{1}{2\lambda + \lambda_m}\left(3\,\frac{g_R^2\mu_L^2 - g_L^2\mu_R^2}{\mu_R^2 - \mu_L^2} - g'^2\right)}. \tag{4.37}$$

Note that in contrast to the singlet extension of the Standard Model, where the strength of the phase transition only depends on the (dimensionless) small couplings (cf. (3.47)), (4.37) includes the dimensionful parameters $\mu^2_{L,R}$ setting the temperature scale. But since the strength of the phase transition is dimensionless, it cannot depend on the temperature scale itself, but only on the ratio between μ^2_L and μ^2_R.[8] This fact will be crucial with regard to the detectability of the GW spectrum from the considered phase transition in the L-R symmetric model: We will choose an appropriate temperature scale generating a peak frequency $\tilde{f}$ within the detectable frequency region, but will be able, by the choice of the ratio between μ^2_L and μ^2_R, to enlarge the strength of the phase transition and hence the height of the GW amplitude $h^2_o\tilde{\Omega}_{GW}$ independently from the temperature scale.

4.4.3. Parameter Constraints

The choice of parameters is restricted by the parameter constraints necessary to preserve the physically relevant features of the appearing quantities and for the considered phase-transition scenario. In detail, the following parameter constraints emerge in the left-right symmetric model:

Vacuum Stability. To ensure the vacuum stability of the theory, the tree-level potential $V_0(v_L, v_R)$ of (4.26),

$$V_0(v_L, v_R) \equiv -\mu^2_L v^2_L - \mu^2_R v^2_R + \frac{\lambda}{4}\left(v^4_L + v^4_R\right) + \frac{\lambda_m}{4} v^2_L v^2_R \tag{4.38}$$

with $\mu^2_{L,R}$, λ, $\lambda_m > 0$, has to be bounded from below. Analogously to Sec. 3.3.3, it has to reach infinity when the mean-fields $v_{L,R}$ become infinite in any direction. The large-field behavior of the tree-level potential is determined by the quartic contributions of the fields $v_{L,R}$. Since we have chosen $\lambda_m > 0$ in Sec. 4.4.1, vacuum stability is maintained in case of

$$\lambda > \lambda_m. \tag{4.39}$$

Sufficient Conditions for Local Minima. In addition to the necessary conditions, given in (4.27) and (4.28), the left- and right-handed minimum have to fulfill the sufficient conditions

$$\left.\frac{\partial^2 V_{eff}\left(v_L(T), v_R, T\right)}{\partial v^2_R}\right|_{v_R=\langle v_R(T)\rangle} > 0, \qquad \left.\frac{\partial^2 V_{eff}\left(v_L, v_R(T), T\right)}{\partial v^2_L}\right|_{v_L=\langle v_L(T)\rangle} > 0. \tag{4.40}$$

Both inequalities turn out to be satisfied in case of

$$\lambda > \frac{\lambda_m}{2}. \tag{4.41}$$

---

[8] This can be easily seen by expressing μ^2_L as $\mu^2_L = x \cdot \mu^2_R$ with $\frac{\mu^2_{L_{min}}}{\mu^2_R} \leq x \leq \frac{\mu^2_{L_{max}}}{\mu^2_R}$ (where the allowed range of x will have to be determined by the parameter constraints).

As we will see in Sec. 4.4.3, the limiting case of flat directions arises for $\lambda = \frac{\lambda_m}{2}$ so that we will choose the parameters randomly in accordance with the constraint (4.41). Hence, this constraint consists an improvement of the bound derived in (4.39).

Consistency with the Standard Model. At low energies, the left-right symmetric model has to reproduce the phenomenology of the Standard Model. Since we have assumed the bidoublet field to acquire a left-handed VEV at the electroweak scale (cf. Sec. 4.4.1) evolving with T down to the (experimentally determined) zero-temperature Higgs VEV, the observed left-handed gauge boson masses will arise correctly if the parameters g_L and g' equal their Standard Model values [58],[9]

$$g_L \simeq 0.64, \quad g' \simeq 0.35. \tag{4.42}$$

Physically Viability of the Critical Temperature. To be a physically viable quantity, the critical temperature in particular has to be real, i.e. $T_C^2 > 0$. Since the physical concept of the left-right symmetric model bases on the assumption that

$$g_R > g_L, \tag{4.43}$$

the critical temperature, as computed in (4.35), is real if additionally the constraint

$$\mu_R^2 > \mu_L^2 \tag{4.44}$$

is fulfilled.

Physically Viability of the VEV v_C. The same condition for physical viability holds true for the VEV v_C. The requirement of a real VEV, $v_C^2 > 0$, applied to the result of (4.36) imposes a *lower* bound on the parameter μ_L^2,

$$\mu_L^2 > \frac{3g_L^2 + g'^2}{3g_R^2 + g'^2}\, \mu_R^2 \equiv \mu_{L_{min}}^2. \tag{4.45}$$

In case of $\mu_L^2 = \mu_{L_{min}}^2$ the VEV v_C vanishes.

Broken Right-Handed Minimum. For temperatures $T \leq T_C$ the right-handed minimum is required to form the broken vacuum state. The condition for the phase transition to proceed, guaranteeing the right-handed minimum to be the deepest, yields [82]

$$\left. \frac{d^2 \Delta V_{eff}(T)}{dT^2} \right|_{T=T_C} > 0 \tag{4.46}$$

---

[9] Note that we do not take account of running couplings in this context. The above couplings g_L and g' are given at the Z-pole.

Parameter	**Constraint**		**Free**
λ_m	/		√
λ	$\lambda > \frac{\lambda_m}{2}$	(4.41)	×
g_L	$g_L \simeq 0.64$	(4.42)	×
g'	$g' \simeq 0.35$		×
g_R	$g_R > g_L$	(4.43)	×
μ_R^2	/		√
μ_L^2	$\mu_{L_{max}}^2 > \mu_L^2 > \mu_{L_{min}}^2$ with		
	$\mu_{L_{max}}^2 \equiv \frac{3\left(3g_L^2+2g_R^2\right)+5g'^2}{3\left(3g_R^2+2g_L^2\right)+5g'^2}\,\mu_R^2$	(4.47)	×
	$\mu_{L_{min}}^2 \equiv \frac{3g_L^2+g'^2}{3g_R^2+g'^2}\,\mu_R^2$	(4.45)	×

Table 4.2: *Free and constrained parameters in the left-right symmetric model.* The remaining free parameters of the left-right symmetric model are λ_m and μ_R^2. While λ_m will dominantly determine the strength of the phase transition, the parameter μ_R^2 will set the temperature scale. Apart from the parameters g_L and g', which are dictated by their Standard Model values, we will choose the parameters λ, g_L and μ_L^2 randomly with respect to the parameter constraints.

with $\Delta V_{eff}(T)$ given in (4.33)-(4.34). By including the condition $\lambda > \frac{\lambda_m}{2}$ and assuming $g_R > g_L$, the above expression transforms into an *upper* bound on μ_L^2,

$$\mu_{L_{max}}^2 \equiv \frac{3\left(3g_L^2 + 2g_R^2\right) + 5g'^2}{3\left(3g_R^2 + 2g_L^2\right) + 5g'^2}\,\mu_R^2 > \mu_L^2, \tag{4.47}$$

which in particular implies $\mu_R^2 > \mu_L^2$. In combination with the lower bound in (4.45), this constraint restricts the parameter μ_L^2 to a distinct range, $\mu_{L_{max}}^2 > \mu_L^2 > \mu_{L_{min}}^2$.[10] Note that the allowed range for μ_L^2 (in terms of μ_R^2) is only determined by the couplings $g_{L,R}$ and g' and thus independent of the parameters λ and λ_m.

Free and Constrained Parameters in the Left-Right Symmetric Model

The discussed parameter constraints emerging in the left-right symmetric model are summarized in Tab. 4.2. As two of the seven model parameters are dictated by Standard Model values (g_L, g') and three further parameters are restricted by model bounds $\left(\lambda,\, g_R,\, \mu_L^2\right)$, two (completely) free parameters, namely λ_m and μ_R^2, remain. Analogously to the singlet extension of the Standard Model, λ_m will be the crucial parameter to determine the strength of the phase transition and hence the GW amplitude $h_o^2\tilde{\Omega}_{GW}$, while the choice of the dimensionful parameter μ_R^2 will set the temperature scale and subsequently the peak frequency $\tilde{f}$ of the GW spectrum.

---

[10] Setting the upper bound in relation to the lower bound, $\mu_{L_{max}}^2 \geq \mu_{L_{min}}^2$ yields the constraint $3\left(g_R^2 + g_L^2\right) + 4g'^2 \geq 0$ which is automatically fulfilled for $g_{L,R}, g' > 0$.

Furthermore, we will choose the relation between the parameters λ and λ_m (cf. (4.41)), g_R and g_L (cf. (4.43)) as well as μ_L^2 and μ_R^2 (cf. (4.45) and (4.47)) randomly in consistency with the parameter constraints to generate a strongly first-order phase transition. Their relevance for the strength of the phase transition will become evident in the next section. As we will see, the limiting case of these parameter constraints will lead to flat directions of the effective potential.

6.4.3 Flat Directions

Flat directions of the effective potential develop in the particular limiting case where the curves $D_R^2(v_L, T)$ and $D_L^2(v_L, T)$, defined in (4.29) and (4.30), are completely identical and overlie each other [82]. In this case, the curves correspond to flat directions in the effective potential. Hence, the condition for flat directions to arise consists in

$$D_R^2(v_L, T) = D_L^2(v_L, T)\,. \tag{4.48}$$

By inserting (4.29) and (4.30) in this expression and comparing the coefficients of the terms on the left- and right-hand side, we derive the parameter conditions for flat directions of the effective potential. These are

$$\mu_R^2 = \frac{2\lambda}{\lambda_m}\mu_L^2, \quad \lambda = \frac{\lambda_m}{2}, \quad g_R = \sqrt{\frac{1}{3}\left[\frac{2\lambda}{\lambda_m}\left(3g_L^2 + g'^2\right) - g'^2\right]}. \tag{4.49}$$

If we subsequently use the second condition $\lambda = \frac{\lambda_m}{2}$ of (4.49) to simplify the other two equations, the first equation reduces to $\mu_R^2 = \mu_L^2$, while the third one becomes $g_R = g_L$.
As displayed by Tab. 4.2, the parameter constraints however require $\lambda > \frac{\lambda_m}{2}$, $\mu_R^2 > \mu_L^2$ and $g_R > g_L$ so that the above conditions for flat directions correspond to the particular *limiting case* of the parameter constraints, but are excluded per construction of the model.
In the case of flat directions the strength of the phase transition can be significantly enlarged [82]. (This will be explicitly discussed in Sec. 4.6.) Therefore, we will approach close to the flat directions by choosing $\lambda > \frac{\lambda_m}{2}$ randomly in consistency with the parameter constraints. Thus, the constraints $\mu_R^2 > \mu_L^2$ and $g_R > g_L$ will be automatically reproduced correctly from the first and third condition of (4.49) by inserting $\lambda > \frac{\lambda_m}{2}$.

4.5. Gravitational Waves as Cosmological Probes

After having discussed the characteristics of the first-order phase transition in the left-right symmetric model, we are now ready to investigate its cosmological implications. Particularly, we will determine the GW spectrum from bubble collisions, characterized by the parameters $\alpha(T)$ and $\beta(T)$. In contrast to the singlet extension of the Standard Model, it will be possible for the left-right symmetric model to perform the calculation of α and β analytically. This will allow to display explicitly their dependence on the model parameters. At first, we will determine the parameter α.

4.5.1. Analytical Determination of the Parameter α

The parameter $\alpha(T)$ is defined as the ratio of false-vacuum energy density $\epsilon(T)$ to thermal energy density $e(T) = \frac{\pi^2}{30} g_* T^4$ of the symmetric phase (cf. (2.1)),

$$\alpha \equiv \frac{\epsilon(T)}{e(T)}. \tag{4.50}$$

The false-vacuum energy density (cf. (2.4)),

$$\epsilon(T) \equiv \Delta V_{eff}(T) - T \frac{\partial \Delta V_{eff}(T)}{\partial T}, \tag{4.51}$$

in the left-right symmetric model is derived from the potential difference $\Delta V_{eff}(T)$ between the left- and right-handed temperature-dependent minima, given in (4.33), and yields

$$\epsilon(T) = \frac{\lambda}{4\lambda^2 - \lambda_m^2} \left[-3c_1(g)\, T^4 + c_2\!\left(g, \mu^2\right) T^2 + c_3\!\left(\mu^2\right) \right] \tag{4.52}$$

with $c_1(g)$, $c_2\!\left(g, \mu^2\right)$, $c_3\!\left(\mu^2\right)$ given in (4.34). At the critical temperature T_C the false-vacuum energy density equals the latent heat L, defined in (2.6)), since the degeneracy of the minima leads to a vanishing potential difference $\Delta V_{eff}(T_C) = 0$. By inserting (4.52) in (2.6), we derive for the latent heat in the left-right symmetric model the expression

$$\begin{aligned} L &\equiv -T_C \left. \frac{\partial \Delta V_{eff}(T)}{\partial T} \right|_{T=T_C} \\ &= \frac{2\lambda}{4\lambda^2 - \lambda_m^2} \left[-2c_1(g)\, T_C^2 + c_2\!\left(g, \mu^2\right) \right] T_C^2 \\ &= \frac{3}{8} \frac{\lambda}{2\lambda - \lambda_m} \left(g_R^2 - g_L^2 \right) v_C^2 T_C^2, \end{aligned} \tag{4.53}$$

revealing a direct proportionality to the VEV v_C and the critical temperature T_C, $L \propto v_C^2 T_C^2$.

The result for the false-vacuum energy density of (4.52) in general determines the parameter $\alpha \equiv \frac{\epsilon(T)}{e(T)}$ for the left-right symmetric model and will be used for the numerical analysis. However, we can derive a physically more intuitive expression for α by approximating the false-vacuum energy density by the latent heat, $\epsilon(T) \simeq L$. From the resulting equation

$$\alpha(T) = \frac{45}{4\pi^2 g_*} \frac{\lambda}{2\lambda - \lambda_m} \left(g_R^2 - g_L^2 \right) \frac{v_C^2 T_C^2}{T^4}, \tag{4.54}$$

it becomes directly apparent that $\alpha(T_C) \to \infty$ for the limiting case of flat directions where $\lambda = \frac{\lambda_m}{2}$. Hence, by approaching the flat directions in consistency with the parameter constraint $\lambda > \frac{\lambda_m}{2}$, it will be possible to enlarge $\alpha(T)$ significantly. This will be essential with regard the detectability of the GW spectrum, as will be discussed in detail in Sec. 4.5.3.
For the calculation of the gravitational wave spectrum, the parameter $\alpha(T)$ has to evaluated

at the tunneling temperature T_*. Since α is not at all as strongly temperature-dependent as $\frac{\beta}{H_*}$ (what will be confirmed by the numerical analysis in Sec. 4.6), even the approximate evaluation of α at $T \simeq T_C$,

$$\alpha(T_C) = \frac{45}{4\pi^2 g_*} \frac{\lambda}{2\lambda - \lambda_m} \left(g_R^2 - g_L^2\right) \left(\frac{v_C}{T_C}\right)^2 , \tag{4.55}$$

generates suitable results. In this approximation, the relation between the strength of the phase transition $\frac{v_C}{T_C}$ and the parameter α is simply described by the proportionality $\alpha \propto ({v_C}/{T_C})^2$. Hence, stronger phase transitions will lead to larger values of α and hence higher peak amplitudes of the GW spectra. Note that this is generally valid [125, 112].

4.5.2. Analytical Determination of the Parameter β

After having computed the parameter α in the left-right symmetric model in the previous section, we will now calculate β as second parameter characterizing the GW spectrum. According to (2.24), the parameter $\beta(T_*)$ renormalized to the Hubble parameter H_* at the tunneling temperature T_* is given by

$$\begin{aligned}\frac{\beta}{H_*} &\equiv T_* \frac{d}{dT}\left(\frac{S_3(T)}{T}\right)\Bigg|_{T=T_*} \\ &\simeq -280 \frac{T_*}{\Delta V_{eff}(T_*)} \frac{d}{dT}\left(\frac{\Delta V_{eff}(T_*)}{T_*}\right)\Bigg|_{T=T_*}\end{aligned} \tag{4.56}$$

with $S_3(T)$ denoting the three-dimensional Euclidean action for thermal tunneling in thin-wall approximation (cf. (2.23)),

$$S_3(T) = \frac{16\pi S_1(T)^3}{3\left(\Delta V_{eff}(T)\right)^2}, \tag{4.57}$$

and $\Delta V_{eff}(T)$ defined in (4.33)-(4.34). For an analytical determination of $\frac{\beta}{H_*}$, we expand $\Delta V_{eff}(T)$ in a Taylor series about T_C up to the first order (the zeroth order vanishes since $\Delta V_{eff}(T_C) = 0$),

$$\Delta V_{eff}(T) \simeq \frac{\partial \Delta V_{eff}(T)}{\partial T}\Bigg|_{T=T_C} = -\frac{L}{T_C}\left(T - T_C\right), \tag{4.58}$$

containing the latent heat L of (2.6). By inserting this equation in (4.56), we obtain an expression for $\frac{\beta}{H_*}$ which is only dependent on the critical temperature T_C and the tunneling temperature T_*,

$$\frac{\beta}{H_*} = 280 \frac{T_*}{T_C - T_*} = 280 \left(\frac{1}{\delta} - 1\right). \tag{4.59}$$

In the last step, we have rewritten the tunneling temperature as $T_* = T_C\,(1-\delta)$ by introduction of the parameter δ. Since the tunneling temperature is required to be equal to or smaller than the critical temperature, $T_C \geq T_* \geq 0$, the parameter δ is constrained to the range $0 \leq \delta \leq 1$.
Note the approximate expression for $\frac{\beta}{H_*}$ as well as the exact equation in (4.56) with (4.57) become divergent for $T_* = T_C$. Hence, $\frac{\beta}{H_*}$ is strongly temperature-dependent and it will be crucial to determine the tunneling temperature T_*.

Analytical Determination of the Tunneling Temperature

The tunneling temperature T_* can be derived from the three-dimensional Euclidean action. Since the dominant temperature dependency of $S_3(T)$ is contained in the potential difference $\Delta V_{eff}(T_*)$ (causing in particular its divergence at the critical temperature), we approximate (4.57) by use of (4.58) as

$$\begin{aligned} \frac{S_3(T_*)}{T_*} &\simeq \frac{16\pi\, S_1(T_C)^3}{3\,T_C\left(\Delta V_{eff}(T_*)\right)^2} \\ &\simeq \frac{16\pi}{3}\,\frac{S_1(T_C)^3}{L^2}\,\frac{T_C}{(T_* - T_C)^2}, \end{aligned} \tag{4.60}$$

where we have evaluated the one-dimensional Euclidean action at the critical temperature, $S_1(T_*) \simeq S_1(T_C)$, and have divided by T_C instead of T_* on the right-hand side. Relating (4.60) to the general expression $\frac{S_3(T_*)}{T_*} \simeq 140$ (cf. (2.11)) subsequently yields the tunneling temperature,

$$\begin{aligned} T_* &= T_C - \sqrt{\frac{16\pi}{3\cdot 140}\,\frac{T_C\,S_1(T_C)^3}{L^2}} \\ &= T_C\,(1-\delta)\,, \end{aligned} \tag{4.61}$$

where the parameter δ emerges as

$$\delta \equiv \sqrt{\frac{16\pi}{3\cdot 140}\,\frac{S_1(T_C)^3}{T_C\cdot L^2}}. \tag{4.62}$$

To determine the tunneling temperature in terms of the model parameters, it remains to compute the one dimensional Euclidean action $S_1(T_C)$ in the left-right symmetric model.

One-dimensional Euclidean Action. The one-dimensional Euclidean action S_1 in the left-right symmetric model is given by [81]

$$S_1 = \int_{-\infty}^{\infty} d\tau \left[\frac{1}{2}\left(\frac{\partial v_L(\tau)}{\partial\tau}\right)^2 + \frac{1}{2}\left(\frac{\partial v_R(\tau)}{\partial\tau}\right)^2 + V_{eff}(v_L(\tau)\,, v_R(\tau)\,, T)\right] \tag{4.63}$$

with Euclidean time τ and boundary conditions imposed by the phase-transition scenario,

$$\begin{aligned} &v_L(\tau=-\infty)=v_C, \quad v_L(\tau=\infty)=0, \quad \partial_\tau v_L(\tau)\,|_{\tau=\pm\infty}0, \\ &v_R(\tau=-\infty)=0, \quad v_R(\tau=\infty)=v_C, \quad \partial_\tau v_R(\tau)\,|_{\tau=\pm\infty}0. \end{aligned} \tag{4.64}$$

According to Hamilton's principle of least action, the tunneling of the fields $v_{L,R}$ proceeds along the path $\varphi(\tau)$ for which the Euclidean action becomes stationary. If we parametrize the Euclidean action S_1 by the path $\varphi(\tau)$, we can derive the thin-wall approximation from the equation of motion, as explained in Sec. 2.3,

$$S_1 = \int_{-\infty}^{\infty} d\tau \left[\frac{1}{2}\, f(\varphi(\tau)) \left(\frac{\partial\varphi(\tau)}{\partial\tau}\right)^2 + V_{eff}(\varphi(\tau)\,,T)\right] \tag{4.65}$$

$$\simeq \int_{\varphi(-\infty)}^{\varphi(\infty)} d\varphi\, \sqrt{2\, f(\varphi)\; V_{eff}(\varphi,T)}. \tag{4.66}$$

Therein, we have defined the function

$$f(\varphi) \equiv \left(\frac{\partial v_L(\varphi)}{\partial\varphi}\right)^2 + \left(\frac{\partial v_R(\varphi)}{\partial\varphi}\right)^2. \tag{4.67}$$

To compute the Euclidean action S_1 from the above equations, we choose the following ansatz for the parametrization of the tunneling path $\varphi(\tau)$ [81]

$$v_L(\varphi) = v_c\, \cos[\varphi(\tau)]\,, \quad v_R(\varphi) = v_c\, \sin[\varphi(\tau)]\,, \quad \varphi(\tau) = \frac{\pi}{4}\left(1+\tanh\left[\frac{\tau}{d}\right]\right), \tag{4.68}$$

wherein we have normalized the Euclidean time τ to the wall thickness d.. Note that this parametrization fulfills the boundary conditions in (4.64). Besides, the parametric function $f(\varphi)$ becomes constant, $f(\varphi) = v_C^2$.

As the one-dimensional Euclidean action reveals only a slight dependency on the temperature, we will perform the calculation by approximating $S_1(T_*) \simeq S_1(T_C)$. The dependency of the one-dimensional Euclidean action on the temperature is contained in the contribution of the effective potential $V_{eff}(\varphi(\tau)\,,T) \equiv V_{eff}(v_L(\varphi)\,,v_R(\varphi)\,,T)$ (cf. (4.65) and (4.66)). Consequently, we can evaluate the effective potential, given in (4.26), at the critical temperature. At first, we determine the exact solution of the one-dimensional Euclidean action $S_{1,E}(T_C)$ without thin-wall approximation. By inserting the effective potential (4.26) at $T = T_C$ in (4.65) and solving the integral for the parametrization ansatz of (4.68), we obtain the result

$$S_{1,E}(T_C) = N_E\, \sqrt{2\lambda - \lambda_m}\, v_C^3, \tag{4.69}$$

where the constant

$$N_E = \frac{\pi}{4}\sqrt{\frac{\gamma_E - \mathrm{Ci}\,(2\pi) + \ln\,(2\pi)}{12}} \simeq 0.35 \tag{4.70}$$

includes the Euler-Mascheroni constant γ_E and the cosine integral $\mathrm{Ci}\,(x)$. Next, we can analogously determine the one-dimensional Euclidean action in the thin-wall approximation $S_{1,A}(T_C)$ by computing the integral (4.66). The result

$$S_{1,A}(T_C) = N_A \sqrt{2\lambda - \lambda_m}\, v_C^3 \tag{4.71}$$

with constant

$$N_A = \frac{\mathrm{Si}\,(\pi)}{2\sqrt{2}} \simeq 0.65, \tag{4.72}$$

containing the sine integral $\mathrm{Si}\,(x)$, reveals the same functional dependence on the model parameters as the exact solution $S_{1,E}(T_C)$ differing only by a factor $\frac{N_A}{N_E} \simeq 1.85$ of the constant. For the numerical analysis we will therefore use the exact result of (4.69)-(4.70).

The determination of the one-dimensional Euclidean action finally allows to compute the tunneling temperature T_* and the parameter $\beta(T_*)$. After inserting the latent heat L of (4.53) as well as the results of (4.69) and (4.71), respectively, in the definition of the parameter δ in (4.62),

$$\delta \equiv \frac{16}{3} \frac{1}{g_R^2 - g_L^2} \frac{(2\lambda - \lambda_m)^{\frac{7}{4}}}{\lambda} \sqrt{\frac{\pi N_{E,A}^3}{105} \left(\frac{v_C}{T_C}\right)^5}, \tag{4.73}$$

the tunneling temperature (cf. (4.61)) takes the form

$$\begin{aligned} T_* &= T_C\,(1-\delta) \\ &= T_C \left(1 - \frac{16}{3} \frac{1}{g_R^2 - g_L^2} \frac{(2\lambda - \lambda_m)^{\frac{7}{4}}}{\lambda} \sqrt{\frac{\pi N_{E,A}^3}{105} \left(\frac{v_C}{T_C}\right)^5}\right), \end{aligned} \tag{4.74}$$

while the parameter $\beta(T_*)$, according to (4.59), arises as

$$\begin{aligned} \frac{\beta}{H_*} &= 280 \left(\frac{1}{\delta} - 1\right) \\ &= 280 \left(\frac{3}{16} \left(g_R^2 - g_L^2\right) \frac{\lambda}{(2\lambda - \lambda_m)^{\frac{7}{4}}} \sqrt{\frac{1}{\pi} \left(\frac{105}{N_{E,A}}\right)^3 \left(\frac{T_C}{v_C}\right)^5} - 1\right). \end{aligned} \tag{4.75}$$

The strength of the phase transition $\frac{v_C}{T_C}$ is given in (4.37). Note that the parameter δ is directly proportional to the strength of the phase transition, $\delta \propto (v_C/T_C)^{5/2}$. A stronger phase transition will therefore result in an increase of the parameter δ within the range $0 \le \delta \le 1$. This will lead in turn to a decrease of the tunneling temperature T_* as well as of the parameter $\frac{\beta}{H_*}$. Hence, the peak amplitude of the GW spectrum, $h_0^2 \tilde{\Omega}_{GW} \propto (\beta/H_*)^{-1}$, will be enlarged, whereas the peak frequency, $\tilde{f} \propto T_*\,(\beta/H_*)$, will be simultaneously lowered. By this behavior the above equations directly reflect an important generic feature of the GW spectrum arising from phase transitions: In general, stronger phase transitions proceed at smaller peak frequencies due to the decrease of T_* and $\frac{\beta}{H_*}$ [113, 112]. In the next section, we will discuss the consequences of this feature for the detectability of the GW spectrum.

4.5.3. Gravitational Wave Spectrum from Bubble Collisions

After having calculated the parameters α and $\frac{\beta}{H_*}$ at the tunneling temperature T_*, the spectrum of gravitational waves generated by bubble collisions during the first-order phase transition (cf. (2.43)-2.45),

$$h_o^2\Omega_{GW}(f) = h_o^2\tilde{\Omega}_{GW}\,\frac{(a+b)\ \tilde{f}^b\, f^a}{b\,\tilde{f}^{(a+b)} + a\,f^{(a+b)}} \tag{4.76}$$

with

$$h_o^2\tilde{\Omega}_{GW} = 1.29\cdot 10^{-6}\left(\frac{H_*}{\beta}\right)^2\left(\frac{\alpha}{\alpha+1}\right)^2\left(\frac{100}{g_*}\right)^{\frac{1}{3}}, \tag{4.77}$$

$$\tilde{f} = 3.79\cdot 10^{-3}\,\mathrm{mHz}\left(\frac{\beta}{H_*}\right)\left(\frac{T_*}{100\,\mathrm{GeV}}\right)\left(\frac{g_*}{100}\right)^{\frac{1}{6}}, \tag{4.78}$$

is determined. (We will assume the total number of degrees of freedom in the left-right symmetric model to be approximately $g_* \simeq 100$.)

As discussed before, stronger phase transitions generally lead to a decrease of the parameters T_* and $\frac{\beta}{H_*}$ so that the peak frequency $\tilde{f}$ of the GW spectrum (cf. (4.78)) is lowered, whereas the peak amplitude $h_o^2\tilde{\Omega}_{GW}$ (cf. (4.77)) is enlarged. Note that the peak amplitude besides is enhanced by an increase of the parameter α. As discussed in Sec. 2.3, the parameters α and $\frac{\beta}{H_*}$ are correlated by the potential difference ΔV_{eff}. Smaller values of $\frac{\beta}{H_*}$ entail in particular bigger values of α. Besides, the increase of α for stronger phase transitions is in particular revealed by (4.55) where $\alpha \propto (v_C/T_C)^2$.

Based on the considerations in Sec. 2.3, we will therefore require the phase transition in the left-right symmetric model to be *strongly first-order* $\left(\frac{v_C}{T_C} \gtrsim 1\right)$ and to proceed at a *high temperature scale* ($T_{EW} < T_* < T_{GUT}$) for generating a peak amplitude $h_o^2\tilde{\Omega}_{GW}$ and a peak frequency $\tilde{f}$ which both lie in the sensitive range of the GW detectors. In this case, the GW spectrum from the first-order phase transition in the left-right symmetric model will be detectable.

Taking this conditions into account, we will perform a numerical analysis of the GW spectrum in the following section.

4.6. Numerical Analysis

Our intention for the numerical analysis is to investigate whether gravitational waves from the considered first-order phase transition can serve as cosmological probes for the physical properties of the left-right symmetric model. Therefore, we will have to analyze if the parameter space consistent with the constraints in Sec. 4.4.3 allows for detectable gravitational waves.

The necessary condition for the detection is in the first place the overlap of the spectral peak amplitude $h_o^2\tilde{\Omega}_{GW}$ with the sensitivity range of the GW experiments, reaching from

$h_o^2\Omega_{GW} \sim 10^{-6}$ [156] for the ground-based Advanced LIGO detector, to $h_o^2\Omega_{GW} \sim 10^{-11}$ and $h_o^2\Omega_{GW} \sim 10^{-17}$ [113] for the planned spaceborne interferometers LISA and (correlated) BBO, respectively.[11] We will discuss the parametric dependence of the quantities α and $\frac{\beta}{H_*}$ for determining the highest possible peak amplitude $h_o^2\tilde{\Omega}_{GW}$ arising from the first-order phase transition in the left-right symmetric model.

The second condition to be necessarily fulfilled for detectable gravitational waves requires the peak frequency of the GW spectrum to lie in the frequency range accessible by the GW detectors. While the ground-based detectors like LIGO and VIRGO are sensitive in the high frequency region $f \simeq$ few Hz ...few kHz, the sensitivity of the spaceborne interferometers LISA, BBO and DECIGO covers the low-frequency range $f \simeq 10^{-4} \ldots 1\,\text{Hz}$ [156] (cf. Sec. C.1). Since the peak frequency of the GW spectrum (independently of the peak amplitude $h_o^2\tilde{\Omega}_{GW}$) can be shifted to higher or lower frequencies by varying the tunneling temperature, we will determine the temperature scale by the choice of the model parameters with regard to the experimentally accessible frequency region.

4.6.1. Determination of the Parameter Space

To derive an upper bound on the peak amplitude $h_o^2\tilde{\Omega}_{GW}$ of the GW spectrum arising from the first-order phase transition in the left-right symmetric model, we first have to determine the parameter space consistent with the constraints and then have to choose the parameters randomly.

For generating a high spectral peak amplitude, its functional dependence, given in (4.77) requires a large value of α coinciding with a small $\frac{\beta}{H_*}$. As displayed by the derived expression for α of (4.55), and $\frac{\beta}{H_*}$ of (4.75) in the left-right symmetric model, this is directly achieved by requiring a strongly first order phase transition. Note that the contribution of the phase transition strength ($\alpha \propto (v_C/T_C)^2$, $\delta \propto (v_C/T_C)^{5/2}$) dominates the functional dependence of α and $\frac{\beta}{H_*}$ on the model parameters.[12] Thus, we have to choose the values for the parameters in the numerical analysis with regard to the parametric dependence of the strength of the phase transition given in 4.37 as

$$\frac{v_C}{T_C} = \frac{1}{4}\sqrt{\frac{1}{2\lambda + \lambda_m}\left(3\,\frac{g_R^2\mu_L^2 - g_L^2\mu_R^2}{\mu_R^2 - \mu_L^2} - g'^2\right)}. \tag{4.79}$$

Choice of g_R. From the requirement of renormalizability of the theory we are restricted to values < 1 for the couplings. While the parameters g_L and g' are dictated by the Standard Model values, $g_L = 0.64$ and $g' = 0.35$ [58], the parameter g_R is free to choose.

The conception of the left-right symmetric model requires the parameter constraint $g_R > g_L$

---

[11] In Chap. C, we review the different types of GW detectors and compute their sensitivity curves in terms of $h_o^2\tilde{\Omega}_{GW}$, using either the experimental data from the operational detectors or the instrumental design parameters of the planned missions. The values for the best sensitivities of the specific GW detectors are summarized in Tab. C.2.

[12] As will be confirmed by the numerical analysis, the influence of the parameters appearing as prefactors in α and δ is only marginal.

g_R	$\frac{v_C}{T_C}$	$\alpha(T_*)$	$\frac{\beta}{H_*}$	$h_o^2\tilde{\Omega}_{GW}$
1.00	2.17	0.1333	607	$4.52 \cdot 10^{-14}$
0.95	1.95	0.0810	690	$1.42 \cdot 10^{-14}$
0.90	1.73	0.0454	806	$3.49 \cdot 10^{-15}$
0.85	1.48	0.0225	985	$6.02 \cdot 10^{-16}$
0.80	1.21	0.0091	1 312	$5.74 \cdot 10^{-17}$
0.75	0.87	0.0025	2 175	$1.54 \cdot 10^{-18}$
0.70	0.33	0.0001	15 472	$7.69 \cdot 10^{-23}$

Table 4.3: *Dependence of the quantities characterizing the peak amplitude $h_o^2\tilde{\Omega}_{GW}$ on the parameter g_R.* For the numerical calculation we have chosen $\lambda_m = 0.1$, $\lambda = 0.09$, $\mu_R^2 = 10^{16}$, $\mu_L^2 = 0.87 \cdot \mu_R^2$ in consistency with the parameter constraints. In the further analysis we will set $g_R = 0.95$.

(cf. Tab. 4.2), leaving the range $0.64 < g_R < 1$. As revealed by equation (4.79) and in Tab. 4.3, the strength of the phase transition $\frac{v_C}{T_C}$ (and hence the peak amplitude $h_o^2\tilde{\Omega}_{GW}$) is larger for bigger values of g_R. For the further analysis we therefore choose

$$g_R = 0.95. \tag{4.80}$$

Choice of $\boldsymbol{\mu_L^2}$. In Sec. 4.4.2 we have discussed that the dimensionless strength of the phase transition cannot depend on the dimensionful parameter μ_L^2 itself, but only on the ratio between μ_L^2 and μ_R^2 .
The choice of g_R determines the range of μ_L^2 in dependence of μ_R^2 arising from the parameter constraints. By inserting the values for g', g_L and g_R in the lower and the upper bound of in (4.45) and (4.47), respectively, the allowed range for μ_L^2 turns out to be $0.48\,\mu_R^2 < \mu_L^2 < 0.88\,\mu_R^2$. Since the strength of the phase transition strongly increases for enlarging the ratio between μ_L^2 and μ_R^2, as shown in Fig. 4.1, we approach close to the upper bound by setting

$$\mu_L^2 = 0.87\,\mu_R^2. \tag{4.81}$$

Choice of $\boldsymbol{\lambda}$. According to Sec. 4.4.3, the effective potential develops flat directions in the limiting case $\lambda = \frac{\lambda_m}{2}$, raising the strength of the phase transition to $\frac{v_C}{T_C} \to \infty$. To fulfill the parameter constraints, we are however restricted to $\lambda > \frac{\lambda_m}{2}$ in our choice of the relation between λ and λ_m. Thus, a strongly first-order phase transition in consistency with the parameter constraints is achieved if we choose this relation randomly.[13] For the further discussion, we therefore assume

$$\lambda = 0.55\,\lambda_m. \tag{4.82}$$

---

[13] Note that the physical scenario of the phase transition requires the tunneling temperature $T_* = T_C\,(1-\delta)$ of (4.74) to be bigger than the critical temperature T_C. The resulting constraint $\delta \leq 1$ transforms into an upper bound on the relation of $\lambda$and $\lambda_,$, namely $\lambda < 1.40\,\lambda_m$, by inserting the already chosen parameters in (4.73). For approaching the case of flat directions, the upper bound is fulfilled in any case.

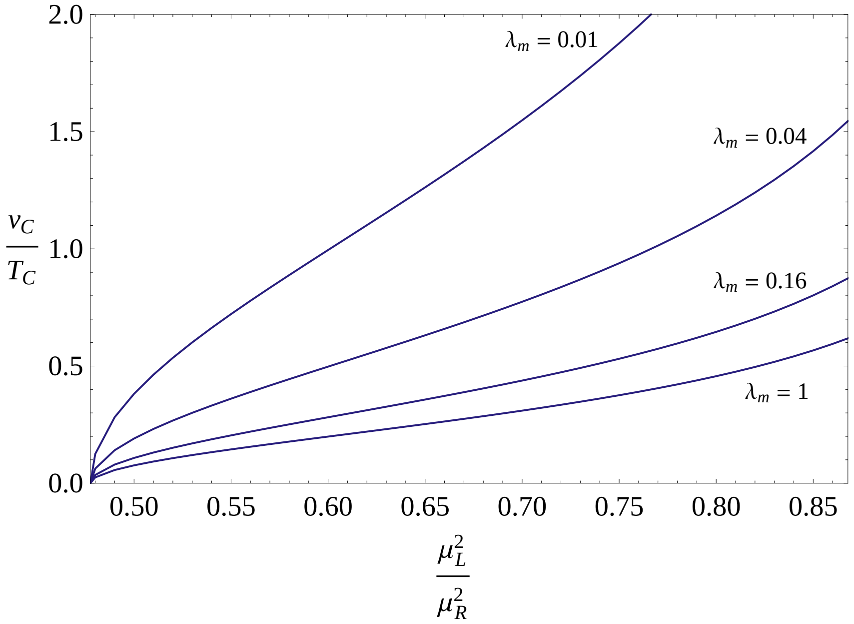

Figure 4.1: *Dependence of the phase transition strength on the ratio of* μ_L^2 *and* μ_R^2 *for different values of* λ_m. Herein, we have assumed the relation $\lambda = 0.9 \cdot \lambda_m$. Note that the lower bound on μ_L^2 leads per construction to a value $v_C = 0$ and hence a vanishing phase transition strength.

Range of λ_m. Apart from μ_R^2, the only remaining undetermined model parameter is λ_m. After having chosen the couplings $g_{L,R}$, g' and set the ratio between μ_L^2 and μ_R^2 as well as λ and λ_m, the value of the strength of the phase transition is only dependent on the choice of λ_m. Although λ_m in principle is a free parameter of the model, the physical properties of the phase transition restrict its choice to a distinct range. On the one hand, the lower bound in this range arises from the condition for a strongly first-order phase transition with $\frac{v_C}{T_C} \lesssim 1$. On the other hand, the phase transition is expected to never be completed for very large values of $\frac{v_C}{T_C}$ [81]. Therefore, we restrict the strength of the phase transition to be $\frac{v_C}{T_C} \lesssim 4$. Transforming these bounds via (4.79) into a range of λ_m reads

$$0.02 \gtrsim \lambda_m \gtrsim 0.38. \tag{4.83}$$

By the determination of the range of λ_m, all necessary parameters for the calculation of the peak amplitude $h_o^2\tilde{\Omega}_{GW}$ of the GW spectrum are set. Since the peak amplitude is higher for stronger phase transitions, the upper bound on λ_m simultaneously yields an upper bound on the order of magnitude of the spectral peak amplitude arising from the considered phase transition in the left-right symmetric model.

In the following section, we will give the results of the numerical analysis for the above choice of parameters by varying λ_m in the range of (4.83) and discuss whether the phase transition provides the possibility of detectable gravitational waves.

$\frac{v_C}{T_C}$	α	$\frac{\beta}{H_*}$	$h_o^2\tilde{\Omega}_{GW}$
3.97	1.79	$1.31 \cdot 10^2$	$3.09 \cdot 10^{-11}$
3.55	0.95	$1.96 \cdot 10^2$	$7.94 \cdot 10^{-12}$
2.75	0.29	$3.76 \cdot 10^2$	$4.52 \cdot 10^{-13}$
1.95	0.08	$7.05 \cdot 10^2$	$1.40 \cdot 10^{-14}$
1.38	0.02	$1.17 \cdot 10^3$	$6.65 \cdot 10^{-16}$
1.04	0.01	$1.69 \cdot 10^3$	$7.12 \cdot 10^{-17}$

Table 4.4: *Results of the numerical analysis for the temperature-scale independent quantities* α, $\frac{\beta}{H_*}$ and $h_o^2\tilde{\Omega}_{GW}$. From the first-order phase transition in the left-right symmetric model we obtain $h_o^2\tilde{\Omega}_{GW} \simeq 3.09 \cdot 10^{-11}$ as upper bound on the peak amplitude of the GW spectrum.

Thereby, we will use the only remaining free parameter μ_R^2 to determine the temperature scale and hence the peak frequency $\tilde{f}$ of the GW spectrum with regard to the detectability.

4.6.2. Detectability of Gravitational Waves

Does the first-order phase transition in the left-right symmetric model give rise to detectable gravitational waves? If yes, at which temperature would the phase transition have to proceed for generating gravitational radiation within the experimentally accessible range?
The first necessary condition for the detectability of the GW spectrum requires the spectral peak amplitude $h_o^2\tilde{\Omega}_{GW}$ to lie in the sensitive region of the GW detectors. To derive an upper bound on the peak amplitude, we perform the numerical analysis for the choice of parameters discussed above by restricting the phase transition strength to the range $1 \lesssim \frac{v_C}{T_C} \lesssim 4$. The results of the numerical analysis for the quantities α, $\frac{\beta}{H_*}$ and $h_o^2\tilde{\Omega}_{GW}$ are listed in Tab. 4.4. From the discussed first-order phase transition in the left-right symmetric model we derive an upper bound on the peak amplitude yielding

$$h_o^2\tilde{\Omega}_{GW_{max}} \simeq 3.09 \cdot 10^{-11}. \tag{4.84}$$

If we compare this bound to the sensitivity range of the ground-based GW detectors GEO600, VIRGO, LIGO, LCGT and the upgraded experiments Advanced VIRGO and Advanced LIGO (cf. Tab. 4.5), it turns out that that the derived value for the peak amplitude is much smaller than the maximal sensitivities achievable by these experiments. In particular, it is six orders of magnitude too small to be detectable by the LCGT/KAGRA detector $\left(h_o^2\Omega_{GW} \sim 10^{-5}\right)$ and still five orders of magnitude smaller than the best sensitivity anticipated for the Advanced LIGO detector $\left(h_o^2\Omega_{GW} \sim 10^{-6}\right)$. Hence, the GW spectrum arising from the first-order phase transition in the left-right symmetric model will not be detectable by the ground-based detectors.[14]

---

[14] Even a detection by the cross-correlated Advanced LIGO (including the last upgrade LIGOIII [108], allowing for a minimal sensitivity of $h_o^2\Omega_{GW} \sim 10^{-10}$ [103]) would be excluded.

Detector	f **[Hz]**	$h_o^2 \Omega_{GW_{max}}$
GEO600 [97]	$1,09 \cdot 10^2$	$9.75 \cdot 10^{-1}$
VIRGO [203]	$4,37 \cdot 10^1$	$2.41 \cdot 10^{-3}$
LIGO [144]	$1,30 \cdot 10^2$	$1.61 \cdot 10^{-3}$
Advanced VIRGO [204]	$4,68 \cdot 10^1$	$1.50 \cdot 10^{-5}$
LCGT / KAGRA [122]	$6,90 \cdot 10^1$	$1.04 \cdot 10^{-5}$
Advanced LIGO [145]	$3,22 \cdot 10^1$	$5.48 \cdot 10^{-6}$

Table 4.5: *Minimal sensitivities of several ground-based GW detectors.* The values for the best sensitivities have been computed from the data which has been taken from the indicated references. This is explained in detail in Sec. C.2. (The maximal sensitivity of the planned Advanced LIGO and LCGT/KAGRA detectors are based on anticipated sensitivity curves.)

Since the sensitivity may change slightly for different data runs and with respect to the current experimental status, these values should serve as rough orientation for the order of magnitude of the sensitivities achievable by the ground-based detectors.

Detector	f **[Hz]**	$h_o^2 \Omega_{GW_{max}}$
LISA	$2,09 \cdot 10^{-3}$	$1.30 \cdot 10^{-11}$
FP-DECIGO	$1,02 \cdot 10^{-1}$	$4.63 \cdot 10^{-13}$
BBO / TDI-DECIGO	$2,35 \cdot 10^{-1}$	$1.13 \cdot 10^{-13}$
Correlated BBO	$2,76 \cdot 10^{-1}$	$8.84 \cdot 10^{-17}$
Ultimate DECIGO	$1,70 \cdot 10^{-1}$	$1.60 \cdot 10^{-17}$

Table 4.6: *Minimal sensitivities of several spaceborne GW detectors.* The values for the best sensitivities for the spaceborne interferometers have been computed from the data of the anticipated sensitivities curves generated by use of [152]. This is explained in detail in Sec. C.2. As before, these values are given to estimate the order of magnitude of the experimentally achievable sensitivities.

This becomes clearly evident in Fig. 4.2, depicting the GW spectra for the sets of model parameters given in Tab. 4.7. For obtaining a peak frequency $\tilde{f}$ of the GW wave spectrum which lies in the frequency range accessible by the ground-based detectors, f = few Hz ...few kHz, we have chosen $\mu_R^2 = 6.02 \cdot 10^{13}\,(\mathrm{GeV})^2$ setting the critical temperature to $T_C = 1.32 \cdot 10^7$ GeV. However, the peak amplitude $h_o^2 \tilde{\Omega}_{GW}$ of the GW spectrum from the left-right symmetric model is several orders of magnitude smaller than the maximal sensitivities of the ground-based GW detectors and hence will not be observable at this temperature scale and in this frequency range, respectively.

Although the experimental observation of the model spectra by the ground-based detectors is excluded, the comparison of Tab. 4.4 with Tab. 4.6 reveals that a detection by the planned spaceborne interferometers LISA, BBO and TDI-/FP-DECIGO, including Ultimate DECIGO and the cross-correlated BBO detector, however will be possible.

Set	α	$\frac{\beta}{H_*}$	$h_o^2\tilde{\Omega}_{GW}$	T_* **[GeV]**	$\tilde{f}$ **[Hz]**
(A1)	1.79	$1.31 \cdot 10^2$	$3.09 \cdot 10^{-11}$	$6.48 \cdot 10^6$	$3.22 \cdot 10^1$
(A2)	0.95	$1.96 \cdot 10^2$	$7.94 \cdot 10^{-12}$	$7.18 \cdot 10^6$	$5.34 \cdot 10^1$
(A3)	0.29	$3.76 \cdot 10^2$	$4.52 \cdot 10^{-13}$	$8.53 \cdot 10^6$	$1.21 \cdot 10^2$
(A4)	0.08	$7.05 \cdot 10^2$	$1.40 \cdot 10^{-14}$	$9.89 \cdot 10^6$	$2.64 \cdot 10^2$
(A5)	0.02	$1.17 \cdot 10^3$	$6.65 \cdot 10^{-16}$	$1.08 \cdot 10^7$	$4.81 \cdot 10^2$
(A6)	0.01	$1.69 \cdot 10^3$	$7.12 \cdot 10^{-17}$	$1.14 \cdot 10^7$	$7.29 \cdot 10^2$

Table 4.7: *Set of parameters corresponding to the GW spectra from the left-right symmetric model which are depicted* Fig. 4.2*.* For generating a model peak frequency $\tilde{f}$ within the frequency range accessible the ground based detectors, we have chosen $\mu_R^2 = 6.02 \cdot 10^{13}$ (GeV)^2 setting the critical temperature to $T_C = 1.32 \cdot 10^7$ GeV.

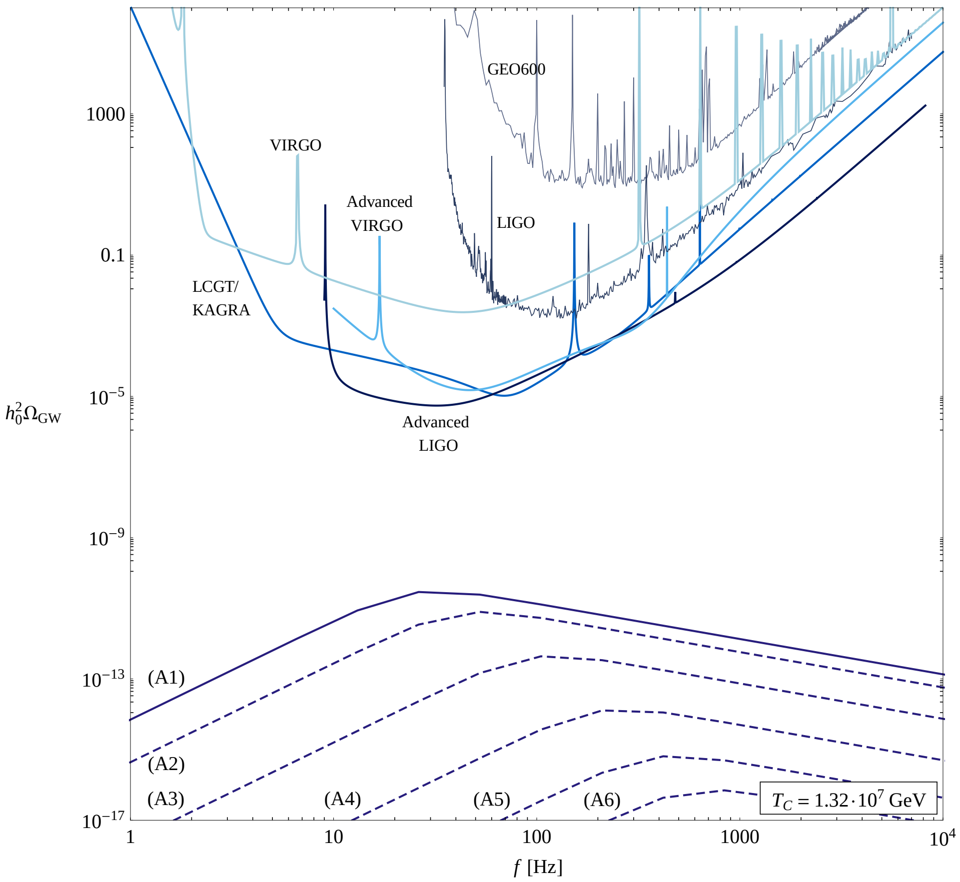

Figure 4.2: *GW spectra from the first-order phase transition in the left-right symmetric model at a critical temperature of* $T_C = 1.32 \cdot 10^7$ GeV *in comparison with the sensitive region of the ground-based GW detectors.* The maximal peak amplitude derived from the first-order phase transition in the left-right symmetric model does not lie in the sensitive region of the ground-based detectors GEO600, VIRGO, LIGO, LCGT / KAGRA and the upgraded experiments Advanced VIRGO and Advanced LIGO. Thus, an experimental detection of the model spectrum by the ground-based detectors is excluded.

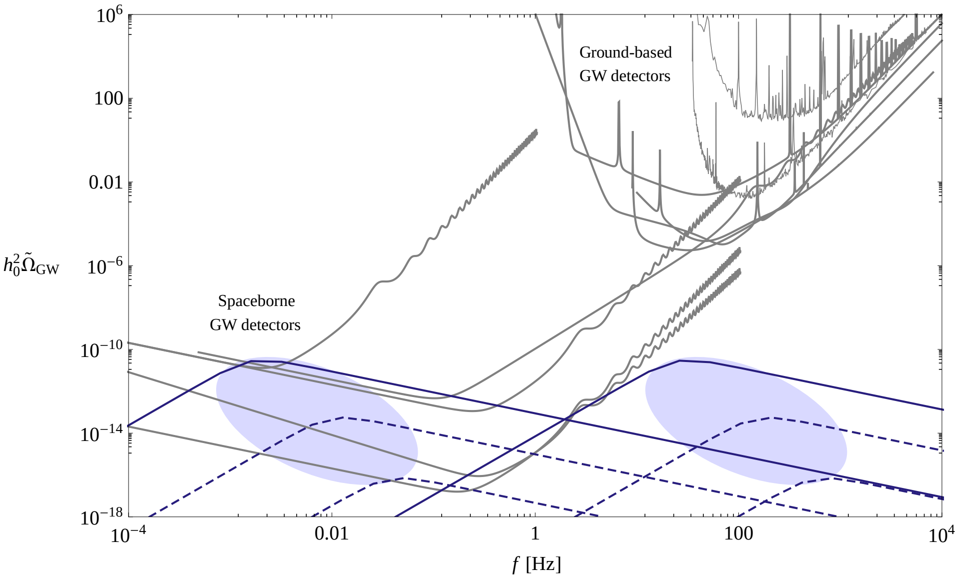

Figure 4.3: *Shift of the GW spectrum to the low-frequency range.* The upper bound on the peak amplitude derived for the left-right symmetric model is too low to allow for detection of the GW spectrum by the ground-based GW detectors, which are sensitive in the frequency range f = few Hz ...few kHz. However, the GW spectrum will be observable by the planned spaceborne detectors in the low-frequency range $f = 10^{-4}\,...\,1\,\text{Hz}$. By demanding the detectability of the GW spectrum, the phase transition is therefore restricted to proceed at a smaller temperature resulting in a shift of the spectral peak frequency to a lower frequency range. The areas of the figure highlighted in blue refer to the range of the peak amplitudes given in Tab. 4.4.

The best sensitivity of the Ultimate DECIGO (cross-correlated BBO) detector, which is of the order $h_o^2\Omega_{GW} \sim 10^{-17}$, will even allow for detection of the GW spectrum (nearly) within the whole parameter range $1 \lesssim \frac{v_C}{T_C} \lesssim 4$. However, in case of really strong phase transitions with $\frac{v_C}{T_C} \gtrsim 3.70$ even a detection with LISA $\left(h_o^2\Omega_{GW} \sim 10^{-11}\right)$ will be achievable.[15]

The second condition for detectability requires the peak frequency $\tilde{f}$ of the GW spectrum to lie in the frequency range accessible by the GW detectors. Since the order of magnitude of the GW spectrum restricts its detectability to the spaceborne detectors, the peak frequency has to be shifted to the low-frequency range $f \simeq 10^{-4}\,...\,1\,\text{Hz}$, as shown in Fig. 4.3.
A shifting to lower frequencies is achieved by restricting the phase transition to proceed at smaller temperatures. If we for instance set the critical temperature to $T_C = 8.56 \cdot 10^2\,\text{GeV}$, by choosing $\mu_R^2 = 2.55 \cdot 10^5\,(\text{GeV})^2$, the maximal peak amplitude arises at a peak frequency

---

[15] For a phase transition strength of $\frac{v_C}{T_C} \simeq 3.70$, the numerical analysis yields a peak amplitude of $h_o^2\tilde{\Omega}_{GW} \simeq 1.30 \cdot 10^{-11}$, which corresponds to the approximated maximal sensitivity $h_o^2\Omega_{GW_{max}}$ of the LISA detector given in Tab. 4.6. For stronger phase transitions with $h_o^2\tilde{\Omega}_{GW_{max}} \gtrsim h_o^2\Omega_{GW_{max}}$ the respective GW spectra will be detectable by LISA.

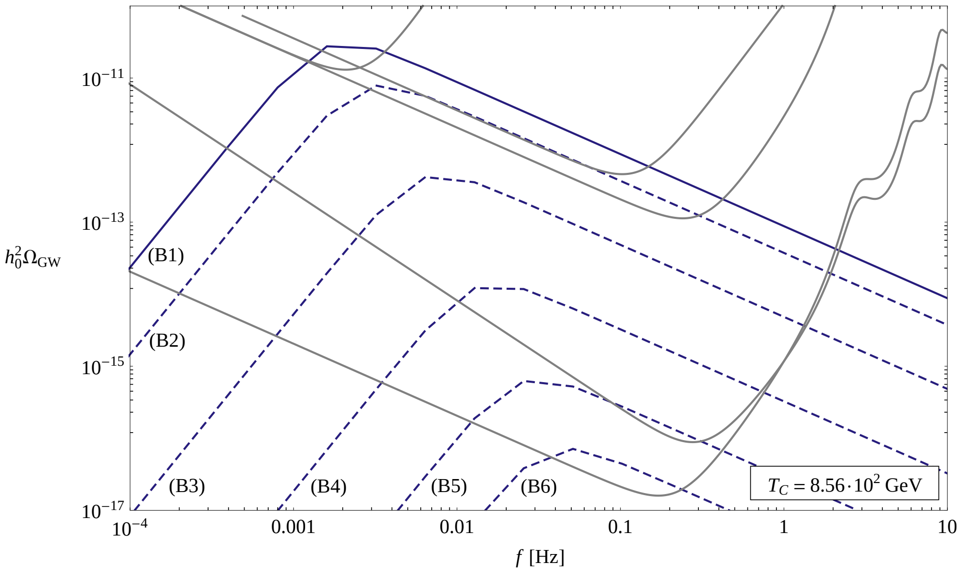

(a) *GW spectra from the left-right symmetric model in comparison with the sensitive region of the spaceborne GW detectors.* At a critical temperature of $T_C = 8.56 \cdot 10^2$ GeV the peak frequency $\tilde{f}$ of the GW spectra lie within the frequency range accessible by the spaceborne interferometers. Since the corresponding peak amplitudes $h_o^2\tilde{\Omega}_{GW}$ additionally are in the sensitive region of these GW detectors, the GW spectrum will be detectable.

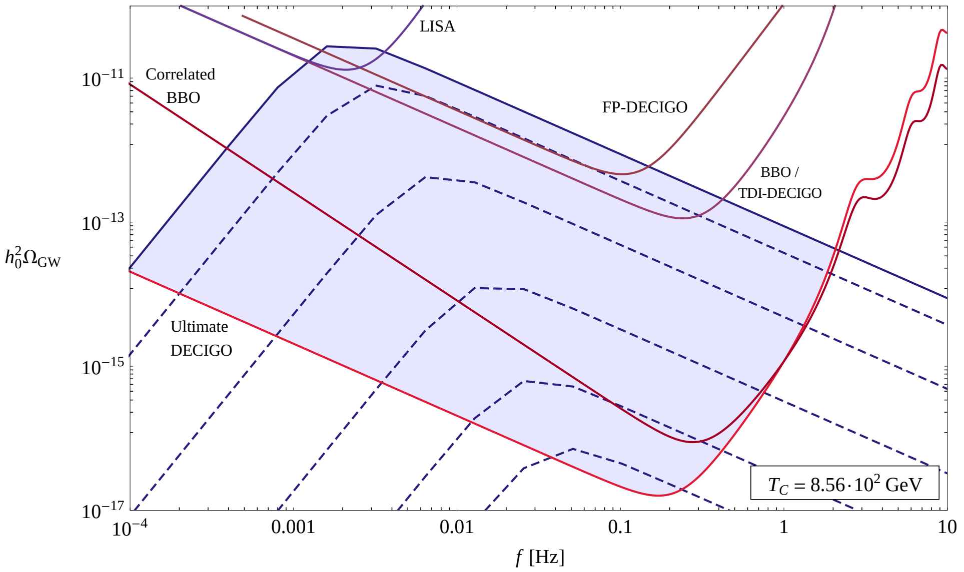

(b) *Detectable region of the GW spectra from the left-right symmetric model.* Within the detectable region, which is highlighted in blue, the model spectra lie in the sensitive region of the GW detectors. The Ultimate DECIGO (cross-correlated BBO detector) allows to detect spectra from (nearly) the whole parameter range, while the detection by LISA is restricted to spectra with peak amplitude $h_o^2\tilde{\Omega}_{GW}$ close to the upper bound.

Figure 4.4: *GW spectra from the first-order phase transition in the left-right symmetric model at a critical temperature of* $T_C = 8.56 \cdot 10^2$ GeV *in comparison with the sensitive region of the spaceborne GW detectors.*

Set	α	$\frac{\beta}{H_*}$	$h_o^2\tilde{\Omega}_{GW}$	T_* **[GeV]**	$\tilde{f}$ **[Hz]**
(B1)	1.79	$1.31 \cdot 10^2$	$3.09 \cdot 10^{-11}$	$4.21 \cdot 10^2$	$2.09 \cdot 10^{-3}$
(B2)	0.95	$1.96 \cdot 10^2$	$7.94 \cdot 10^{-12}$	$4.67 \cdot 10^2$	$3.47 \cdot 10^{-3}$
(B3)	0.29	$3.76 \cdot 10^2$	$4.52 \cdot 10^{-13}$	$5.55 \cdot 10^2$	$7.90 \cdot 10^{-3}$
(B4)	0.08	$7.05 \cdot 10^2$	$1.40 \cdot 10^{-14}$	$6.43 \cdot 10^2$	$1.72 \cdot 10^{-2}$
(B5)	0.02	$1.17 \cdot 10^3$	$6.65 \cdot 10^{-16}$	$7.06 \cdot 10^2$	$3.13 \cdot 10^{-2}$
(B6)	0.01	$1.69 \cdot 10^3$	$7.12 \cdot 10^{-17}$	$7.42 \cdot 10^2$	$4.74 \cdot 10^{-2}$

Table 4.8: *Set of parameters corresponding to the GW spectra from the left-right symmetric model which are depicted* Fig. 4.4. For generating a spectral peak frequency $\tilde{f}$ within the frequency range accessible by the spaceborne detectors, we have chosen $\mu_R^2 = 2.55 \cdot 10^5\,(\text{GeV})^2$ setting the critical temperature to $T_C = 8.56 \cdot 10^2$ GeV.

of $\tilde{f} = 2.09 \cdot 10^{-3}$ Hz and thus will be in particular detectable by LISA. This is illustrated in Fig. 4.4 for the sets of model parameters given in Tab. 4.8. In comparison with Fig. 4.2, the critical temperature in Fig. 4.4 has been lowered by more than four orders of magnitude.

In which temperature range does the phase transition hence have to proceed for providing observable gravitational radiation?
Fig. 4.4 displays that the GW spectrum for peak amplitudes close to the upper bound will even be detectable by the cross-correlated BBO and Ultimate DECIGO detector if the peak frequency reaches the lower frequency limit of 10^{-4} Hz of the experimentally accessible range. However, the numerical analysis yields in this case temperatures of the electroweak scale for the phase transition to proceed. Below 10^{-4} Hz the sensitivity of the spaceborne detectors is expected to drop considerably [113, 112] so that we exclude a detection of gravitational waves at even lower frequencies.
Physically more interesting will be the upper bound on the tunneling temperature derived from the demand of detectability of the GW spectrum. We determine this upper bound on tunneling temperature from the peak frequency $\tilde{f}$ at which the maximal peak amplitude $h_o^2\tilde{\Omega}_{GW_{max}}$ intersects the sensitivity curve $h_o^2\Omega_{GW_{detector}}(f)$ of the Ultimate DECIGO and cross-correlated BBO detectors, i.e. $h_o^2\tilde{\Omega}_{GW_{max}}\left(\tilde{f}\right) = h_o^2\Omega_{GW_{detector}}(f)$ with $\tilde{f} = f$. For Ultimate DECIGO we compute an upper bound on the tunneling temperature of $T_* = 1.73 \cdot 10^6$ GeV $\left(T_C = 2.53 \cdot 10^6 \text{ GeV}\right)$, whereas we obtain for the cross-correlated BBO detector a maximal temperature of $T_* = 2.31 \cdot 10^6$ GeV $\left(T_C = 4.69 \cdot 10^6 \text{ GeV}\right)$. Thus, the GW spectrum from the considered phase transition in the left-right symmetric model will be detectable for tunneling temperatures $T_* \lesssim 10^6$ GeV.

Detectable Range of $\alpha(T_*)$

For determining the upper bound on the tunneling temperature, we have shifted the peak frequency $\tilde{f}$ of the GW spectrum to the upper limit of the detectable frequency range, but have assumed the peak amplitude $h_o^2\tilde{\Omega}_{GW}$ to be maximal and hence constant. Now, we will consider instead a constant tunneling temperature T_* (and hence peak frequency) by varying the peak amplitude. Since the parameters α and $\frac{\beta}{H_*}$ depend on each other (cf. Sec. 2.3), we can numerically determine $\frac{\beta}{H_*}$ in dependency of α for different sets of model parameters. Expressing the results as a function $\frac{\beta(\alpha)}{H_*}$, the GW spectrum (in this model) is only dependent on the parameters α and T_*. For different, but constant values of T_* we can subsequently determine the minimal value of $\alpha(T_*)$ where the peak amplitude of the GW spectrum intersects the sensitivity curve of a specific detector and hence will be detectable. For the computation of $\alpha(T)$ the data of the sensitivity curves for the spaceborne detectors generated by use of [152], on the basis of the input parameters of Tab. C.1 in Chap. C, has been used. The results for minimal values for $\alpha(T_*)$ allowing for detection of the GW spectrum from the phase transition in the left-right symmetric model are summarized in Tab. 4.9, while the corresponding curves $\alpha(T_*)$ are depicted in Fig. 4.5 and Fig. 4.6.. Therein, the dashed lines refer to the uncertainty with respect to the numerically determined relation $\frac{\beta(\alpha)}{H_*}$. For being detectable by LISA, the GW spectrum is required to possess a minimal value $\alpha(T_*) = 1.481$ at $T_* = 3.23 \cdot 10^2$ GeV. Note that this temperature lies slightly above the electroweak scale $\left(T_{EW} \simeq 10^2 \text{ GeV}\right)$ due to the correlation of the parameters α and $\frac{\beta}{H_*}$. In detail, a decrease in the parameter α leads to an enlargement of $\frac{\beta}{H_*}$. This effect, revealed in [103, 113, 112], has already been discussed in Sec. 4.5.3. The optimal tunneling temperature for Ultimate DECIGO, providing a minimal value of $\alpha(T_*) = 0.013$ for the detectability of the GW spectrum, emerges as $T_* = 2.08 \cdot 10^3$ GeV, while a detection by the cross-correlated BBO detector will be possible for at least $\alpha(T_*) = 0.024$ at $T_* = 4.47 \cdot 10^3$ GeV.

Detector	**T_* [GeV]**	**$\alpha(T_*)$**	
LISA	$3.23 \cdot 10^2$	1.481	(cf. Fig. 4.5)
Ultimate DECIGO	$2.08 \cdot 10^3$	0.013	(cf. Fig. 4.6)
Correlated BBO	$4.47 \cdot 10^3$	0.024	(cf. Fig. 4.6)

Table 4.9: *Minimal values of $\alpha(T_*)$ allowing for detection of the GW spectrum from the first-order phase transition in left-right symmetric model for different spaceborne GW detectors.*

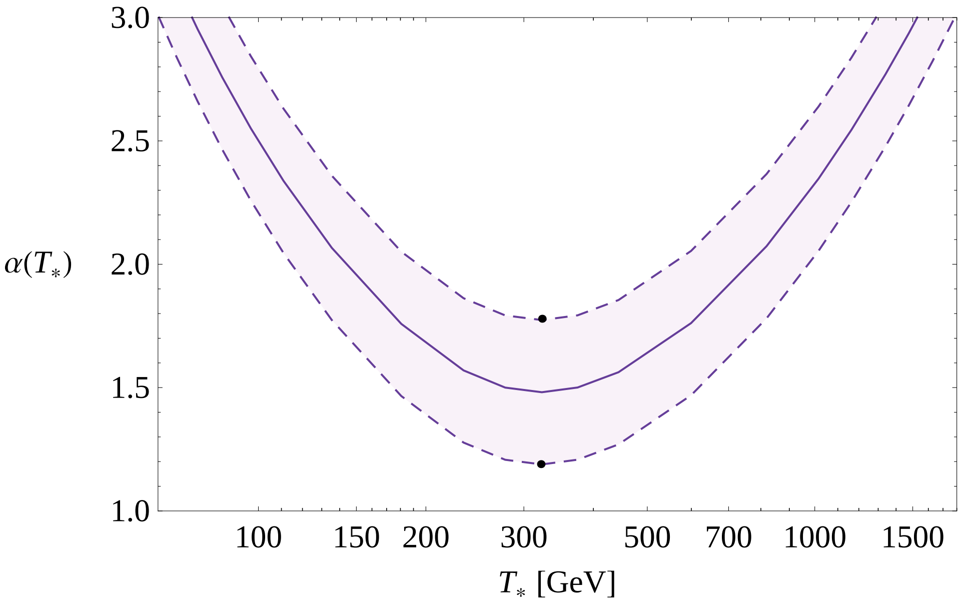

Figure 4.5: *Lower bound on the parameter $\alpha(T_*)$ from the GW spectrum in the left-right symmetric model allowing for detection by the LISA detector.* The minimal values of $\alpha(T_*)$ generating a GW peak amplitude within the experimentally detectable range can be computed from the data of the sensitivity curve (cf. chapter C). The dashed lines refer to the uncertainty with respect to the numerically determined relation $\frac{\beta(\alpha)}{H_*}$.

The sensitivity range of the LISA detector requires a minimal value of $\alpha(T_*) = 1.481$ at a tunneling temperature of $T_* = 3.23 \cdot 10^2$ GeV for the GW spectrum in the left-right symmetric model to be detectable.

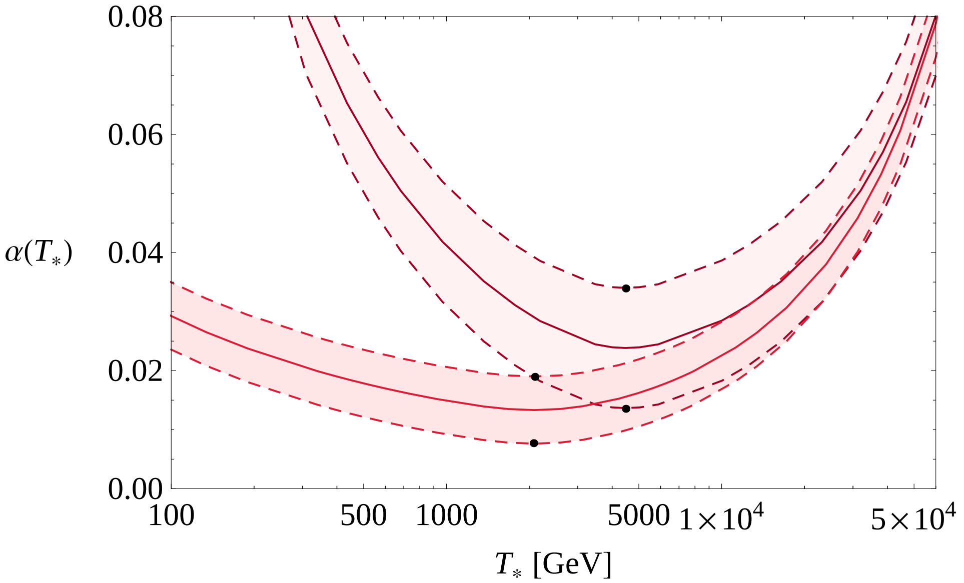

(a) *Lower bound on the parameter $\alpha(T_*)$ in the left-right symmetric allowing for the detection of the GW spectrum by the Ultimate DECIGO and cross-correlated BBO detector.* For being detectable by Ultimate DECIGO, the GW spectrum is required to possess a minimal value of $\alpha(T_*) = 0.013$ at a tunneling temperature of $T_* = 2.08 \cdot 10^3$ GeV (cf. 4.6b), whereas a detection of the GW spectrum by the cross-correlated BBO detector will be possible for a value of at least $\alpha(T_*) = 0.024$ at $T_* = 4.47 \cdot 10^3$ GeV (cf. 4.6c).

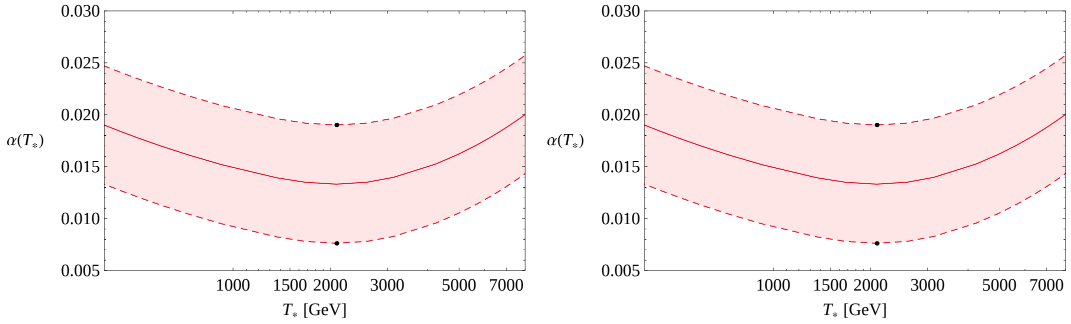

(b) *Lower bound on the parameter $\alpha(T_*)$ in the left-right symmetric allowing for detection of the GW spectrum by Ultimate DECIGO.*

(c) *Lower bound on the parameter $\alpha(T_*)$ in the left-right symmetric allowing for detection for detection of the GW spectrum by the cross-correlated BBO detector.*

Figure 4.6: *Lower bound on the parameter $\alpha(T_*)$ from the GW spectrum in the left-right symmetric model allowing for detection by the Ultimate DECIGO and the cross-correlated BBO detector.* The curve of minimal values for the parameter $\alpha(T_*)$, leading to a GW peak amplitude within the experimentally accessible range, has be computed from the data of the sensitivity curves (cf. Chap. C). The uncertainty with respect to the numerically determined relation $\frac{\beta(\alpha)}{H_*}$ is depicted by dashed lines.

Conclusions

First-order phase transitions constitute one possible source of the stochastic background of cosmological origin. As these relic gravitational waves carry unaltered information from the state of the Universe at the time of their production, they can serve as cosmological probes for new physics at energy scales inaccessible by particle physics experiments. Hence, their detection allows to prove the underlying physical concepts in extensions of the Standard Model. The detection of the stochastic GW background requires a preceding strongly first-order phase transition. Since stronger phase transitions proceed at lower temperatures by creating larger bubbles, they lead to a shift of the spectral peak frequency to frequencies which might lie outside the experimentally accessible frequency region $\left(f \lesssim 10^{-4}\,\mathrm{Hz}\right)$ and therefore does not allow for detection (even in case of sufficient height of the peak amplitude). Therefore, our intention in this thesis was to investigate first-order phase transition in extensions of the Standard Model which are assumed to take place at temperatures between the electroweak and the GUT scale with regard to the possibility of detectable gravitational waves.

First-order phase transitions are characterized by a barrier separating the false from the true vacuum state. The most studied approach is to induce a thermal barrier by the bosonic finite-temperature one-loop contributions in the effective potential. We used these mechanism to investigate the $\mathbb{Z}_2$-symmetry breaking phase transition in the Standard Model extended by a real gauge singlet S. The physical relevance of this model bases on the fact that various extensions of the Standard Model contain elements transforming non-trivially under a hidden sector gauge group, but as singlets in the Standard Model. As the only renormalizable interaction of such scalars with the Standard Model occurs via the Higgs sector, we assumed the additional singlet to couple only to the Higgs field.
To investigate the $\mathbb{Z}_2$-symmetry breaking phase transition we computed the effective potential at finite temperature up to the one-loop order. Thereby, we have in particular taken into account the ring contributions to generate a thermally induced barrier by the cubic contributions in terms of the thermal masses. As the singlet naturally decouples from the low-energy Standard Model sector at temperatures between the electroweak and the GUT scale, where the $\mathbb{Z}_2$-symmetry breaking phase transition is assumed to proceed, we derived a high temperature approximation of the effective potential for the investigation of the phase transition.

For obtaining a physically viable phase transition scenario we imposed constraints on the model parameters restricting the free parameters to μ_S^2 and λ_m. By the choice of μ_S^2 we set the critical temperature of the phase transition to $T_C = 10^5 \ldots 10^7\,\mathrm{GeV}$ and used the parameter λ_m to determine the strength of the phase transition. For generating a strongly first-order phase transition with a strength of at least $\frac{S_C}{T_C} \simeq 1$, the coupling λ_m has to be chosen small. The parameters α and $\frac{\beta}{H_*}$ characterizing the GW spectrum do not merely depend on the phase transition strength, but also incorporate a further dependency on the model parameters (as we have explicitly seen in the case of the left-right symmetric model). Subsequently, the extremely small coupling λ_m leads to values of α significantly smaller than $O(1)$ as required for a detectable signal. As the parameters α and $\frac{\beta}{H_*}$ are correlated via the dependency on the potential difference between the true and the false vacuum state, the parameter $\frac{\beta}{H_*}$ is simultaneously expected to be several magnitudes of order large than the necessary order $O\left(10^2\right)$ for detectable gravitational waves. Hence, the investigated phase transition scenario in the singlet extension of the Standard Model does not provide the possibility of detectable gravitational waves so that its physical conception cannot be probed by gravitational waves. The reason for this is that the thermally induced barrier, which is typically proportional to the couplings of the model, is too small for obtaining a first-order phase transition resulting in detectable gravitational waves.

Due to the smallness of the thermally induced barrier our further motivation was to study a model providing a barrier in the effective potential already at tree-level. Therefore, we investigated the left-right symmetric model being theoretically well motivated and constituting one of the most promising extensions of the Standard Model. Apart from explaining parity violation by including parity as a spontaneous broken symmetry, the left-right symmetric model provides a physical meaning to the $B-L$ quantum number as generator of the $U(1)$ gauge symmetry and incorporates additional sources for viable CP violation. As the model includes right-handed massive gauge bosons escaping experimental detection the $L-R$ symmetry breaking phase transition has to proceed at an energy scale much higher than the electroweak scale. The occurrence of a strongly first-order phase transition, due to the emergence of a barrier in the tree-level potential, which proceeds at temperatures between the electroweak and the GUT scale makes it suitable to be investigated with regard to the detectability of gravitational waves. After the calculation of the effective potential in the mean-field approximation, we derived in particular an analytic expression for the strength of the phase transition influencing the GW spectrum by being incorporated in the parameters α and $\frac{\beta}{H_*}$. As the left-right symmetric model allows for an analytical determination of the parameters α and $\frac{\beta}{H_*}$ as well as the tunneling temperature T_*, we were able to study the functional dependence of these quantities on the model parameters. For determining an upper bound on the GW amplitude we have subsequently chosen the model parameters randomly in consistency with the parameter constraints, but also with regard to the limiting case of flat directions which enhances the phase transition strength significantly. Based on this, we performed a numerical analysis of the GW spectrum for different sets of model parameters. From the first-order phase transition in the left-right symmetric model, we derived an upper bound on the peak amplitude of the GW spectrum yielding $h_o^2\tilde{\Omega}_{GW_{max}} \simeq 3.09 \cdot 10^{-11}$. Although this bound is below the best sensitivity the ground-based detectors such as Advanced VIRGO, LCGT / KAGRA and Advanced LIGO $\left(h_o^2\Omega_{GW} \sim 10^{-5} \ldots 10^{-6}\right)$ and even below the sensitivity range of the cross-correlated Advanced LIGO (LIGOIII) detector $\left(h_o^2\Omega_{GW} \sim 10^{-10}\right)$, a detection of the GW spectrum with the spaceborne interferometers will be possible. For very strongly first-order phase transitions with peak amplitudes close to the upper bound the GW spectrum will be observable by LISA $\left(h_o^2\Omega_{GW} \sim 10^{-11}\right)$. The sensitivity of the Ultimate DECIGO and cross-correlated BBO detector $\left(h_o^2\Omega_{GW} \sim 10^{-16} \ldots 10^{-17}\right)$ even allows a detection of the GW spectrum within the whole parameter range of the model. However, the restriction of the GW spectrum to be detectable only by the spaceborne interferometers imposes an upper bound on the peak frequency and hence on the temperature of the phase transition to proceed. The GW spectrum will be detectable for temperatures below $T_* \lesssim 10^6$ GeV by assuming the parameter $\frac{\beta}{H_*}$ to be close to the lower bound (generating the maximal peak amplitude $h_o^2\tilde{\Omega}_{GW_{max}}$) of the model. Finally, we have determined the minimal values of $\alpha(T_*)$ which are required for a detection of the GW spectrum. Therefore, we have numerically determined the dependency of the parameter $\frac{\beta}{H_*}$ on α for expressing the peak amplitude $h_o^2\tilde{\Omega}_{GW}$ merely as function of α. For a given temperature T_* setting the peak frequency of the spectrum, we computed the minimal value of alpha necessary for a detection of the GW spectrum. Thereby, we related the numerical analysis on the experimental sensitivity curves of the specific detectors. For LISA we derived a lower bound of $\alpha(T_*) = 1.481$ at $T_* = 3.23 \cdot 10^2$ GeV. The value lies slightly above the electroweak scale as the correlation between α and $\frac{\beta}{H_*}$ leads to an enlargement of $\frac{\beta}{H_*}$ by decreasing values of α. For the Ultimate DECIGO detector we obtain a lower bound $\alpha(T_*) = 0.013$ at a temperature $T_* = 2.08 \cdot 10^3$ GeV, while the minimal value $\alpha(T_*) = 0.024$ at $T_* = 4.47 \cdot 10^3$ GeV is needed for a detection with BBO.

Our results are visualized in Fig. 4.2, Fig. 4.4 as well as Fig. 4.6 and 4.6a.

Appendix

Appendix A

Singlet Extension of the Standard Model

A.1. Bosonic Self-Energies in the Infrared Limit

In this chapter of the appendix we will compute the bosonic finite-temperature self-energies (polarization tensors) $\Pi_i\,(h, S, T)$ for the singlet extension of the Standard Model. These are needed to determine the bosonic thermal masses (cf. (3.17))

$$M_i^2(h, S, T) \equiv m_i^2(h, S) + \Pi_i(h, S, T)\,, \tag{A.1}$$

$i = W_{l,t}, Z_{l,t}, \gamma_{l,t}, \chi, h, S$, appearing in the ring-diagram contributions to the effective potential in Sec. 3.2.3.

A.1.1. Finite-Temperature One-Loop Contributions to the Self-Energies

We will compute the self-energies $\Pi_i\,(h, S, T)$ at finite temperature in leading order. The one-loop diagrams contributing to the bosonic self-energies in the singlet model arise from quartic interactions, from interactions with fermion fields (i.e. t-quark fields) and from cubic interactions with the scalars (cf. Fig. A.1). The corresponding one-loop integrals $I_b\big(m_i^2\big)$, $I_f\left(m_i^2\right)$ and $K_b\left(m_i^2, m_j^2\right)$ [200] have to be evaluated at finite temperature. After dimensional regularization their values are given by

$$\begin{aligned} I_b\big(m_i^2\big) &= T\mu^{2\epsilon} \sum_{n=-\infty}^{+\infty} \int \frac{d^{3-2\epsilon}p}{(2\pi)^{3-2\epsilon}} \frac{1}{\omega_{b_n}^2 + \omega^2} \\ &\simeq -\frac{T}{4\pi}\, m(h, S) + \frac{T^2}{12} - \frac{1}{16\pi^2}\left[\frac{1}{\epsilon} + \gamma_E - \log\left(\frac{4\pi T^2}{\mu^2}\right)\right] m_i^2\,, \end{aligned} \tag{A.2}$$

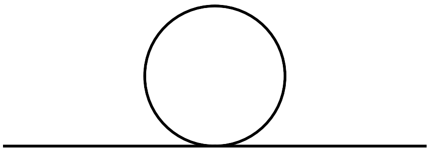

(a) *Quartic interactions.*

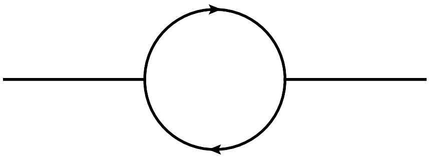

(b) *Interactions with fermion fields.*

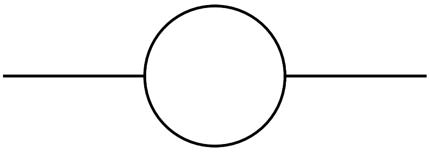

(c) *Cubic interactions with scalars.*

Figure A.1: *One-loop contributions to the bosonic self-energies in the singlet extension of the Standard Model.* In the above diagrams the solid external lines are assumed to represent scalar and gauge-boson fields.

$$\begin{aligned} I_f\left(m_i^2\right) &= T\mu^{2\epsilon} \sum_{n=-\infty}^{+\infty} \int \frac{d^{3-2\epsilon}p}{(2\pi)^{3-2\epsilon}} \frac{1}{\omega_{f_n}^2 + \omega^2} \\ &\simeq -\frac{T^2}{24} - \frac{1}{16\pi^2}\left[\frac{1}{\epsilon} + \gamma_E - \log\left(\frac{4\pi T^2}{\mu^2}\right)\right] m_i^2, \end{aligned} \tag{A.3}$$

$$\begin{aligned} K_b\left(m_i^2, m_j^2\right) &= T\mu^{2\epsilon} \sum_{n=-\infty}^{+\infty} \int \frac{d^{3-2\epsilon}p}{(2\pi)^{3-2\epsilon}} \frac{1}{\left[\omega_{b_n}^2 + \vec{p}^2 + m_i^2\right]\left[\left(\vec{p} - \vec{p_j}\right)^2 + \omega_{b_n}^2 + m_j^2\right]} \\ &= -\int_0^1 dx \, \frac{\partial I_b(\alpha(x))}{\partial \alpha(x)}; \quad \alpha(x) \equiv -x\,(x+1)\,p_j^2 + (1-x)\,m_i^2 + x\,m_j^2 \\ &\simeq -\frac{T^2}{8\pi} \int_0^1 \frac{dx}{\sqrt{\alpha\,(x)}} - \frac{1}{16\pi^2}\left[\frac{1}{\epsilon} + \gamma_E - \log\left(\frac{4\pi T^2}{\mu^2}\right)\right] \end{aligned} \tag{A.4}$$

with mass scale μ and $\omega^2 \equiv \vec{p}^2 + m^2(h, S)$. The bosonic and fermionic Matsubara frequencies ω_{b_b} and ω_{f_n} are defined in (1.31) and (1.32), respectively. Since the dominant contributions of the integrals (A.2) and (A.3) to the self-energies at high temperatures emerge from the terms $\propto T^2$, we will neglect the other terms (and in particular the terms arising from (A.4)) in the computation of the self-energies.

A.1.2. Self-Energies $\Pi_i\,(h, S, T)$

For the computation of the self-energies the integral contributions have to be multiplied by the corresponding couplings and the appropriate combinatorial and symmetry factors of the Feynman diagrams. Apart from the Standard Model couplings of the gauge-boson and fermion fields to the Higgs (and Goldstone) fields and the Higgs field self-couplings [51], the additional couplings arising in the singlet extended model from the singlet self-interactions and the Higgs-singlet interactions are provided by the tree-level potential in Sec. 3.1.

Self-Energies of the Scalar Fields. The self-energy $\Pi_{SS}\,(h, S, T)$, constituting the thermal correction to the pure singlet mass matrix element $m^2_{SS}\,(h, S)$ (cf. (3.22)), arises for instance as the sum of the self-energy contributions from the singlet self-interaction as well as the singlet interactions with the Higgs and Goldstone fields,

$$\begin{aligned}\Pi_{SS}\,(h, S, T) &\simeq 3\lambda_S\; I_b\!\left(m^2_{SS}\right) + \frac{\lambda_m}{2}\, I_b\!\left(m^2_{hh}\right) + 3\cdot\frac{\lambda_m}{2}\, I_b\!\left(m^2_{\chi}\right)\\ &\simeq (3\lambda_S + 2\lambda_m)\,\frac{T^2}{12}\\ &= \left(\frac{\lambda_S}{4} + \frac{\lambda_m}{6}\right)T^2.\end{aligned} \tag{A.5}$$

Analogously, we can compute the further scalar self-energies leading to the results

$$\begin{aligned}\Pi_{SS} &= \left(\frac{\lambda_S}{4} + \frac{\lambda_m}{6}\right)T^2,\\ \Pi_{hh} &= \Pi_{\chi} = \left(\frac{\lambda_h}{2} + \frac{\lambda_m}{24} + \frac{3g^2 + g'^2}{16} + \frac{y_t^2}{4}\right)T^2,\\ \Pi_{hS} &= \Pi_{Sh} \simeq 0,\end{aligned} \tag{A.6}$$

Self-Energies of the Gauge-Boson Fields. Next we will derive the self-energies of the gauge-boson sector. Therefore, we write the gauge-boson polarization tensor Π^{AB}_{gb} of the original (Standard Model) $SU(2)_L$ and $U(1)_Y$ gauge fields A^a_μ and B_μ (cf. Sec. 3.1) in matrix form. In the IR limit only the longitudinal components of the gauge bosons receive a thermal mass correction from the self-energy contributions in the polarization tensor [53]. The polarization tensor reduces in this limit to a diagonal matrix

$$\Pi^{AB}_{gb} = \begin{pmatrix} \Pi_{A^1_\mu} & 0 & 0 & 0\\ 0 & \Pi_{A^2_\mu} & 0 & 0\\ 0 & 0 & \Pi_{A^3_\mu} & 0\\ 0 & 0 & 0 & \Pi_{B_\mu}\end{pmatrix}, \tag{A.7}$$

whose elements contain the self-energies of the gauge fields A^a_μ and B_μ. Analogously to the previous computations, these are computed arise as the sum of the self-energy contributions from the gauge-boson fields, the Higgs fields and the t-quark fields yielding

$$\Pi_{A^a_\mu} = \frac{11}{6} g^2 T^2, \quad \Pi_{B_\mu} = \frac{11}{6} g'^2 T^2. \tag{A.8}$$

To obtain the self-energies in the basis of the mass eigenstates, i.e. the *physical* gauge-boson fields $W^\pm_\mu$, Z_μ and A_μ, we have to diagonalize the thermal mass matrix $\mathcal{M}^2_{gb}(h,T) \equiv \mathcal{M}^2_{gb}(h) + \Pi^{AB}_{gb}(h,T)$ containing the zero-temperature (Standard Model) mass matrix of the gauge-boson fields A^a_μ and B_μ

$$\mathcal{M}^2_{gb}(h) = \frac{h^2}{4} \begin{pmatrix} g^2 & 0 & 0 & 0 \\ 0 & g^2 & 0 & 0 \\ 0 & 0 & g^2 & -gg' \\ 0 & 0 & -gg' & g'^2 \end{pmatrix}. \tag{A.9}$$

In the charged gauge-boson sector, where the physical gauge-boson fields are per convention defined as $W^\pm_\mu \equiv \frac{1}{\sqrt{2}}\left(A^1_\mu \pm iA^2_\mu\right)$, the thermal mass matrix appears already in diagonal from. This allows to directly read off the corresponding thermal masses $M^2_{W_l}(h,T)$. The self-energies equal in particular

$$\Pi_{W_l} = \frac{11}{6} g^2 T^2. \tag{A.10}$$

Since the thermal mass matrix in the neutral gauge-boson sector however possesses off-diagonal elements, it has to be diagonalized by an orthogonal rotation matrix $\mathcal{R}$ connecting the neutral gauge-boson fields $\left(A^0_\mu, B_\mu\right)$ to the physical fields $\left(Z_\mu, A_\mu\right)$ corresponding to the mass eigenstates of the neutral gauge-bosons Z and γ [25, 85]. After diagonalizing the respective thermal masses arise as eigenvalues (diagonal elements) of the thermal mass matrix. Since these can be written as

$$\begin{aligned} M^2_{Z_l}(h,T) &= m^2_Z(h) - m^2_W(h) + \frac{11}{6} g'^2 T^2, \\ M^2_{\gamma_l}(h,T) &= m^2_W(h) + \frac{11}{6} g^2 T^2, \end{aligned} \tag{A.11}$$

we can identify the self-energies as thermal corrections to the field-dependent masses[1]

$$\begin{aligned} \Pi_{Z_l} &= -m^2_W(h) + \frac{11}{6} g'^2 T^2, \\ \Pi_{\gamma_l} &= m^2_W(h) + \frac{11}{6} g^2 T^2. \end{aligned} \tag{A.12}$$

Due to $m^2_\gamma(h) = 0$, the only contribution of the photon to the ring-diagram correction in the effective potential arises from the non-vanishing self-energy in the thermal mass.

---

[1] Note that our results for the self-energies Π_{W_l}, Π_{Z_l} and Π_{γ_l} are consistent with those in [72]. The deviation of the prefactors is only caused by the different definitions of the (zero-temperature) Higgs VEVs (cf. Sec.3.3.3).

Appendix B

Left-Right Symmetric Model

B.1. Gauge-Boson Masses

In this chapter of the appendix we compute the masses of the gauge bosons $W^{\pm}_{L,R}$ and $Z_{L,R}$ in the left-right symmetric model.

The masses of the *physical* gauge-boson fields correspond to the eigenvalues of the mass matrices derived from the covariant derivatives in the Higgs-field contribution to the Lagrangian. Hence, the latter will be the starting point for our calculations.

Gauge-Boson Mass Matrices

The Higgs sector of the Lagrangian, as defined in (4.8), is given by

$$\begin{aligned} \mathcal{L}_H =& \mathrm{Tr}\left[\left(D_\mu\Phi\right)^\dagger \left(D^\mu\Phi\right)\right] + \mathrm{Tr}\left[\left(D_\mu\Delta_L\right)^\dagger \left(D^\mu\Delta_L\right)\right] + \mathrm{Tr}\left[\left(D_\mu\Delta_R\right)^\dagger \left(D^\mu\Delta_R\right)\right] \\ & - V_0(\Phi, \Delta_L, \Delta_R)\,, \end{aligned} \tag{B.1}$$

Therein, the covariant derivatives of the bidoublet and triplet fields Φ, Δ_L and Δ_R (cf. (4.9)),

$$\begin{aligned} D_\mu\Phi &\equiv \partial_\mu\Phi + i\frac{g}{2}\left(\sigma_a W^a_{L\mu}\,\Phi - \Phi\,\sigma_a W^a_{L\mu}\right), \\ D_\mu\Delta_L &\equiv \partial_\mu\Delta_L + i\frac{g_L}{2}\left(\sigma_a W^a_{L\mu}\,\Delta_L - \Delta_L\,\sigma_a W^a_{L\mu}\right) + i\frac{g'}{2}\,B_\mu\Delta_L, \\ D_\mu\Delta_R &\equiv \partial_\mu\Delta_R + i\frac{g_R}{2}\left(\sigma_a W^a_{R\mu}\,\Delta_R - \Delta_R\,\sigma_a W^a_{R\mu}\right) + i\frac{g'}{2}\,B_\mu\Delta_R, \end{aligned} \tag{B.2}$$

consist of a kinetic term ($\partial_\mu\Phi$, $\partial_\mu\Delta_L$ and $\partial_\mu\Delta_R$, respectively) complemented by a gauge-invariance preserving term which will provide the gauge-boson masses.

Substituting the Higgs sector VEVs of (4.14),

$$\langle\Phi\rangle = \begin{pmatrix} k_1 & 0 \\ 0 & k_2 \end{pmatrix},\ \langle\Delta_L\rangle = \begin{pmatrix} 0 & 0 \\ v_L & 0 \end{pmatrix},\ \langle\Delta_L\rangle = \begin{pmatrix} 0 & 0 \\ v_R & 0 \end{pmatrix}, \tag{B.3}$$

for the scalar fields in (B.2) and inserting this in (B.1) generates the gauge-boson mass terms $\mathcal{L}_m$ in the Higgs-sector Lagrangian

$$\begin{aligned}\mathcal{L}_H \ni \mathcal{L}_m =& \frac{g_L^2}{4}\left(k_1^2+k_2^2\right)\left[\left(W_{\mu L}^1\right)^2+\left(W_{\mu L}^2\right)^2+\left(W_{\mu L}^3\right)^2\right] \\ &+\frac{g_R^2}{4}\left(k_1^2+k_2^2\right)\left[\left(W_{\mu R}^1\right)^2+\left(W_{\mu R}^2\right)^2+\left(W_{\mu R}^3\right)^2\right] \\ &+\frac{g_L^2}{4}v_L^2\left[\left(W_{\mu L}^1\right)^2+\left(W_{\mu L}^2\right)^2\right]+\frac{v_L^2}{4}\left(g_L\,W_{\mu L}^3-g'\,B_\mu\right)^2 \\ &+\frac{g_R^2}{4}v_R^2\left[\left(W_{\mu R}^1\right)^2+\left(W_{\mu R}^2\right)^2\right]+\frac{v_R^2}{4}\left(g_R\,W_{\mu R}^3-g'\,B_\mu\right)^2 .\end{aligned} \tag{B.4}$$

The above equation can be separated into two parts, providing the mass terms for the charged and neutral gauge-bosons, respectively

$$\mathcal{L}_m = \mathcal{L}_{m,c} + \mathcal{L}_{m,n}. \tag{B.5}$$

Charged Gauge-Boson Sector. By defining the *physical* charged gauge-boson fields per convention as $W_{\mu L,R}^{\pm} \equiv \frac{1}{\sqrt{2}}\left(W_{\mu L,R}^1 \mp W_{\mu L,R}^2\right)$ (equivalently to the Standard Model), we can write the part of the Lagrangian containing the mass terms for the charged gauge-bosons in the form

$$\mathcal{L}_{m,c} = \left(W_{\mu L}^+,\ W_{\mu R}^+\right)\mathcal{M}_c^2\left(v_L, v_R\right)\begin{pmatrix} W_{\mu L}^- \\ W_{\mu R}^- \end{pmatrix}, \tag{B.6}$$

and derive the elements of the charged gauge-boson mass matrix $\mathcal{M}_c^2\left(v_L, v_R\right)$ from (B.4)

$$\mathcal{M}_c^2\left(v_L, v_R\right) = \frac{1}{4}\begin{pmatrix} g_L^2\left(k_1^2+k_2^2+v_L^2\right) & -2g_L g_R\,k_1 k_2 \\ -2g_L g_R\,k_1 k_2 & g_R^2\left(k_1^2+k_2^2+v_R^2\right)\end{pmatrix}. \tag{B.7}$$

Since the (squared) gauge-boson masses correspond to the eigenvalues of the mass matrix in the basis of the mass eigenstates (the physical gauge-boson fields), they can be obtained by diagonalizing the mass matrix and reading off the diagonal elements.
However, the neglection of the Higgs-bidoublet contributions k_1,k_2, as motivated in (Sec. 4.3), already reduces the mass matrix of (B.7) to a diagonal matrix,

$$\mathcal{M}_c^2\left(v_L, v_R\right) = \frac{1}{4}\begin{pmatrix} g_L^2\,v_L^2 & 0 \\ 0 & g_R^2\,v_R^2\end{pmatrix}, \tag{B.8}$$

so that the masses of the charged gauge-bosons $W_{L,R}^{\pm}$ directly arise as

$$m_{W_L}^2\left(v_L\right) = \frac{g_L^2}{4}v_L^2, \quad m_{W_R}^2\left(v_R\right) = \frac{g_R^2}{4}v_R^2. \tag{B.9}$$

Neutral Gauge-Boson Sector. For computing the neutral gauge-boson masses, we derive from (B.4) and(B.5) the Lagrangian containing the corresponding mass terms,

$$\mathcal{L}_{m,n} = \frac{1}{2}\left(W^3_{\mu L},\, W^3_{\mu R},\, B_\mu\right) \mathcal{M}^2_n\left(v_L, v_R\right) \begin{pmatrix} W^3_{\mu L} \\ W^3_{\mu R} \\ B_\mu \end{pmatrix}, \tag{B.10}$$

where the neutral gauge-boson mass matrix $\mathcal{M}^2_c\left(v_L, v_R\right)$ emerges as

$$\mathcal{M}^2_n\left(v_L, v_R\right) = \frac{1}{4}\begin{pmatrix} g_L^2\left(k_1^2+k_2^2+v_L^2\right) & -g_L g_R\left(k_1^2+k_2^2\right) & -g_L g'\, v_L^2 \\ -g_L g_R\left(k_1^2+k_2^2\right) & g_R^2\left(k_1^2+k_2^2+v_R^2\right) & -g_R g'\, v_R^2 \\ -g_L g'\, v_L^2 & -g_R g'\, v_R^2 & g'\,\left(v_L^2+v_R^2\right) \end{pmatrix}. \tag{B.11}$$

Despite the neglection of the Higgs-bidoublet VEVs, leading to

$$\mathcal{M}^2_n\left(v_L, v_R\right) = \frac{1}{4}\begin{pmatrix} g_L^2\, v_L^2 & 0 & -g_L g'\, v_L^2 \\ 0 & g_R^2\, v_R^2 & -g_R g'\, v_R^2 \\ -g_L g'\, v_L^2 & -g_R g'\, v_R^2 & g'\,\left(v_L^2+v_R^2\right) \end{pmatrix}, \tag{B.12}$$

the neutral gauge-boson mass matrix possesses off-diagonal terms so that a mixing between the gauge boson fields $W^3_{\mu L}$, $W^3_{\mu R}$ and B_μ of the neutral sector occurs, in contrary to the charged gauge-boson sector (cf. (B.8)).
To obtain the physical masses of the neutral gauge bosons, the mass matrix $\mathcal{M}^2_n\left(v_L, v_R\right)$ has to be diagonalized (as in the Standard-Model case) by an orthogonal rotation matrix $\mathcal{R}$ connecting the neutral weak fields $\left(W^3_{\mu L},\, W^3_{\mu R},\, B_\mu\right)$ to the corresponding physical fields $\left(Z_{\mu L},\, Z_{\mu R},\, A_\mu\right)$ of the neutral weak sector. The calculation yields the following results for the neutral gauge-boson masses[1]

$$\begin{aligned} m^2_{Z_{L,R}}(v_L, v_R) &= \frac{1}{8}\Big\{\left(g_L^2+g'^2\right) v_L^2 + \left(g_R^2+g'^2\right) v_R^2 \\ &\qquad \mp \sqrt{\left[\left(g_L^2+g'^2\right) v_L^2 - \left(g_R^2+g'^2\right) v_R^2\right]^2 + 4g'^4\, v_L^2 v_R^2}\Big\}, \\ m^2_\gamma(v_L, v_R) &= 0. \end{aligned} \tag{B.13}$$

Note that the photon γ remains massless in the left-right symmetric model like in the Standard Model as well and consequently does not appear in the mass-dependent thermal one-loop correction of (4.18) and (4.23), respectively. Additionally, by setting either v_L or v_R to zero, the $Z_{L,R}$-boson mass equation takes an analogous form as in the Standard Model, $m^2_{Z_{L,R}}\left(v_{L,R}\right) = \frac{g^2_{L,R}+g'}{4}\, v^2_{L,R}$.
Finally, the Lagrangian $\mathcal{L}_m$ of (B.4) in terms of the physical gauge-boson fields and masses reads

$$\begin{aligned} \mathcal{L}_m =& m^2_{W_L}(v_L)\; W_L^{\mu+} W^-_{\mu L} + m^2_{W_R}(v_R)\; W_R^{\mu+} W^-_{\mu R} \\ &+ \frac{1}{2} m^2_{Z_L}(v_L, v_R)\; Z_L^{\mu+} Z^-_{\mu L} + \frac{1}{2} m^2_{Z_L}(v_L, v_R)\; Z_R^{\mu+} Z^-_{\mu R}. \end{aligned} \tag{B.14}$$

---

[1] From our calculation for $m^2_{Z_{L,R}}\left(v_L, v_R\right)$ we reobtain exactly the result of [58], when assuming $g_L \equiv g_R \equiv g$ and $g \gg g'$.

Appendix C

Sensitivity Curves of the Gravitational Wave Detectors

Current and future GW experiments aim to search for gravitational waves of astrophysical and cosmological origin. The searches mainly focus on gravitational waves from coalescing binary systems (cf. for instance [21, 2, 5]), continuous gravitational waves sources (e.g., rotating neutron stars) [4], GW bursts [20, 3] as well as (stochastic) GW backgrounds [44, 6]. Phase transitions in the early evolution of the Universe constitute a possible production mechanism for stochastic GW backgrounds of cosmological origin. Among the different types of GW detectors (for instance cryogenic resonant bars [173]), the GW interferometers possess a frequency range suitable for the detection of gravitational waves of cosmological origin [156].

In this appendix we will briefly review the different classes of interferometric gravitational-wave detectors. Afterwards, we will generate the sensitivity curves or different GW detectors in terms of the strain sensitivity $\tilde{h}_f(f)$ and the normalized GW energy density $h_o^2\Omega_{GW}(f)$ by use of the experimental data.

C.1. Interferometric Gravitational Wave Detectors

C.1.1. Ground-Based Interferometers

In general, two classes of interferometric gravitational-wave detectors exists. The first generation of interferometers comprises ground-based detectors of large scale as for instance the currently operational "Laser Interferometer Gravitational-Wave Observatory" (LIGO) [8, 7] with arms of 4000 m length or the comparable VIRGO detector [52, 9] possessing an arm length of 4000 m. An important improvement of the sensitivity has been and will be achieved by the upgraded experiments Advanced VIRGO [204] (operational) and Advanced LIGO [108] (planned).

The GEO600 detector [154, 155] (600 m arm length) is marginally smaller than LIGO and VIRGO, but uses advanced techniques (as narrow-banding [156]) which will be important for the future generations of detectors. Currently still under construction is the Japanese LCGT detector [141, 24, 140, 192] (renamed as KAGRA due to its location at Kamioka), whereas the so-called "Einstein Telescope" (ET) [80, 109, 185] is proposed as detector of the third generation.
The ground-based detectors are sensitive in the frequency range [156]

$$f \simeq \text{few Hz} \ldots \text{ few kHz}. \tag{C.1}$$

While the upper bound on the frequency is set by the domination of the laser shot (position) noise, the lower bound arises from the seismic noise level. For covering the low-frequency range, which is inaccessible on Earth due to the seismic noise, future GW detectors will therefore operate as spaceborne interferometers.

C.1.2. Spaceborne Interferometers

The future spaceborne interferometers will be sensitive in the frequency range [156]

$$f \simeq 10^{-4} \ldots 1\,\text{Hz}. \tag{C.2}$$

The first proposed cornerstone mission, the "Laser Interferometer Space Antenna" (LISA) [67, 68, 69, 22, 153],will be a detector with three arms of $5 \cdot 10^9$ m length in a respective angle of 60°, can be thought of as two interferometers sharing a common arm. As planned follow-on mission of the LISA detector, the "Big Bang Observer" (BBO) [107, 139] and the Japanese DECIGO detector [127, 128] have been proposed. In addition to LISA, BBO and the original DECIGO detector, which will implement the so-called time-delay interferometry (TDI), a Fabry-Pérot (FP) type spaceborne interferometer [139], adopting the same technique as used by the ground-based interferometers, named FP-DECIGO, has been suggested. (To distinguish between the two types of DECIGO detectors, we will refer to the original DECIGO detector as TDI-DECIGO). As an observational limitation we will consider the Ultimate DECIGO detector which is conceptionally similar to TDI-DECIGO, but whose sensitivity is assumed to be only limited by quantum noises.
The instrumental design parameters for the different spaceborne interferometers are listed in Tab. C.1.

C.2. Sensitivity Curves

C.2.1. Strain Sensitivity $\tilde{h}_f(f)$

The experimental sensitivity of the GW detector is expressed in terms of the strain sensitivity $\tilde{h}_f(f)$ which is linear in the noise density and has dimension $\left[\tilde{h}_f\right] = 1/\sqrt{\text{Hz}}$. The strain sensitivity is defined as [156]

$$\tilde{h}_f(f) \equiv \sqrt{S_n(f)}, \tag{C.3}$$

Parameter		**LISA [152]**	**BBO [106, 107]**	**TDI-DECIGO [14]**	**FP-DECIGO [13]**	**Ultimate DECIGO [14]**
Arm Length	$L\,[\mathrm{m}]$	$5 \cdot 10^{9}$	$5 \cdot 10^{7}$	$5 \cdot 10^{7}$	10^{6}	$5 \cdot 10^{7}$
Arm Angle	$\alpha\,[°]$	60	60	60	60	60
Telescope Diameter	$D\,[\mathrm{m}]$	0.3	2.5	1	1	1
Laser Wavelength	$\lambda\,[\mathrm{nm}]$	1064	355	532	532	532
Laser Power	$P\,[\mathrm{W}]$	1	300	10	10	10
Optical Efficiency	ϵ	0.3	0.3	0.3	0.3	0.3
Acceleration Noise	$\sqrt{S_{acc}}\left[\frac{\mathrm{m}}{\mathrm{s}^2\sqrt{Hz}}\right]$	$3 \cdot 10^{-15}$	$3 \cdot 10^{-17}$	$3.9 \cdot 10^{-17}$ [139]	$7.9 \cdot 10^{-17}$ [139]	$3 \cdot 10^{-19}$ [139]
Position Noise	$\sqrt{S_{pos}}\left[\frac{\mathrm{m}}{\sqrt{Hz}}\right]$	$2 \cdot 10^{-11}$	$1.5 \cdot 10^{-17}$	$1.2 \cdot 10^{-16}$ [139]	$2.2 \cdot 10^{-18}$ [139]	$3 \cdot 10^{-19}$ [139]

Table C.1: *Instrumental Parameters for the Spaceborne Interferometers.* The design parameters for the space interferometers are taken from the respective references given in the headline of the table, if not marked otherwise. They are used as input for the generation of the sensitivity curves by using [152]. Note that the mission design of BBO includes different variants of instrumental parameters and hence the sensitivity may change slightly in the final design.

where $S_n(f)$ denotes the square spectral noise density. A significant reduction of the overall sensitivity is achieved by cross-correlating the signals of several separated detectors [139]. The cross-correlation strain sensitivity for a two-detector constellation is given by [14]

$$\tilde{h}_{f,cross}(f) \simeq \overline{SNR}^{2} \frac{\tilde{h}_f}{(2T\Delta f)^{\frac{1}{4}}}. \tag{C.4}$$

Therein, $\overline{SNR}$ corresponds to the signal-to-noise ratio of the stochastic GW background over the frequency range $f + \Delta f$ and T denotes the observation time. We have explicitly computed the strain sensitivity $\tilde{h}_{f,cross}(f)$ for a cross-correlated BBO constellation. According to [156], we have assumed for the BBO detector a frequency resolution $\Delta f = \frac{f}{10}$ and have chosen $\overline{SNR} = 1$, $T = 1\,\mathrm{yr}$.

where $\overline{SNR}$ is the signal-to-noise ratio of the stochastic gravitational wave background over the frequency range $f + \Delta f$ and T is the observation time. According to [156], we assume for the BBO detector a frequency resolution $\Delta f = \frac{f}{10}$ and $\overline{SNR} = 1$, $T = 1\,\mathrm{yr}$.

For generating the sensitivity curves in terms of the strain sensitivity $\tilde{h}_f(f)$ for the ground-based interferometers, we have taken the experimental data [144, 203, 204, 97] of LIGO,

Detector	f **[Hz]**	$\tilde{h}_f\ \left[\frac{1}{\sqrt{Hz}}\right]$	$h_o^2\Omega_{GW_{max}}$
LISA	$2,09 \cdot 10^{-3}$	$2.06 \cdot 10^{-20}$	$1.30 \cdot 10^{-11}$
FP-DECIGO	$1,02 \cdot 10^{-1}$	$1.14 \cdot 10^{-23}$	$4.63 \cdot 10^{-13}$
BBO / TDI-DECIGO	$2,35 \cdot 10^{-1}$	$1.62 \cdot 10^{-24}$	$1.13 \cdot 10^{-13}$
Correlated BBO	$2,76 \cdot 10^{-1}$	$3.55 \cdot 10^{-26}$	$8.84 \cdot 10^{-17}$
Ultimate DECIGO	$1,70 \cdot 10^{-1}$	$3.12 \cdot 10^{-26}$	$1.60 \cdot 10^{-17}$
GEO600 [97]	$1,09 \cdot 10^{2}$	$1.73 \cdot 10^{-21}$	$9.75 \cdot 10^{-1}$
VIRGO [203]	$4,37 \cdot 10^{1}$	$1.08 \cdot 10^{-22}$	$2.41 \cdot 10^{-3}$
LIGO [144]	$1,30 \cdot 10^{2}$	$1.71 \cdot 10^{-23}$	$1.61 \cdot 10^{-3}$
Advanced VIRGO [204]	$4,68 \cdot 10^{1}$	$7.66 \cdot 10^{-24}$	$1.50 \cdot 10^{-5}$
LCGT / KAGRA [122]	$6,90 \cdot 10^{1}$	$3.56 \cdot 10^{-24}$	$1.04 \cdot 10^{-5}$
Advanced LIGO [145]	$3,22 \cdot 10^{1}$	$8.10 \cdot 10^{-24}$	$5.48 \cdot 10^{-6}$

Table C.2: *Minimal sensitivities of different GW detectors read off from the experimental data.* The points of best strain sensitivity $\tilde{h}_f$ from the experimental data were used to compute the sensitivity $h_o^2\Omega_{GW}$ via (C.6). For the ground-based interferometers the sources of experimental data are indicated, while the data of the anticipated sensitivity curves for the spaceborne interferometers has been generated by use of [152] on the basis of Tab. C.1.

The sensitivities may change slightly for different data runs and with respect to the current experimental status. Therefore, these values should be considered as rough orientation for the order of magnitude of the achievable sensitivity. We refer to these figures in the numerical analysis of Sec. 4.6.

VIRGO, Advanced VIRGO and GEO600 as well as the data [145, 122] anticipating the sensitivity curves of the Advanced LIGO upgrade and the LCGT / KAGRA detector.

Besides, we have taken the instrumental parameters of Tab. C.1 as input to generate data of anticipated sensitivities for the future spaceborne interferometers LISA, BBO, TDI- / FP-DECIGO and Ultimate DECIGO by using [152]. Thereof, we have computed in particular the sensitivity $\tilde{h}_{f,cross}(f)$ via (C.4) for the cross-correlated BBO detector.

The resulting strain-sensitivity curves are depicted in Fig. C.1, Fig. C.2 and Fig. C.3.

C.2.2. Sensitivity $h_o^2\Omega_{GW}(f)$

A stochastic GW background of cosmological origin is usually characterized by the (normalized) energy density per unit logarithmic frequency interval, $h_o^2\Omega_{GW}(f)$. In particular, we express the GW spectra arising from cosmological phase transitions as functions $h_o^2\Omega_{GW}(f)$. For a comparison of the GW spectra with the experimentally accessible sensitivity range it is therefore necessary covert the strain sensitivity $\tilde{h}_f(f)$ into the dimensionless quantity $h_o^2\Omega_{GW}(f)$.

A stochastic GW background will manifest itself in a GW detector as an excess in noise.

Hence it will be observable at a frequency f if spectral GW density $S_h(f)$ exceeds the spectral noise density $S_n(f)$, $S_h(f) > \frac{1}{F} S_n(f)$, where F is the angular efficiency factor F of the GW detector. Inserting this equation in the relation [156]

$$h_o^2 \Omega_{GW}(f) = \frac{4\pi^2}{3H_o^2} \, f^3 S_h(f) \tag{C.5}$$

and expressing the Hubble parameter as $H_0 = h_0 \cdot 100 \, \frac{\mathrm{km}}{\mathrm{s \cdot Mpc}}$, we can derive a minimal detectable value for the detectable energy density,[1]

$$h_o^2 \Omega_{GW}^{min}(f) \simeq \frac{1}{F} \cdot 10^{-2} \left(\frac{f}{100\,\mathrm{Hz}} \right)^3 \left(\frac{\tilde{h}_f}{10^{-22}\,(1/\sqrt{Hz})} \right). \tag{C.6}$$

(We will refer to the energy density of the GW detectors simply as sensitivity.) The angular efficiency factor for interferometric GW detectors is given by

$$F = \frac{2}{5} \, \sin^2(\alpha) \tag{C.7}$$

with α denoting the angle between the interferometer arms. For the ground-based interferometers LIGO, VIRGO, GEO600 and LCGT / KAGRA $\alpha = 90°$, yielding an efficiency factor of $F = \frac{2}{5}$. The arms of the spaceborne interferometers LISA, BBO and DECIGO comprise an angle of $\alpha = 60°$ (cf. Tab. C.1) so that $F = \frac{3}{10}$.

We have used (C.6) to convert the experimental data (cf. Sec. C.2.1), given in terms of the strain sensitivity $\tilde{h}_f(f)$, into values of energy density, $h_o^2 \Omega_{GW}(f)$. From the data, we have determined the best sensitivities, i.e. the minimal values of $\tilde{h}_f$ and $h_o^2 \Omega_{GW}$, achievable by the different GW detectors. The results are listed in Tab. C.2. For the ground-based detectors we obtain a minimal sensitivity of $h_o^2 \Omega_{GW} \sim 10^{-6}$ achievable by the advanced LIGO detector, while the best sensitivities for the spaceborne interferometers reach from $h_o^2 \Omega_{GW} \sim 10^{-11}$ for LISA up to $h_o^2 \Omega_{GW} \sim 10^{-17}$ for the Ultimate DECIGO and cross-correlated BBO detector. The orders of magnitude of these bound equal the values given in [113, 112] and are used in the numerical analysis of Sec. 4.6.
Besides, we have generated the energy-density sensitivity curves $h_o^2 \Omega_{GW}(f)$ for the ground-based and spaceborne interferometric GW detectors. These are depicted in Fig. C.4, Fig. C.5 and Fig. C.6.

---

[1] Note that the relation between the energy density and the strain sensitivity incorporates a factor $\propto f^3$. Thus, the values of energy density for the spaceborne interferometers, which are sensitive in the low-frequency region, are several orders of magnitude smaller in comparison with those of the high-frequency ground-based detectors.

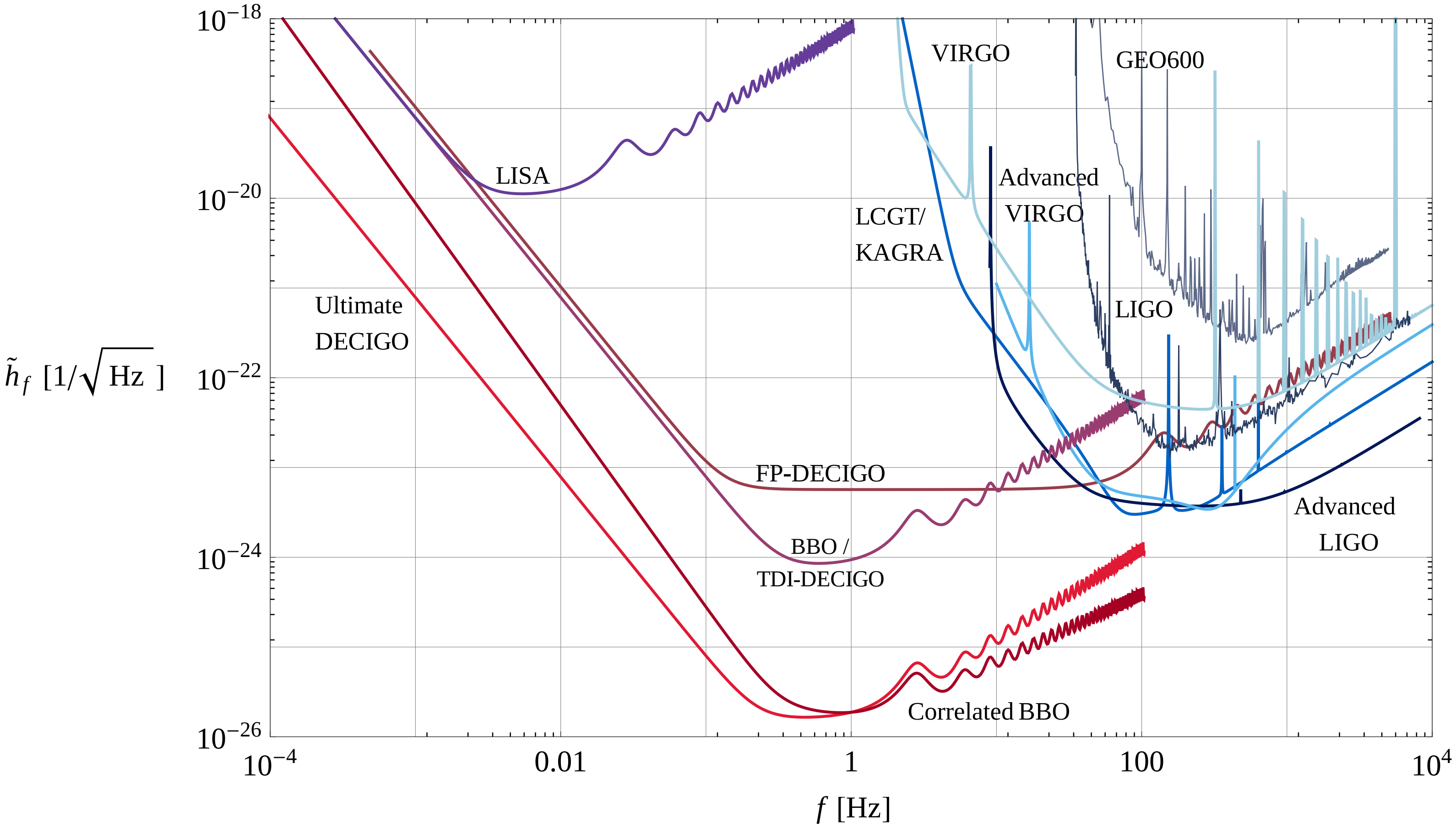

Figure C.1: *Strain-sensitivity curves $\tilde{h}_f(f)$ for different ground-based and spaceborne interferometric GW detectors.* The spaceborne interferometers LISA, BBO, TDI- / FP-DECIGO, Ultimate DECIGO and the cross-correlated BBO detector are sensitive in the low-frenquency range, while the ground based interferometers LIGO, VIRGO, GEO600, LCGT / KAGRA, Advanced LIGO and Advanced VIRGO cover the higher frequency range.

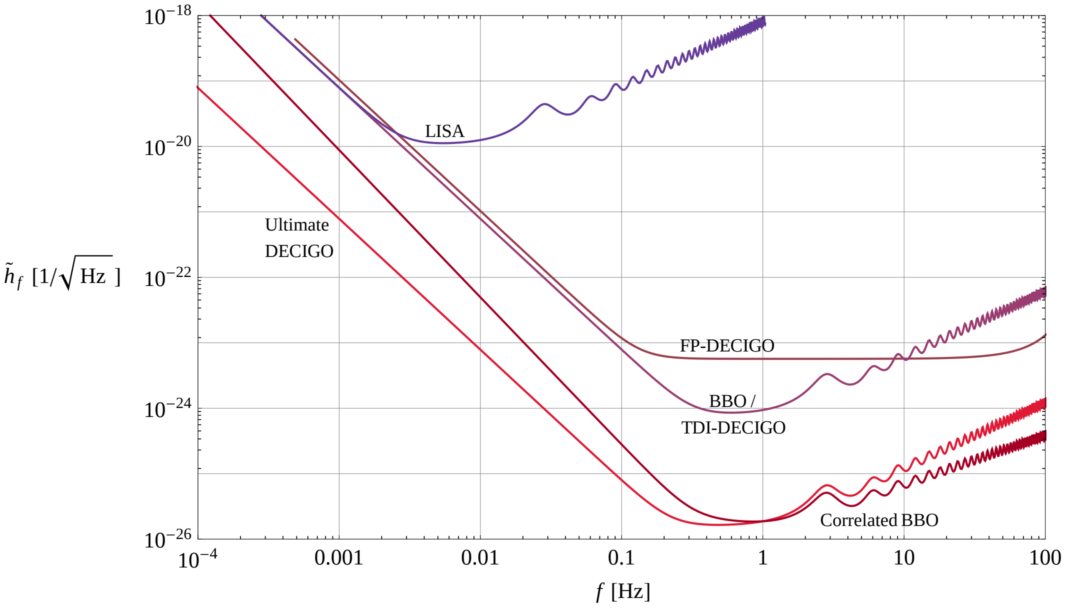

Figure C.2: *Strain-sensitivity curves $\tilde{h}_f(f)$ for the spaceborne interferometric GW detectors LISA, BBO, TDI- / FP-DECIGO, Ultimate DECIGO and the cross-correlated BBO detector.*

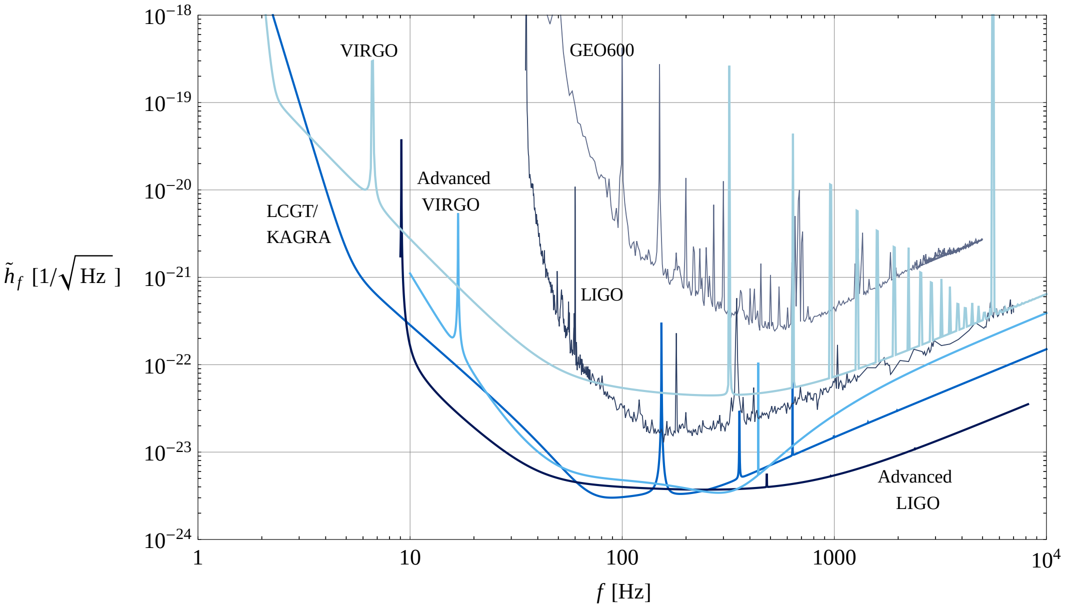

Figure C.3: *Strain-sensitivity curves $\tilde{h}_f(f)$ for the ground-based interferometric GW detectors LIGO, VIRGO, GEO600, LCGT / KAGRA, Advanced LIGO and Advanced VIRGO.*

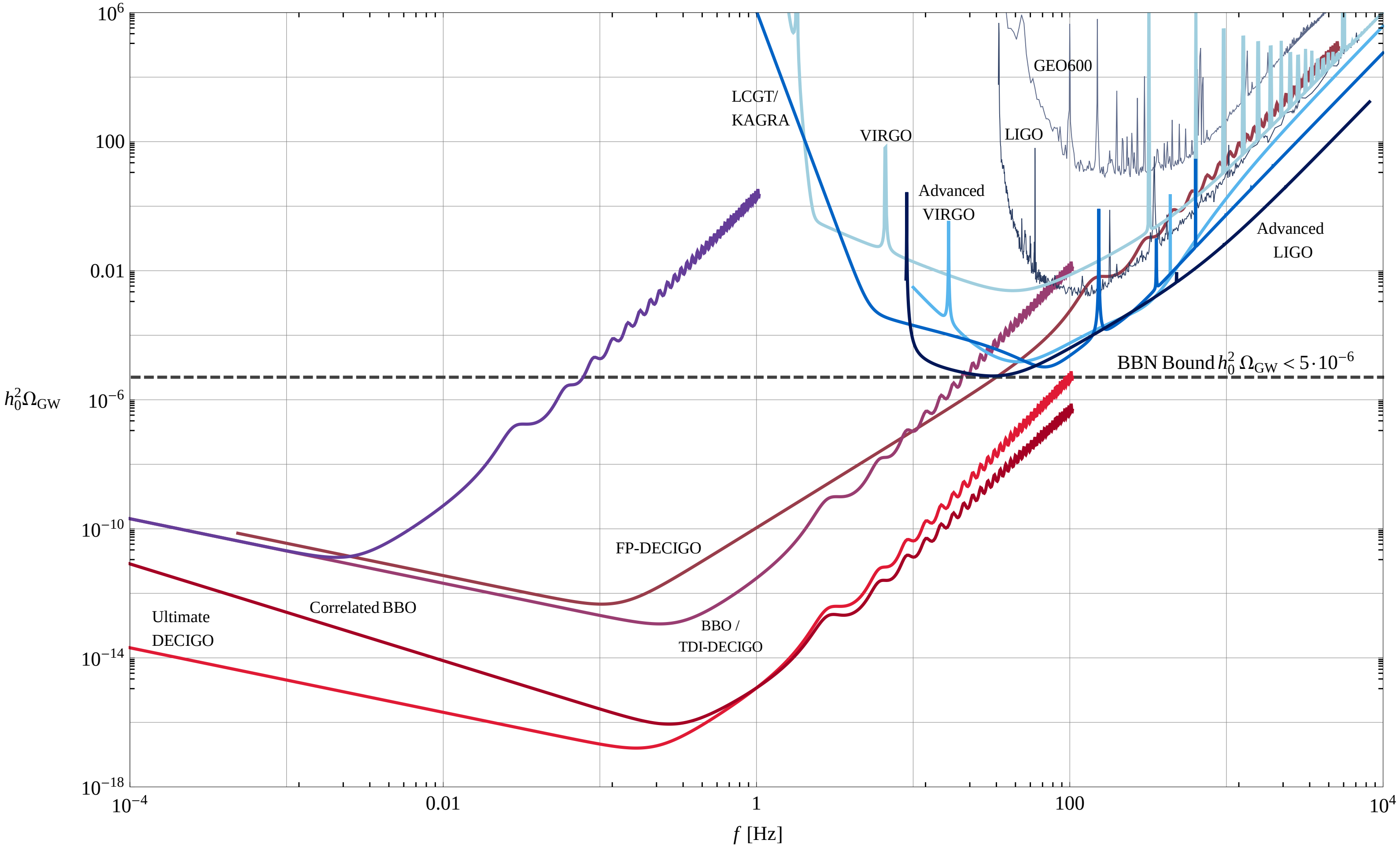

Figure C.4: *Sensitivity curves $h_o^2\Omega_{GW}(f)$ for different ground-based and spaceborne interferometric GW detectors.* The best sensitivities of the spaceborne interferometers lie in the range between $h_o^2\Omega_{GW}(f) \sim 10^{-11}$ (LISA) and $h_o^2\Omega_{GW}(f) \sim 10^{-17}$ (correlated BBO, Ultimate DECIGO), wheras the ground based interferometers only allow for sensitivities as low as $h_o^2\Omega_{GW}(f) \sim 10^{-6}$ (Advanced LIGO), which are comparable to the order of magnitude of the Big Bang nucleosynthesis (BBN) bound $h_o^2\Omega_{GW}(f) < 5 \cdot 10^6$ [156].

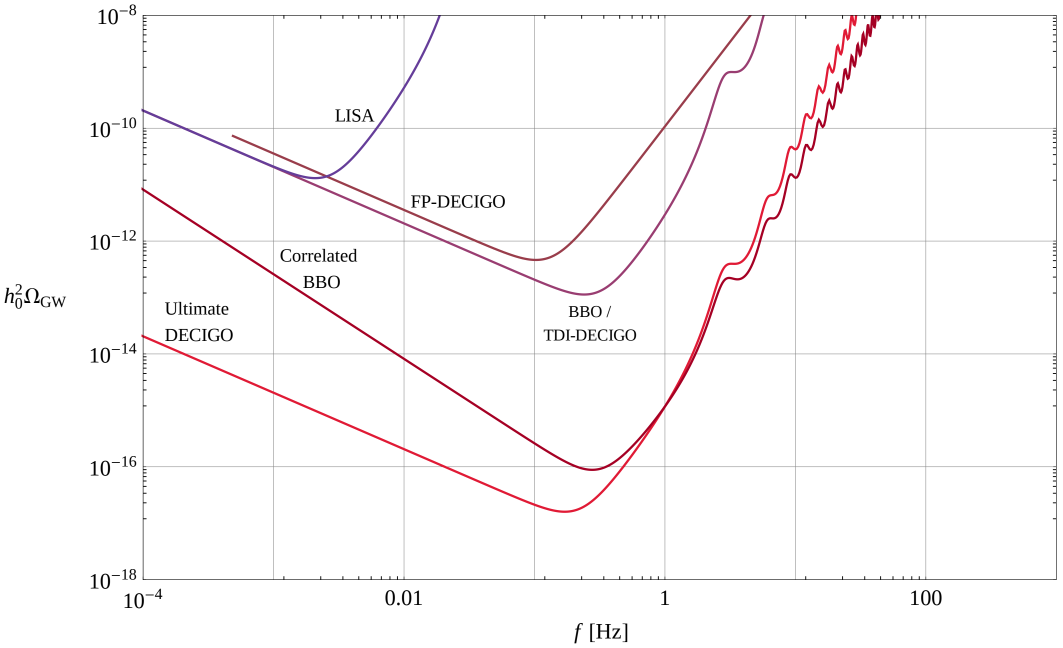

Figure C.5: *Sensitivity curves $h_o^2\Omega_{GW}(f)$ for the spaceborne interferometric GW detectors LISA, BBO, TDI- / FP-DECIGO, Ultimate DECIGO and the cross-correlated BBO detector.*

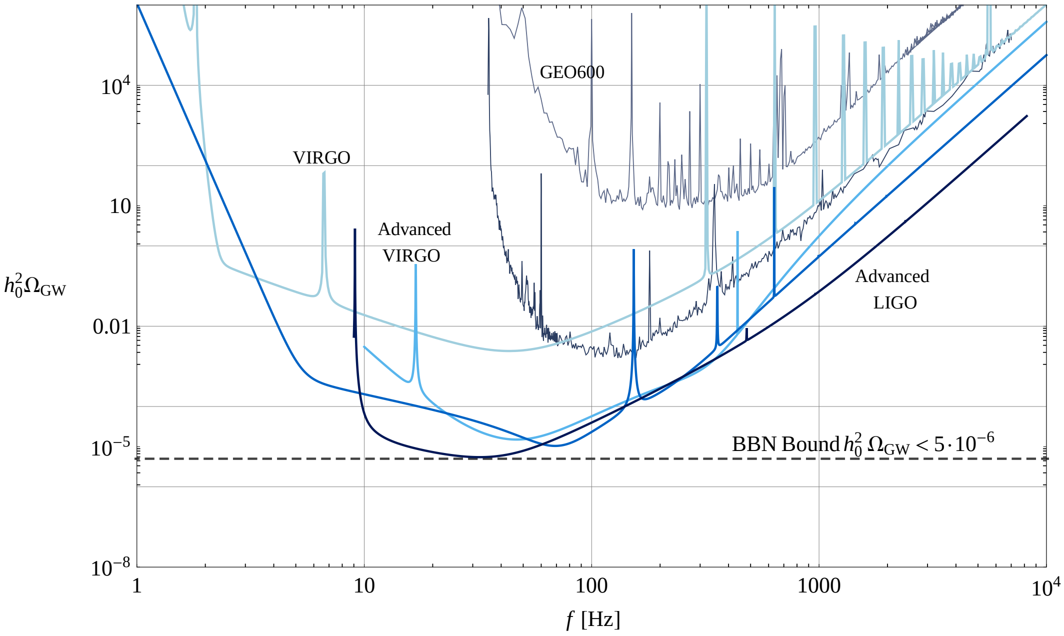

Figure C.6: *Sensitivity curves $h_o^2\Omega_{GW}(f)$ for the ground-based interferometric GW detectors LIGO, VIRGO, GEO600, LCGT / KAGRA, Advanced LIGO and Advanced VIRGO.*

Bibliography

[1] Georges Aad et al. Observation of a new particle in the search for the Standard Model Higgs boson with the ATLAS detector at the LHC. *Phys.Lett.*, B716:1–29, 2012. `arXiv:1207.7214`, `doi:10.1016/j.physletb.2012.08.020`. 51

[2] B. Abbott et al. Analysis of LIGO data for gravitational waves from binary neutron stars. *Phys.Rev.*, D69:122001, 2004. `arXiv:gr-qc/0308069`, `doi:10.1103/PhysRevD.69.122001`. 1, 109

[3] B. Abbott et al. First upper limits from ligo on gravitational wave bursts. *Phys.Rev.*, D69:102001, 2004. `arXiv:gr-qc/0312056`, `doi:10.1103/PhysRevD.69.102001`. 1, 109

[4] B. Abbott et al. First all-sky upper limits from LIGO on the strength of periodic gravitational waves using the Hough transform. *Phys.Rev.*, D72:102004, 2005. `arXiv:gr-qc/0508065`, `doi:10.1103/PhysRevD.72.102004`. 1, 109

[5] B. Abbott et al. Search for gravitational waves from galactic and extra-galactic binary neutron stars. *Phys.Rev.*, D72:082001, 2005. `arXiv:gr-qc/0505041`, `doi:10.1103/PhysRevD.72.082001`. 1, 109

[6] B. Abbott et al. Upper limits on a stochastic background of gravitational waves. *Phys.Rev.Lett.*, 95:221101, 2005. `arXiv:astro-ph/0507254`, `doi:10.1103/PhysRevLett.95.221101`. 109

[7] B.P. Abbott et al. LIGO: The laser interferometer gravitational-wave observatory. *Rept.Prog.Phys.*, 72:076901, 2009. `arXiv:0711.3041`, `doi:10.1088/0034-4885/72/7/076901`. 1, 109

[8] Alex Abramovici, William E. Althouse, Ronald W.P. Drever, Yekta Gursel, Seiji Kawamura, et al. LIGO: The laser interferometer gravitational wave observatory. *Science*, 256:325–333, 1992. 1, 109

[9] T. Accadia et al. Virgo: A laser interferometer to detect gravitational waves. *JINST*, 7:P03012, 2012. `doi:10.1088/1748-0221/7/03/P03012`. 1, 109

[10] Ian Affleck. Quantum Statistical Metastability. *Phys.Rev.Lett.*, 46:388, 1981. doi:10.1103/PhysRevLett.46.388. 30

[11] Jarkko Ahonen and Kari Enqvist. Magnetic field generation in first order phase transition bubble collisions. *Phys.Rev.*, D57:664–673, 1998. arXiv:hep-ph/9704334, doi:10.1103/PhysRevD.57.664. 2

[12] Amine Ahriche. *The electroweak phase transition in models with gauge singlets*. PhD thesis, Bielefeld University, 2007. URL: http://pub.uni-bielefeld.de/publication/2306235. 51

[13] Tomotada Akutsu. DECIGO and DECIGO Pathfinder, 9th LISA Symposium. Paris, 2012. URL: http://tamago.mtk.nao.ac.jp/decigo/File/international/9thLISA_20120524_akutsu.pdf. 111

[14] Laila Alabidi, Kazunori Kohri, Misao Sasaki, and Yuuiti Sendouda. Observable Spectra of Induced Gravitational Waves from Inflation. *JCAP*, 1209:017, 2012. arXiv:1203.4663, doi:10.1088/1475-7516/2012/09/017. 1, 111

[15] Andreas Albrecht, Savas Dimopoulos, W. Fischer, Edward W. Kolb, Stuart Raby, et al. NEW INFLATION IN SUPERSYMMETRIC THEORIES. *Nucl.Phys.*, B229:528, 1983. doi:10.1016/0550-3213(83)90347-4. 25

[16] Andreas Albrecht, Paul J. Steinhardt, Michael S. Turner, and Frank Wilczek. Reheating an Inflationary Universe. *Phys.Rev.Lett.*, 48:1437, 1982. doi:10.1103/PhysRevLett.48.1437. 25

[17] Bruce Allen. The Stochastic Gravity Wave Background in Inflationary Universe Models. *Phys.Rev.*, D37:2078, 1988. doi:10.1103/PhysRevD.37.2078. 1

[18] Guido Altarelli. The Standard electroweak theory and beyond. pages 1–59, 2000. arXiv:hep-ph/0011078. 62

[19] Ugo Amaldi, Wim de Boer, and Hermann Furstenau. Comparison of grand unified theories with electroweak and strong coupling constants measured at LEP. *Phys.Lett.*, B260:447–455, 1991. doi:10.1016/0370-2693(91)91641-8. 2

[20] Masaki Ando, Koji Arai, Youichi Aso, Peter Beyersdorf, Kazuhiro Hayama, et al. Observation results by the TAMA300 detector on gravitational wave bursts from stellar-core collapses. *Phys.Rev.*, D71:082002, 2005. arXiv:gr-qc/0411027, doi:10.1103/PhysRevD.71.082002. 1, 109

[21] Masaki Ando et al. Stable operation of a 300-m laser interferometer with sufficient sensitivity to detect gravitational wave events within our galaxy. *Phys.Rev.Lett.*, 86:3950, 2001. arXiv:astro-ph/0105473, doi:10.1103/PhysRevLett.86.3950. 1, 109

[22] F. Antonucci, M. Armano, H. Audley, G. Auger, M. Benedetti, et al. LISA Pathfinder: Mission and status. *Class.Quant.Grav.*, 28:094001, 2011. doi:10.1088/0264-9381/28/9/094001. 1, 110

[23] Riccardo Apreda, Michele Maggiore, Alberto Nicolis, and Antonio Riotto. Gravitational waves from electroweak phase transitions. *Nucl.Phys.*, B631:342–368, 2002. arXiv:gr-qc/0107033, doi:10.1016/S0550-3213(02)00264-X. 2, 3, 30

[24] K. Arai et al. Status of Japanese gravitational wave detectors. *Class.Quant.Grav.*, 26:204020, 2009. doi:10.1088/0264-9381/26/20/204020. 110

[25] Peter Brockway Arnold and Olivier Espinosa. The Effective potential and first order phase transitions: Beyond leading-order. *Phys.Rev.*, D47:3546, 1993. arXiv:hep-ph/9212235, doi:10.1103/PhysRevD.47.3546,10.1103/PhysRevD.50.6662. 22, 104

[26] A. Ashoorioon and T. Konstandin. Strong electroweak phase transitions without collider traces. *JHEP*, 0907:086, 2009. arXiv:0904.0353, doi:10.1088/1126-6708/2009/07/086. 40

[27] K.S. Babu, Yanzhi Meng, and Zurab Tavartkiladze. New Ways to Leptogenesis with Gauged B-L Symmetry. *Phys.Lett.*, B681:37–43, 2009. arXiv:0901.1044, doi:10.1016/j.physletb.2009.09.036. 68

[28] G. Barenboim and J. Bernabeu. Spontaneous breakdown of CP in left-right symmetric models. *Z.Phys.*, C73:321–331, 1997. arXiv:hep-ph/9603379, doi:10.1007/s002880050321. 63, 64, 68

[29] Gabriela Barenboim and Nuria Rius. Electroweak phase transitions in left-right symmetric models. *Phys.Rev.*, D58:065010, 1998. arXiv:hep-ph/9803215, doi:10.1103/PhysRevD.58.065010. 62, 68

[30] R.A. Battye, R.R. Caldwell, and E.P.S. Shellard. Gravitational waves from cosmic strings. pages 11–31, 1997. arXiv:astro-ph/9706013. 1

[31] M.L. Bellac. *Thermal Field Theory*. Cambridge Monographs on Mathematical Physics. Cambridge University Press, 2000. 9, 15

[32] J. Beringer et al. Review of Particle Physics (RPP). *Phys.Rev.*, D86:010001, 2012. doi:10.1103/PhysRevD.86.010001. 51

[33] Claude W. Bernard. Feynman Rules for Gauge Theories at Finite Temperature. *Phys.Rev.*, D9:3312, 1974. doi:10.1103/PhysRevD.9.3312. 15

[34] S. Blundell and K.M. Blundell. *Concepts in Thermal Physics*. Oxford University Press, 2006. URL: http://books.google.de/books?id=6T9LmTJJSPgC. 25

[35] A.I. Bochkarev and M.E. Shaposhnikov. Electroweak Production of Baryon Asymmetry and Upper Bounds on the Higgs and Top Masses. *Mod.Phys.Lett.*, A2:417, 1987. doi:10.1142/S0217732387000537. 3

[36] Dietrich Bodeker, Lars Fromme, Stephan J. Huber, and Michael Seniuch. The Baryon asymmetry in the standard model with a low cut-off. *JHEP*, 0502:026, 2005. arXiv:hep-ph/0412366, doi:10.1088/1126-6708/2005/02/026. 3

[37] N.N. Bogoliubov and D.V. Sirkov. *Introduction to the theory of quantized fields: transl. from the Russian*. Interscience monographs in physics and astronomy. 1959. URL: `http://books.google.de/books?id=zjdDtwAACAAJ`. 10

[38] Matthew Bowen, Yanou Cui, and James D. Wells. Narrow trans-TeV Higgs bosons and H —> hh decays: Two LHC search paths for a hidden sector Higgs boson. *JHEP*, 0703:036, 2007. `arXiv:hep-ph/0701035`, `doi:10.1088/1126-6708/2007/03/036`. 4, 39

[39] D. Boyanovsky, H.J. de Vega, and M. Simionato. Primordial magnetic fields from cosmological phase transitions. 2003. `arXiv:astro-ph/0305131`. 2

[40] Robert H. Brandenberger. Quantum Field Theory Methods and Inflationary Universe Models. *Rev.Mod.Phys.*, 57:1, 1985. `doi:10.1103/RevModPhys.57.1`. 9

[41] A. Brignole, J.R. Espinosa, M. Quiros, and F. Zwirner. Aspects of the electroweak phase transition in the minimal supersymmetric standard model. *Phys.Lett.*, B324:181–191, 1994. `arXiv:hep-ph/9312296`, `doi:10.1016/0370-2693(94)90405-7`. 3

[42] R. Brustein, M. Gasperini, Massimo Giovannini, and G. Veneziano. Relic gravitational waves from string cosmology. *Phys.Lett.*, B361:45–51, 1995. `arXiv:hep-th/9507017`, `doi:10.1016/0370-2693(95)01128-D`. 1

[43] W. Buchmuller, Z. Fodor, T. Helbig, and D. Walliser. The Weak - electroweak phase transition. *Annals Phys.*, 234:260–299, 1994. `arXiv:hep-ph/9303251`, `doi:10.1006/aphy.1994.1082`. 2

[44] Alessandra Buonanno, Gunter Sigl, Georg G. Raffelt, Hans-Thomas Janka, and Ewald Müller. Stochastic gravitational wave background from cosmological supernovae. *Phys.Rev.*, D72:084001, 2005. `arXiv:astro-ph/0412277`, `doi:10.1103/PhysRevD.72.084001`. 1, 109

[45] R.R. Caldwell and Bruce Allen. Cosmological constraints on cosmic string gravitational radiation. *Phys.Rev.*, D45:3447–3468, 1992. `doi:10.1103/PhysRevD.45.3447`. 1

[46] R.R. Caldwell, R.A. Battye, and E.P.S. Shellard. Relic gravitational waves from cosmic strings: Updated constraints and opportunities for detection. *Phys.Rev.*, D54:7146–7152, 1996. `arXiv:astro-ph/9607130`, `doi:10.1103/PhysRevD.54.7146`. 1

[47] Jr. Callan, Curtis G. and Sidney R. Coleman. The Fate of the False Vacuum. 2. First Quantum Corrections. *Phys.Rev.*, D16:1762–1768, 1977. `doi:10.1103/PhysRevD.16.1762`. 30

[48] Chiara Caprini and Ruth Durrer. Gravitational waves from stochastic relativistic sources: Primordial turbulence and magnetic fields. *Phys.Rev.*, D74:063521, 2006. `arXiv:astro-ph/0603476`, `doi:10.1103/PhysRevD.74.063521`. 2, 26

[49] Chiara Caprini, Ruth Durrer, Thomas Konstandin, and Geraldine Servant. General Properties of the Gravitational Wave Spectrum from Phase Transitions. *Phys.Rev.*, D79:083519, 2009. `arXiv:0901.1661`, `doi:10.1103/PhysRevD.79.083519`. 1

[50] Chiara Caprini, Ruth Durrer, and Geraldine Servant. Gravitational wave generation from bubble collisions in first-order phase transitions: An analytic approach. *Phys.Rev.*, D77:124015, 2008. `arXiv:0711.2593`, `doi:10.1103/PhysRevD.77.124015`. 2

[51] Marcela S. Carena and Howard E. Haber. Higgs boson theory and phenomenology. *Prog.Part.Nucl.Phys.*, 50:63–152, 2003. `arXiv:hep-ph/0208209`, `doi:10.1016/S0146-6410(02)00177-1`. 103

[52] B. Caron, A. Dominjon, C. Drezen, R. Flaminio, X. Grave, et al. The Virgo interferometer. *Class.Quant.Grav.*, 14:1461–1469, 1997. `doi:10.1088/0264-9381/14/6/011`. 1, 109

[53] M.E. Carrington. The Effective potential at finite temperature in the Standard Model. *Phys.Rev.*, D45:2933–2944, 1992. Revised version. `doi:10.1103/PhysRevD.45.2933`. 21, 22, 103

[54] D. Chang, R.N. Mohapatra, and M.K. Parida. A New Approach to Left-Right Symmetry Breaking in Unified Gauge Theories. *Phys.Rev.*, D30:1052, 1984. `doi:10.1103/PhysRevD.30.1052`. 62, 68

[55] D. Chang, R.N. Mohapatra, and M.K. Parida. Decoupling Parity and SU(2)-R Breaking Scales: A New Approach to Left-Right Symmetric Models. *Phys.Rev.Lett.*, 52:1072, 1984. `doi:10.1103/PhysRevLett.52.1072`. 62, 68

[56] Darwin Chang. A Minimal Model of Spontaneous CP Violation with the Gauge Group SU(2)-L x SU(2)-R x U(1)-(B-L). *Nucl.Phys.*, B214:435, 1983. `doi:10.1016/0550-3213(83)90243-2`. 68

[57] Serguei Chatrchyan et al. Observation of a new boson at a mass of 125 GeV with the CMS experiment at the LHC. *Phys.Lett.*, B716:30–61, 2012. `arXiv:1207.7235`, `doi:10.1016/j.physletb.2012.08.021`. 51

[58] Jarny Choi and R.R. Volkas. The Effective potential at finite temperature in the left-right symmetric model. *Phys.Rev.*, D48:1258–1265, 1993. `arXiv:hep-ph/9210223`, `doi:10.1103/PhysRevD.48.1258`. 68, 74, 83, 107

[59] Chris Clarkson and Roy Maartens. Gravity-wave detectors as probes of extra dimensions. *Gen.Rel.Grav.*, 37:1681–1687, 2005. `arXiv:astro-ph/0505277`, `doi:10.1007/s10714-005-0150-8,10.1142/S0218271805007905`. 1

[60] Chris Clarkson and Sanjeev S. Seahra. A gravitational wave window on extra dimensions. *Class.Quant.Grav.*, 24:F33–F40, 2007. `arXiv:astro-ph/0610470`, `doi:10.1088/0264-9381/24/9/F01`. 1

[61] James M. Cline and Kimmo Kainulainen. Supersymmetric electroweak phase transition: Dimensional reduction versus effective potential. *Nucl.Phys.*, B510:88–102, 1998. `arXiv:hep-ph/9705201`, `doi:10.1016/S0550-3213(97)00570-1`. 2, 47

[62] James M. Cline, U.A. Yajnik, S.N. Nayak, and M. Rabikumar. Transient domain walls and lepton asymmetry in the left-right symmetric model. *Phys.Rev.*, D66:065001, 2002. `arXiv:hep-ph/0204319`, `doi:10.1103/PhysRevD.66.065001`. 63, 64, 65, 68, 69

[63] Sidney R. Coleman. The Fate of the False Vacuum. 1. Semiclassical Theory. *Phys.Rev.*, D15:2929–2936, 1977. `doi:10.1103/PhysRevD.15.2929,10.1103/PhysRevD.16.1248`. 30

[64] Sidney R. Coleman and Erick J. Weinberg. Radiative Corrections as the Origin of Spontaneous Symmetry Breaking. *Phys.Rev.*, D7:1888–1910, 1973. `doi:10.1103/PhysRevD.7.1888`. 10

[65] Sidney R. Coleman and Erick J. Weinberg. Radiative Corrections as the Origin of Spontaneous Symmetry Breaking. *Phys.Rev.*, D7:1888–1910, 1973. `doi:10.1103/PhysRevD.7.1888`. 13

[66] F. Csikor, Z. Fodor, and J. Heitger. Endpoint of the hot electroweak phase transition. *Phys.Rev.Lett.*, 82:21–24, 1999. `arXiv:hep-ph/9809291`, `doi:10.1103/PhysRevLett.82.21`. 3

[67] K. Danzmann. LISA: Laser interferometer space antenna for gravitational wave measurements. *Class.Quant.Grav.*, 13:A247–A250, 1996. `doi:10.1088/0264-9381/13/11A/033`. 1, 110

[68] K. Danzmann. LISA: An ESA cornerstone mission for a gravitational wave observatory. *Class.Quant.Grav.*, 14:1399–1404, 1997. `doi:10.1088/0264-9381/14/6/002`. 1, 110

[69] K. Danzmann and A. Rudiger. LISA technology - Concept, status, prospects. *Class.Quant.Grav.*, 20:S1–S9, 2003. 1, 110

[70] A.T. Davies, C.D. Froggatt, and R.G. Moorhouse. Electroweak baryogenesis in the next-to-minimal supersymmetric model. *Phys.Lett.*, B372:88–94, 1996. `arXiv:hep-ph/9603388`, `doi:10.1016/0370-2693(96)00076-7`. 3

[71] A. Dedes, C. Hugonie, S. Moretti, and K. Tamvakis. Phenomenology of a new minimal supersymmetric extension of the standard model. *Phys.Rev.*, D63:055009, 2001. `arXiv:hep-ph/0009125`, `doi:10.1103/PhysRevD.63.055009`. 3

[72] Cedric Delaunay, Christophe Grojean, and James D. Wells. Dynamics of Non-renormalizable Electroweak Symmetry Breaking. *JHEP*, 0804:029, 2008. `arXiv:0711.2511`, `doi:10.1088/1126-6708/2008/04/029`. 21, 22, 41, 104

[73] N.G. Deshpande, J.F. Gunion, Boris Kayser, and Fredrick I. Olness. Left-right symmetric electroweak models with triplet Higgs. *Phys.Rev.*, D44:837–858, 1991. `doi:10.1103/PhysRevD.44.837`. 65, 68

[74] Michael Dine, Robert G. Leigh, Patrick Huet, Andrei D. Linde, and Dmitri A. Linde. Comments on the electroweak phase transition. *Phys.Lett.*, B283:319–325, 1992. `arXiv:hep-ph/9203201`, `doi:10.1016/0370-2693(92)90026-Z`. 2

[75] Michael Dine, Robert G. Leigh, Patrick Y. Huet, Andrei D. Linde, and Dmitri A. Linde. Towards the theory of the electroweak phase transition. *Phys.Rev.*, D46:550–571, 1992. `arXiv:hep-ph/9203203`, `doi:10.1103/PhysRevD.46.550`. 2

[76] L. Dolan and R. Jackiw. Symmetry Behavior at Finite Temperature. *Phys.Rev.*, D9:3320–3341, 1974. `doi:10.1103/PhysRevD.9.3320`. 15, 17, 21

[77] Alexander D. Dolgov, Dario Grasso, and Alberto Nicolis. Relic backgrounds of gravitational waves from cosmic turbulence. *Phys.Rev.*, D66:103505, 2002. `arXiv:astro-ph/0206461`, `doi:10.1103/PhysRevD.66.103505`. 2, 26

[78] Jean Francois Dufaux, Amanda Bergman, Gary N. Felder, Lev Kofman, and Jean-Philippe Uzan. Theory and Numerics of Gravitational Waves from Preheating after Inflation. *Phys.Rev.*, D76:123517, 2007. `arXiv:0707.0875`, `doi:10.1103/PhysRevD.76.123517`. 1

[79] Richard Easther and Eugene A. Lim. Stochastic gravitational wave production after inflation. *JCAP*, 0604:010, 2006. `arXiv:astro-ph/0601617`, `doi:10.1088/1475-7516/2006/04/010`. 1

[80] Einstein-Telescope. Project Homepage, Last Updated: March 15, 2012. Retrieved: October 14, 2012. URL: `https://www.et-gw.eu/et/`. 110

[81] Jose R. Espinosa, Ben Gripaios, Thomas Konstandin, and Francesco Riva. Electroweak Baryogenesis in Non-minimal Composite Higgs Models. *JCAP*, 1201:012, 2012. `arXiv:1110.2876`, `doi:10.1088/1475-7516/2012/01/012`. 53, 79, 80, 85

[82] Jose R. Espinosa, Thomas Konstandin, and Francesco Riva. Strong Electroweak Phase Transitions in the Standard Model with a Singlet. *Nucl.Phys.*, B854:592–630, 2012. `arXiv:1107.5441`, `doi:10.1016/j.nuclphysb.2011.09.010`. 40, 50, 66, 68, 70, 74, 76

[83] Jose Ramon Espinosa and Mariano Quiros. Novel Effects in Electroweak Breaking from a Hidden Sector. *Phys.Rev.*, D76:076004, 2007. `arXiv:hep-ph/0701145`, `doi:10.1103/PhysRevD.76.076004`. 4, 39

[84] J.R. Espinosa, T. Konstandin, J.M. No, and M. Quiros. Some Cosmological Implications of Hidden Sectors. *Phys.Rev.*, D78:123528, 2008. `arXiv:0809.3215`, `doi:10.1103/PhysRevD.78.123528`. 4, 39

[85] J.R. Espinosa and M. Quiros. The Electroweak phase transition with a singlet. *Phys.Lett.*, B305:98–105, 1993. `arXiv:hep-ph/9301285`, `doi:10.1016/0370-2693(93)91111-Y`. 104

[86] J.R. Espinosa, M. Quiros, and F. Zwirner. On the nature of the electroweak phase transition. *Phys.Lett.*, B314:206–216, 1993. `arXiv:hep-ph/9212248`, `doi:10.1016/0370-2693(93)90450-V`. 3

[87] Glennys R. Farrar and M.E. Shaposhnikov. Baryon asymmetry of the universe in the minimal Standard Model. *Phys.Rev.Lett.*, 70:2833–2836, 1993. `arXiv:hep-ph/9305274`, `doi:10.1103/PhysRevLett.70.2833`. 2

[88] Glennys R. Farrar and M.E. Shaposhnikov. Baryon asymmetry of the universe in the standard electroweak theory. *Phys.Rev.*, D50:774, 1994. `arXiv:hep-ph/9305275`, `doi:10.1103/PhysRevD.50.774`. 2

[89] Elisa Fenu, Daniel G. Figueroa, Ruth Durrer, and Juan Garcia-Bellido. Gravitational waves from self-ordering scalar fields. *JCAP*, 0910:005, 2009. `arXiv:0908.0425`, `doi:10.1088/1475-7516/2009/10/005`. 3

[90] Valeria Ferrari, Sabino Matarrese, and Raffaella Schneider. Gravitational wave background from a cosmological population of core collapse supernovae. *Mon.Not.Roy.Astron.Soc.*, 303:247, 1999. `arXiv:astro-ph/9804259`, `doi:10.1046/j.1365-8711.1999.02194.x`. 1

[91] R.P. Feynman and A.R. Hibbs. *Quantum mechanics and path integrals*. International series in pure and applied physics. McGraw-Hill, 1965. 10

[92] D.J. Fixsen. The Temperature of the Cosmic Microwave Background. *Astrophys.J.*, 707:916–920, 2009. `arXiv:0911.1955`, `doi:10.1088/0004-637X/707/2/916`. 33

[93] J.M. Frere, L. Houart, J.M. Moreno, J. Orloff, and M. Tytgat. Generation of the baryon asymmetry of the universe within the left-right symmetric model. *Phys.Lett.*, B314:289–297, 1993. `arXiv:hep-ph/9301228`, `doi:10.1016/0370-2693(93)91238-I`. 65, 68

[94] Avijit Ganguly, Jitendra C. Parikh, and Utpal Sarkar. Low-energy leptogenesis in left-right symmetric models. *Phys.Lett.*, B385:175–180, 1996. `arXiv:hep-ph/9408271`, `doi:10.1016/0370-2693(96)00892-1`. 65, 68

[95] Juan Garcia-Bellido and Daniel G. Figueroa. A stochastic background of gravitational waves from hybrid preheating. *Phys.Rev.Lett.*, 98:061302, 2007. `arXiv:astro-ph/0701014`, `doi:10.1103/PhysRevLett.98.061302`. 1

[96] M. Gasperini and G. Veneziano. The Pre - big bang scenario in string cosmology. *Phys.Rept.*, 373:1–212, 2003. `arXiv:hep-th/0207130`, `doi:10.1016/S0370-1573(02)00389-7`. 1

[97] GEO600. Sensitivity Curve Data, Last Updated: June 21, 2006. Retrieved: October 2, 2012. URL: `http://www.geo600.uni-hannover.de/geocurves/`. 87, 111, 112

[98] Gian F. Giudice. The Electroweak phase transition in supersymmetry. *Phys.Rev.*, D45:3177–3182, 1992. `doi:10.1103/PhysRevD.45.3177`. 3

[99] Grigol Gogoberidze, Tina Kahniashvili, and Arthur Kosowsky. The Spectrum of Gravitational Radiation from Primordial Turbulence. *Phys.Rev.*, D76:083002, 2007. `arXiv:0705.1733`, `doi:10.1103/PhysRevD.76.083002`. 2, 26

[100] J. Goldstone. Field Theories with Superconductor Solutions. *Nuovo Cim.*, 19:154–164, 1961. `doi:10.1007/BF02812722`. 49

[101] I.S. Gradshtein, I.M. Ryzhik, and A. Jeffrey. *Table of Integrals, Series, and Products*. Elsevier Science, 2000. 14

[102] Eric Greenwood and Pascal M. Vaudrevange. Gravity waves from the non-renormalizable Electroweak Vacua phase transition. 2010. `arXiv:1011.5881`. 31

[103] Christophe Grojean and Geraldine Servant. Gravitational Waves from Phase Transitions at the Electroweak Scale and Beyond. *Phys.Rev.*, D75:043507, 2007. `arXiv:hep-ph/0607107`, `doi:10.1103/PhysRevD.75.043507`. 1, 26, 28, 33, 34, 36, 86, 92

[104] Christophe Grojean, Geraldine Servant, and James D. Wells. First-order electroweak phase transition in the standard model with a low cutoff. *Phys.Rev.*, D71:036001, 2005. `arXiv:hep-ph/0407019`, `doi:10.1103/PhysRevD.71.036001`. 3, 29

[105] S.W. Ham and S.K. Oh. Electroweak phase transition in the standard model with a dimension-six Higgs operator at one-loop level. *Phys.Rev.*, D70:093007, 2004. `arXiv:hep-ph/0408324`, `doi:10.1103/PhysRevD.70.093007`. 3

[106] J Harms. *The Detection of Gravitational Waves - Data Analysis and Interferometry*. PhD thesis, Gottfried Wilhelm Leibniz Universität Hannover, 2006, eDoc: 307745. URL: `http://pubman.mpdl.mpg.de/pubman/faces/viewItemFullPage.jsp?itemId=escidoc:150885:1`. 111

[107] G.M. Harry, P. Fritschel, D.A. Shaddock, W. Folkner, and E.S. Phinney. Laser interferometry for the big bang observer. *Class.Quant.Grav.*, 23:4887–4894, 2006. `doi:10.1088/0264-9381/23/15/008`. 1, 110, 111

[108] Gregory M. Harry. Advanced LIGO: The next generation of gravitational wave detectors. *Class.Quant.Grav.*, 27:084006, 2010. `doi:10.1088/0264-9381/27/8/084006`. 86, 109

[109] S. Hild, M. Abernathy, F. Acernese, P. Amaro-Seoane, N. Andersson, et al. Sensitivity Studies for Third-Generation Gravitational Wave Observatories. *Class.Quant.Grav.*, 28:094013, 2011. `arXiv:1012.0908`, `doi:10.1088/0264-9381/28/9/094013`. 110

[110] Craig J. Hogan. Magnetohydrodynamic Effects of a First-Order Cosmological Phase Transition. *Phys.Rev.Lett.*, 51:1488–1491, 1983. `doi:10.1103/PhysRevLett.51.1488`. 2

[111] S.J. Huber and M.G. Schmidt. Electroweak baryogenesis: Concrete in a SUSY model with a gauge singlet. *Nucl.Phys.*, B606:183–230, 2001. `arXiv:hep-ph/0003122`, `doi:10.1016/S0550-3213(01)00250-4`. 3

[112] Stephan J. Huber and Thomas Konstandin. Gravitational Wave Production by Collisions: More Bubbles. *JCAP*, 0809:022, 2008. `arXiv:0806.1828`, `doi:10.1088/1475-7516/2008/09/022`. 1, 2, 4, 26, 34, 35, 36, 78, 81, 91, 92, 113

[113] Stephan J. Huber and Thomas Konstandin. Production of gravitational waves in the nMSSM. *JCAP*, 0805:017, 2008. arXiv:0709.2091, doi:10.1088/1475-7516/2008/05/017. 3, 4, 27, 28, 36, 81, 83, 91, 92, 113

[114] Stephan J. Huber, Thomas Konstandin, Tomislav Prokopec, and Michael G. Schmidt. Electroweak Phase Transition and Baryogenesis in the nMSSM. *Nucl.Phys.*, B757:172–196, 2006. arXiv:hep-ph/0606298, doi:10.1016/j.nuclphysb.2006.09.003. 3

[115] Satoshi Iso, Nobuchika Okada, and Yuta Orikasa. Classically conformal B^- L extended Standard Model. *Phys.Lett.*, B676:81–87, 2009. arXiv:0902.4050, doi:10.1016/j.physletb.2009.04.046. 68

[116] Satoshi Iso, Nobuchika Okada, and Yuta Orikasa. The minimal B-L model naturally realized at TeV scale. *Phys.Rev.*, D80:115007, 2009. arXiv:0909.0128, doi:10.1103/PhysRevD.80.115007. 68

[117] Satoshi Iso, Nobuchika Okada, and Yuta Orikasa. Resonant Leptogenesis in the Minimal B-L Extended Standard Model at TeV. *Phys.Rev.*, D83:093011, 2011. arXiv:1011.4769, doi:10.1103/PhysRevD.83.093011. 68

[118] Y. Iwasaki, K. Kanaya, S. Kaya, S. Sakai, and T. Yoshie. QCD phase transition with strange quark in Wilson formalism for fermions. *Z.Phys.*, C71:343–346, 1996. arXiv:hep-lat/9505017, doi:10.1007/s002880050180. 2

[119] R. Jackiw. Functional evaluation of the effective potential. *Phys.Rev.*, D9:1686, 1974. doi:10.1103/PhysRevD.9.1686. 12, 13

[120] P. John and M.G. Schmidt. Bubble wall velocity in the MSSM. pages 284–288, 2000. arXiv:hep-ph/0012077. 32

[121] G. Jona-Lasinio. Relativistic field theories with symmetry breaking solutions. *Nuovo Cim.*, 34:1790–1795, 1964. doi:10.1007/BF02750573. 10

[122] LCGT / KAGRA. Sensitivity Curve Data, Last Updated: 2010. Retrieved: October 2, 2012. URL: http://gwcenter.icrr.u-tokyo.ac.jp/en/researcher/parameter. 87, 112

[123] K. Kajantie, M. Laine, K. Rummukainen, and Mikhail E. Shaposhnikov. Is there a hot electroweak phase transition at m(H) larger or equal to m(W)? *Phys.Rev.Lett.*, 77:2887–2890, 1996. arXiv:hep-ph/9605288, doi:10.1103/PhysRevLett.77.2887. 3

[124] Marc Kamionkowski and Katherine Freese. Instability and subsequent evolution of electroweak bubbles. *Phys.Rev.Lett.*, 69:2743–2746, 1992. arXiv:hep-ph/9208202, doi:10.1103/PhysRevLett.69.2743. 26

[125] Marc Kamionkowski, Arthur Kosowsky, and Michael S. Turner. Gravitational radiation from first order phase transitions. *Phys.Rev.*, D49:2837–2851, 1994. arXiv:astro-ph/9310044, doi:10.1103/PhysRevD.49.2837. 1, 26, 27, 32, 34, 35, 78

[126] J.I. Kapusta and C. Gale. *Finite-Temperature Field Theory: Principles and Applications*. Cambridge monographs on mechanics and applied mathematics. Cambridge University Press, 2006. 9, 15

[127] S. Kawamura, T. Nakamura, M. Ando, N. Seto, K. Tsubono, et al. The Japanese space gravitational wave antenna DECIGO. *Class.Quant.Grav.*, 23:S125–S132, 2006. `doi:10.1088/0264-9381/23/8/S17`. 110

[128] Seiji Kawamura, Masaki Ando, Naoki Seto, Shuichi Sato, Takashi Nakamura, et al. The Japanese space gravitational wave antenna: DECIGO. *Class.Quant.Grav.*, 28:094011, 2011. `doi:10.1088/0264-9381/28/9/094011`. 110

[129] John Kehayias and Stefano Profumo. Semi-Analytic Calculation of the Gravitational Wave Signal From the Electroweak Phase Transition for General Quartic Scalar Effective Potentials. *JCAP*, 1003:003, 2010. `arXiv:0911.0687`, `doi:10.1088/1475-7516/2010/03/003`. 26, 28, 29

[130] D.A. Kirzhnits. Weinberg model in the hot universe. *JETP Lett.*, 15:529–531, 1972. 15

[131] D.A. Kirzhnits and Andrei D. Linde. Macroscopic Consequences of the Weinberg Model. *Phys.Lett.*, B42:471–474, 1972. `doi:10.1016/0370-2693(72)90109-8`. 15

[132] D.A. Kirzhnits and Andrei D. Linde. A Relativistic phase transition. *Sov.Phys.JETP*, 40:628, 1975. 15

[133] E.W. Kolb and M.S. Turner. *The early universe*. Frontiers in physics. Westview Press, 1994. 27, 47

[134] Thomas Konstandin and Stephan J. Huber. Numerical approach to multi dimensional phase transitions. *JCAP*, 0606:021, 2006. `arXiv:hep-ph/0603081`, `doi:10.1088/1475-7516/2006/06/021`. 30

[135] Arthur Kosowsky, Andrew Mack, and Tinatin Kahniashvili. Gravitational radiation from cosmological turbulence. *Phys.Rev.*, D66:024030, 2002. `arXiv:astro-ph/0111483`, `doi:10.1103/PhysRevD.66.024030`. 2, 26

[136] Arthur Kosowsky and Michael S. Turner. Gravitational radiation from colliding vacuum bubbles: envelope approximation to many bubble collisions. *Phys.Rev.*, D47:4372–4391, 1993. `arXiv:astro-ph/9211004`, `doi:10.1103/PhysRevD.47.4372`. 2, 26

[137] Arthur Kosowsky, Michael S. Turner, and Richard Watkins. Gravitational radiation from colliding vacuum bubbles. *Phys.Rev.*, D45:4514–4535, 1992. `doi:10.1103/PhysRevD.45.4514`. 2, 26

[138] Arthur Kosowsky, Michael S. Turner, and Richard Watkins. Gravitational waves from first order cosmological phase transitions. *Phys.Rev.Lett.*, 69:2026–2029, 1992. Revised version. `doi:10.1103/PhysRevLett.69.2026`. 1, 26

[139] Hideaki Kudoh, Atsushi Taruya, Takashi Hiramatsu, and Yoshiaki Himemoto. Detecting a gravitational-wave background with next-generation space interferometers. *Phys.Rev.*, D73:064006, 2006. arXiv:gr-qc/0511145, doi:10.1103/PhysRevD.73.064006. 1, 110, 111

[140] K. Kuroda. Status of LCGT. *Class.Quant.Grav.*, 27:084004, 2010. doi:10.1088/0264-9381/27/8/084004. 110

[141] K. Kuroda et al. Large scale cryogenic gravitational wave telescope. *Int.J.Mod.Phys.*, D8:557–579, 1999. doi:10.1142/S0218271899000390. 110

[142] Paul Langacker. Grand Unified Theories and Proton Decay. *Phys.Rept.*, 72:185, 1981. doi:10.1016/0370-1573(81)90059-4. 3

[143] Henry Lew and Antonio Riotto. Baryogenesis, domain walls and the role of gravity. *Phys.Lett.*, B309:258–263, 1993. arXiv:hep-ph/9304203, doi:10.1016/0370-2693(93)90930-G. 68

[144] LIGO. Sensitivity Curve Data, Last Updated: March 23, 2004. Retrieved: October 2, 2012. URL: http://www.ligo.caltech.edu/~jzweizig/distribution/LSC_Data/. 87, 111, 112

[145] Advanced LIGO. Sensitivity Curve Data, Last Updated: January 25, 2010. Retrieved: October 2, 2012. URL: https://dcc.ligo.org/cgi-bin/DocDB/ShowDocument?docid=2974. 87, 112

[146] Andrei D. Linde. Dynamical Symmetry Restoration and Constraints on Masses and Coupling Constants in Gauge Theories. *JETP Lett.*, 23:64–67, 1976. 15

[147] Andrei D. Linde. On the Vacuum Instability and the Higgs Meson Mass. *Phys.Lett.*, B70:306, 1977. doi:10.1016/0370-2693(77)90664-5. 30

[148] Andrei D. Linde. VACUUM INSTABILITY, COSMOLOGY AND CONSTRAINTS ON PARTICLE MASSES IN THE WEINBERG-SALAM MODEL. *Phys.Lett.*, B92:119, 1980. doi:10.1016/0370-2693(80)90318-4. 15

[149] Andrei D. Linde. THE NEW INFLATIONARY UNIVERSE SCENARIO. 1982. 25

[150] Andrei D. Linde. Decay of the False Vacuum at Finite Temperature. *Nucl.Phys.*, B216:421, 1983. doi:10.1016/0550-3213(83)90293-6. 29, 30, 31

[151] Andrei D. Linde. Particle physics and inflationary cosmology. *Contemp.Concepts Phys.*, 5:1–362, 1990. arXiv:hep-th/0503203. 1

[152] LISA. Online Sensitivity Curve Generator for Spaceborne Gravitational Wave Observatories, Last Updated: April 29, 2003. Retrieved: October 23, 2012. URL: http://www.srl.caltech.edu/~shane/sensitivity/MakeCurve.html. 87, 92, 111, 112

[153] LISA. Project Homepage, Last Updated: June 09, 2011. Retrieved: October 23, 2012. URL: http://lisa.nasa.gov/. 1, 110

[154] H. Luck. The GEO-600 project. *Class.Quant.Grav.*, 14:1471–1476, 1997. `doi:10.1088/0264-9381/14/6/012`. 110

[155] Harald Luck, Christopf Affeldt, Jerome Degallaix, Andreas Freise, Hartmut Grote, et al. The upgrade of GEO600. *J.Phys.Conf.Ser.*, 228:012012, 2010. `arXiv:1004.0339`, `doi:10.1088/1742-6596/228/1/012012`. 110

[156] Michele Maggiore. Gravitational wave experiments and early universe cosmology. *Phys.Rept.*, 331:283–367, 2000. `arXiv:gr-qc/9909001`, `doi:10.1016/S0370-1573(99)00102-7`. 4, 26, 33, 83, 109, 110, 111, 113, 116

[157] Takeo Matsubara. A New approach to quantum statistical mechanics. *Prog.Theor.Phys.*, 14:351–378, 1955. `doi:10.1143/PTP.14.351`. 16

[158] A. Menon, D.E. Morrissey, and C.E.M. Wagner. Electroweak baryogenesis and dark matter in the nMSSM. *Phys.Rev.*, D70:035005, 2004. `arXiv:hep-ph/0404184`, `doi:10.1103/PhysRevD.70.035005`. 3

[159] Rabindra N. Mohapatra, Frank E. Paige, and D.P. Sidhu. Symmetry Breaking and Naturalness of Parity Conservation in Weak Neutral Currents in Left-Right Symmetric Gauge Theories. *Phys.Rev.*, D17:2462, 1978. `doi:10.1103/PhysRevD.17.2462`. 63

[160] Rabindra N. Mohapatra and Goran Senjanovic. Neutrino Mass and Spontaneous Parity Violation. *Phys.Rev.Lett.*, 44:912, 1980. `doi:10.1103/PhysRevLett.44.912`. 62

[161] Rabindra N. Mohapatra and Goran Senjanovic. Neutrino Masses and Mixings in Gauge Models with Spontaneous Parity Violation. *Phys.Rev.*, D23:165, 1981. `doi:10.1103/PhysRevD.23.165`. 62

[162] R.N. Mohapatra. *Unification and Supersymmetry: The Frontiers of Quark-Lepton Physics*. Graduate Texts in Contemporary Physics. Springer, 2010. 4, 61, 62

[163] R.N. Mohapatra and Jogesh C. Pati. A Natural Left-Right Symmetry. *Phys.Rev.*, D11:2558, 1975. `doi:10.1103/PhysRevD.11.2558`. 4, 61

[164] R.N. Mohapatra and X. Zhang. Electroweak baryogenesis in left-right symmetric models. *Phys.Rev.*, D46:5331–5336, 1992. `doi:10.1103/PhysRevD.46.5331`. 68

[165] Guy D. Moore and Tomislav Prokopec. Bubble wall velocity in a first order electroweak phase transition. *Phys.Rev.Lett.*, 75:777–780, 1995. `arXiv:hep-ph/9503296`, `doi:10.1103/PhysRevLett.75.777`. 32

[166] Stanley Myint. Baryogenesis constraints on the minimal supersymmetric model. *Phys.Lett.*, B287:325–330, 1992. `arXiv:hep-ph/9206266`, `doi:10.1016/0370-2693(92)90991-C`. 3

[167] Alberto Nicolis. Relic gravitational waves from colliding bubbles and cosmic turbulence. *Class.Quant.Grav.*, 21:L27, 2004. `arXiv:gr-qc/0303084`. 2, 25, 26, 27, 28, 32, 33

[168] C. Panagiotakopoulos and K. Tamvakis. Stabilized NMSSM without domain walls. *Phys.Lett.*, B446:224–227, 1999. `arXiv:hep-ph/9809475`, `doi:10.1016/S0370-2693(98)01493-2`. 3

[169] Jogesh C. Pati and Abdus Salam. Lepton Number as the Fourth Color. *Phys.Rev.*, D10:275–289, 1974. `doi:10.1103/PhysRevD.10.275,10.1103/PhysRevD.11.703`. 4, 61

[170] Brian Patt and Frank Wilczek. Higgs-field portal into hidden sectors. 2006. `arXiv:hep-ph/0605188`. 4, 39

[171] M.E. Peskin and D.V. Schroeder. *An introduction to quantum field theory*. Advanced Book Program. Addison-Wesley Pub. Co., 1995. 40

[172] Massimo Pietroni. The Electroweak phase transition in a nonminimal supersymmetric model. *Nucl.Phys.*, B402:27–45, 1993. `arXiv:hep-ph/9207227`, `doi:10.1016/0550-3213(93)90635-3`. 3

[173] G. Pizzella. Resonant detectors for the search for gravitational waves. *Class.Quant.Grav.*, 14:1481–1485, 1997. `doi:10.1088/0264-9381/14/6/014`. 109

[174] Chris Quigg. Spontaneous Symmetry Breaking as a Basis of Particle Mass. *Rept.Prog.Phys.*, 70:1019–1054, 2007. `arXiv:0704.2232`, `doi:10.1088/0034-4885/70/7/R01`. 39, 40

[175] M. Quiros. Field theory at finite temperature and phase transitions. *Helv.Phys.Acta*, 67:451–583, 1994. 9, 11, 13, 15, 17, 18, 47, 48

[176] M. Quiros. Higgs bosons in the standard model and the minimal supersymmetric standard model. 1996. `arXiv:hep-ph/9609392`. 39, 41

[177] M. Quiros. Cosmological phase transitions and baryogenesis. 1997. 9, 47

[178] Mariano Quiros. Finite temperature field theory and phase transitions. pages 187–259, 1999. Based on lectures given at the Summer School in High Energy Physics and Cosmology, ICTP, Trieste, Italy, 29 June - 17 July 1998. `arXiv:hep-ph/9901312`. 9, 47

[179] Mariano Quiros. Electroweak baryogenesis and the Higgs and stop masses. *Nucl.Phys.Proc.Suppl.*, 101:401–409, 2001. `arXiv:hep-ph/0101230`, `doi:10.1016/S0920-5632(01)01526-2`. 3

[180] Mariano Quiros. Field theory at finite temperature and phase transitions. *Acta Phys.Polon.*, B38:3661–3703, 2007. 9, 47

[181] K. Rummukainen, M. Tsypin, K. Kajantie, M. Laine, and Mikhail E. Shaposhnikov. The Universality class of the electroweak theory. *Nucl.Phys.*, B532:283–314, 1998. `arXiv:hep-lat/9805013`, `doi:10.1016/S0550-3213(98)00494-5`. 3

[182] Narendra Sahu and Utpal Sarkar. Leptogenesis bound on neutrino masses in left-right symmetric models with spontaneous D-parity violation. *Phys.Rev.*, D74:093002, 2006. `arXiv:hep-ph/0605007`, `doi:10.1103/PhysRevD.74.093002`. 68

[183] Narendra Sahu and Urjit A. Yajnik. Gauged B - L symmetry and baryogenesis via leptogenesis at TeV scale. *Phys.Rev.*, D71:023507, 2005. arXiv:hep-ph/0410075, doi:10.1103/PhysRevD.71.023507. 68

[184] Anjishnu Sarkar and Urjit A. Yajnik. Cosmology in a supersymmetric model with gauged B - L. *Phys.Rev.*, D76:025001, 2007. arXiv:hep-ph/0703142, doi:10.1103/PhysRevD.76.025001. 65, 68

[185] B. Sathyaprakash, M. Abernathy, F. Acernese, P. Ajith, B. Allen, et al. Scientific Potential of Einstein Telescope. 2011. arXiv:1108.1423. 110

[186] Robert Schabinger and James D. Wells. A Minimal spontaneously broken hidden sector and its impact on Higgs boson physics at the large hadron collider. *Phys.Rev.*, D72:093007, 2005. arXiv:hep-ph/0509209, doi:10.1103/PhysRevD.72.093007. 4, 39

[187] Simon Schettler, Tillmann Boeckel, and Jurgen Schaffner-Bielich. Imprints of the QCD Phase Transition on the Spectrum of Gravitational Waves. *Phys.Rev.*, D83:064030, 2011. arXiv:1010.4857, doi:10.1103/PhysRevD.83.064030. 2

[188] Christoph Schmid, Dominik J. Schwarz, and Peter Widerin. Amplification of cosmological inhomogeneities from the QCD transition. *Phys.Rev.*, D59:043517, 1999. arXiv:astro-ph/9807257, doi:10.1103/PhysRevD.59.043517. 2

[189] Sanjeev S. Seahra, Chris Clarkson, and Roy Maartens. Detecting extra dimensions with gravity wave spectroscopy: the black string braneworld. *Phys.Rev.Lett.*, 94:121302, 2005. arXiv:gr-qc/0408032, doi:10.1103/PhysRevLett.94.121302. 1

[190] G. Senjanovic and Rabindra N. Mohapatra. Exact Left-Right Symmetry and Spontaneous Violation of Parity. *Phys.Rev.*, D12:1502, 1975. doi:10.1103/PhysRevD.12.1502. 4, 61, 63

[191] Tristan L. Smith, Marc Kamionkowski, and Asantha Cooray. Direct detection of the inflationary gravitational wave background. *Phys.Rev.*, D73:023504, 2006. arXiv:astro-ph/0506422, doi:10.1103/PhysRevD.73.023504. 1

[192] Kentaro Somiya. Detector configuration of KAGRA: The Japanese cryogenic gravitational-wave detector. *Class.Quant.Grav.*, 29:124007, 2012. arXiv:1111.7185, doi:10.1088/0264-9381/29/12/124007. 110

[193] H.E. Stanley. *Introduction to phase transition and critical phenomena*. International series of monographs on physics. 1971. URL: http://books.google.de/books?id=vC0OQwAACAAJ. 25

[194] Paul Joseph Steinhardt. RELATIVISTIC DETONATION WAVES AND BUBBLE GROWTH IN FALSE VACUUM DECAY. *Phys.Rev.*, D25:2074, 1982. doi:10.1103/PhysRevD.25.2074. 26, 32

[195] K. Takahashi. Higher Order Finite Temperature Effects on Effective Potentials. *Z.Phys.*, C28:247–249, 1985. doi:10.1007/BF01575730. 21

[196] Gerard t'Hooft and M.J.G. Veltman. Regularization and Renormalization of Gauge Fields. *Nucl.Phys.*, B44:189–213, 1972. doi:10.1016/0550-3213(72)90279-9. 14

[197] Michael S. Turner. Detectability of inflation produced gravitational waves. *Phys.Rev.*, D55:435–439, 1997. arXiv:astro-ph/9607066, doi:10.1103/PhysRevD.55.R435. 1

[198] N. Turok. Electroweak bubbles: Nucleation and growth. *Phys.Rev.Lett.*, 68:1803–1806, 1992. doi:10.1103/PhysRevLett.68.1803. 32

[199] T. Vachaspati. Magnetic fields from cosmological phase transitions. *Phys.Lett.*, B265:258–261, 1991. doi:10.1016/0370-2693(91)90051-Q. 2

[200] L. Vergara. Evaluating one loop integrals at finite temperature. *J.Phys.A*, A30:6977–6980, 1997. doi:10.1088/0305-4470/30/19/031. 101

[201] A. Vilenkin. GRAVITATIONAL RADIATION FROM COSMIC STRINGS. *Phys.Lett.*, B107:47–50, 1981. doi:10.1016/0370-2693(81)91144-8. 1

[202] Alexander Vilenkin. Cosmic Strings and Domain Walls. *Phys.Rept.*, 121:263, 1985. doi:10.1016/0370-1573(85)90033-X. 1

[203] VIRGO. Sensitivity Curve Data, Last Updated: August 27, 2003. Retrieved: October 2, 2012. URL: https://wwwcascina.virgo.infn.it/senscurve/. 87, 111, 112

[204] Advanced VIRGO. Sensitivity Curve Data, Last Updated: June 14, 2012. Retrieved: October 2, 2012. URL: https://wwwcascina.virgo.infn.it/advirgo/. 87, 109, 111, 112

[205] Erick J. Weinberg. Radiative corrections as the origin of spontaneous symmetry breaking. 1973. arXiv:hep-th/0507214. 10, 11, 13

[206] Steven Weinberg. Gauge and Global Symmetries at High Temperature. *Phys.Rev.*, D9:3357–3378, 1974. doi:10.1103/PhysRevD.9.3357. 15

[207] Edward Witten. Cosmic Separation of Phases. *Phys.Rev.*, D30:272–285, 1984. doi:10.1103/PhysRevD.30.272. 2

[208] U.A. Yajnik, Hatem Widyan, Debajyoti Choudhari, Shobhit Mahajan, and Amitabha Mukherjee. Topological defects in the left-right symmetric model and their relevance to cosmology. *Phys.Rev.*, D59:103508, 1999. arXiv:hep-ph/9812406, doi:10.1103/PhysRevD.59.103508. 68

[209] U.A. Yajnik, Hatem Widyan, Shobhit Mahajan, Amitabha Mukherjee, and Debajyoti Choudhury. Topological defects and conditions for baryogenesis in the left-right symmetric model. 1998. arXiv:hep-ph/9805276. 68

Acknowledgments

First of all, I wish to thank my supervisor Thomas Konstandin who suggested this really interesting and challenging work on gravitational waves for my Diploma thesis. I am very grateful for his excellent and motivating support throughout the entire period I worked on this thesis. It is incredible how much I learned in this one year.

In addition, I would like to thank Günter Sigl for acting as second examiner of this thesis, who thereby was always willing to discuss and to support my work.

Moreover, I particularly thank Wilfried Buchmüller for giving me the opportunity to carry out my Diploma thesis in the DESY Theory Group. Many thanks also to all other members of the group for providing a really enjoyable working atmosphere at DESY.

Finally and foremost, I am deeply grateful to family. To my younger brothers, Lennart and Yannik, for their understanding, their encouragement and the joy they bring in my life. To my parents, Barbara and Holger, and to my boyfriend Timo for their incredible support and their infinite love. They made this thesis possible in the first place. Therefore it is dedicated to them.

Selbstständigkeitserklärung

Hiermit versichere ich, dass ich diese Arbeit selbstständig verfasst und keine anderen als die angegeben Quellen und Hilfsmittel benutzt habe. Alle Stellen der Arbeit, die wörtlich oder sinngemäß aus anderen Quellen übernommen wurden, sind als solche kenntlich gemacht. Die Arbeit ist in gleicher oder ähnlicher Form noch keiner Prüfungsbehörde vorgelegt worden.

Mit einer zukünftigen Ausleihe der Arbeit in die Bibliothek bin ich einverstanden.

Hamburg, den 20. Dezember 2012

Laura Sagunski